# ABSTRACT


Title of Dissertation: Quantum Circuit Studies with Two-Level Defects of Aluminum Oxide in a Polycrystalline Phase, Amorphous Phase, and at a Metal Surface

Chih-Chiao Hung
Doctor of Philosophy, 2022

Dissertation Directed by: Professor Kevin Osborn
Department of Physics



This thesis reports on recent achievements toward understanding the nanoscale two-level systems (TLS) within aluminum oxide layers. I will discuss novel experimental and theoretical methods using superconducting resonator data to characterize the TLSs, which are deleterious to qubit coherence. This includes (1) a traditional power dependent loss, which provides the information of collective TLS effects, (2) spectroscopy of individual TLSs by DC-tuning, and (3) two-tone spectroscopy of ensemble TLSs by a second saturation tone. We find that the behaviors of TLSs in different structural phases have distinguishing features. Utilizing the DC-tuning feature of our sensor, we further extract dipole moments from individual TLSs and provide the moment histograms of the two aluminum oxide film types. We observe polycrystalline oxide has an average dipole moment = 2.6 Debye and a single-peak histogram consistent with a single TLS origin. On the other hand, TLSs in amorphous oxide have a wide spread of dipole moment values probably due to oxygen deficiency. Saturation slopes of TLSs in bulk films (polycrystalline and

amorphous phases) show a square root dependence of power indicating an ignorable TLS-TLS interaction. Moreover, TLSs in the polycrystalline phase are more stable in the time domain than TLSs in the amorphous phase. Unlike the previous two bulk TLSs, TLSs at the metal-air interface require an explanation from the model assuming TLS frequencies are under stochastic fluctuations originating from TLS-TLS interaction since we find a weak power dependence. We also demonstrate the first published transmon qubits which are solely made from optical lithography. They have a comparable relaxation time and junction resistance to those made from e-beam lithography.

# Quantum Circuit Studies with Two-Level Defects of Aluminum Oxide in a Polycrystalline Phase, Amorphous Phase, and at a Metal Surface

by

Chih-Chiao Hung

Dissertation submitted to the Faculty of the Graduate School of the
University of Maryland, College Park in partial fulfillment
of the requirements for the degree of
Doctor of Philosophy
2022

Advisory Committee:
Professor Kevin Osborn, Co-Chair/Advisor
Professor Christopher Lobb, Chair
Professor Steven Anlage
Professor Alicia Kollar
Professor John Cumings, Dean's Representative

# Acknowledgments

First and foremost I am extremely grateful to my advisor, Dr. Kevin Osborn for his invaluable advice, continuous support, and patience during my Ph.D. study. I still remember the first time we met when he introduced me to the importance of defect studies and brought me into the field of superconducting circuits. I appreciate him giving me the freedom to explore any interesting research. His immense knowledge and plentiful experience have encouraged me all the time in my academic research and daily life.

I thank the committee members, Prof. Christopher J. Lobb, Prof. Steven Anlage, Prof. Alicia Kollar, and Prof. John Cumings for overseeing this dissertation work and the defense.

I would like to thank Prof. Fred Wellstood whose invaluable insight helped improve my understanding several times throughout my Ph.D.

I would also like to thank Dr. Benjamin S. Palmer and Michael Dryer for their technical support in my study. I learned a lot of experimental skills from Ben during our discussions on low-temperature measurements and dilution refrigerator setup. I learned from Michael about the fundamentals and maintenance of dilution refrigerators.

I would like to thank Dr. Bahman Sarabi and Dr. Peng Xu for their advice and support during my first few years at UMD. I learned a lot from their expertise in circuit design and fabrication.

I also owe my gratitude to the people that I enjoyed working with as a group: Dr. Neda

Forouzani, Dr. Liuqi Yu, Dr. Timothy P. Kohler, Dr. Waltraut Wustmann, Dr. Ekta Bhatia, Dr. Yaniv Rosen, and Dr. Stephen Gil. I was very lucky to have such knowledgeable and friendly colleagues. Our countless discussions and meetings were extremely helpful in choosing the best path toward my objectives. Neda and Liuqi were incredibly kind and supportive all the time.

I would like to thank all the members of the LPS cleanroom members - Toby Oliver, Jim Fogleboch, Paul Hannah, Dan Hinkel, Doug Ketchum, Warren Berk, Debtanu Basu, and Jason Moody. It is their kind help and support that have made my study and life in the fabrication a wonderful time. I thank Greg Latini for his help with issues on electronics or computers.

I should also thank many great people at LPS for creating a great work environment: Dr. Jen-Hao Yeh, Dr. Joyce Coppock, Dr. Wan-Ting Liao,

I would like to first thank our theory collaborators, Prof. Alexander L Burin for discussing the data. I thank Dr. Stefan Fritz and Prof. Dagmar Gerthsen provide the aluminum oxide sample.

I would like to thank my friends and roommates around the world. Finally, I would like to express my gratitude to my parents. Without their tremendous understanding and encouragement over the past few years, it would be impossible for me to complete my study.

# Table of Contents

Bibliography 158

# List of Tables

# List of Figures

# List of Abbreviations

| | |
|---|---|
| CMOS | complementary metal-oxide semiconductor |
| CPW | coplanar waveguide |
| cQED | cavity quantum electrodynamics |
| DR | dilution refrigerator |
| DUT | device under test |
| EBQuDS | Electrical-Bridge Quantum-Defect Sensor |
| EM | electromagnetic |
| FS | fast-switching |
| HEMT | high-electron-mobility transistor |
| IDC | interdigital-capacitor |
| JC | Jaynes-Cumming |
| JJ | Josephson junction |
| LE | lumped-element |
| MC | multi-contribution |
| MLE | maximum likelihood estimation |
| PC | processing chamber |
| PCB | printed circuit board |
| PR | photoresist |
| QAOA | quantum approximate optimization algorithm |
| QC | quantum computer |
| QND | quantum non-demolition |
| SC | superconducting |
| SEM | scanning electron microscope |
| STM | standard tunneling model |

TEM transmission electron microscope
TLS two-level system

VNA vector network analyzer

# Chapter 1: Introduction

## 1.1 Overview of quantum computing

Richard Feynman once proposed the idea of using quantum computers (QCs) to simulate quantum systems which can outspeed classical computers [11]. It was unclear how to actually achieve a quantum speed-up until a few quantum algorithms were discovered [12–16]. Peter Shor proposed an algorithm for integer factoring which is computationally difficult for large integers in a classical computer and is the basis of the standard encryption via the internet [12]. Thus, the security of widely used cryptosystems could be potentially broken by QCs [14]. Grover's algorithm solved the problem of searching through unstructured data and showed a potential improvement of operation numbers from $\mathcal{O}(N)$ to $\mathcal{O}(\sqrt{N})$ [16]. In the near future, we might not see the above two algorithms running since they require millions of qubits with very high fidelities [17]. However, some algorithms have potential if we could reach hundreds of qubits. For example, quantum approximate optimization algorithm (QAOA) was proposed to improve the computation time of problems such as Max-Cut and the max-independent set [18]. Moreover, quantum simulation of chemistry problems with quantum processors could potentially have practical consequences in the near-term [19,20]. As a result, cryptography, chemistry simulation, optimization, and machine learning have been significantly impacted by this technology.

The fundamental of computing is a bit, which is the smallest unit of classical information

and can be in one of two discrete values (0 or 1). A classical bit is relatively robust to all sorts of noise, such as physical motions, temperature fluctuations, magnetic fields, etc, within a reasonable margin. Even if an error occurs, well-developed error correction codes can rectify it [21]. A quantum counterpart of a bit is called "qubit". A qubit has states in the basis of $|0\rangle$ and $|1\rangle$, and can represent an infinite set of values. Unlike classical bits, qubits are highly vulnerable to environmental noises [22, 23]. Based on quantum mechanics, any unwanted interactions with the environment will cause a quantum state to collapse into a spurious state. Moreover, imprecision in qubit control would propagate forward during operations, and there is nothing to prevent the accumulating errors from building up. The problems lie in the conflicting demands which requires tremendous efforts to achieve together: a highly isolated quantum system on one side, and fast manipulations and rapid readouts on the other side.

Many schemes of quantum error correction are proposed to correct errors [24–27]. When multiple connected qubits have their gate error per operation below a certain threshold value, then we could bundle many imperfect qubits together into one near-perfect "logical" qubit. In the simplest example, a bit-flip code copies the information multiple times and corrects the error if disagreement happens, while the phase-flip error correction is more complex [24]. A more complicated error-correcting process (i.e. surface code) attempts to use a number of two-dimensional physical qubits array as one fault-tolerant logical qubit [27].

In principle, any quantum system with distinguishable energy states can be operated as a qubit. Many physical implementations have been proposed and developed: polarization optics [28, 29], nuclear spin [30], spins trapped by crystal defects or within quantum dots [31, 32], ionized atoms [33], superconducting qubit [34–36], etc. There are strengths and weaknesses in each approach, and none has convincing advantages to set itself apart as the only candidate.

Superconducting (SC) qubits meet most of the requirements of building QCs in the future: long-lived qubits, purity of two-qubits entanglement control, qubit state readout, scalability, etc. SC qubits utilize the Josephson effect to realize artificial atoms [37] and the well-controlled Josephson junction (JJ) barrier thickness guarantees the accuracy of designed qubit frequencies. A "quantum Moore's law" shows an increase in their lifetime by five orders of magnitude [22, 36]. The improvement of qubit quality comes from many aspects. First of all, researchers learn to avoid the loss mechanisms from (1) two-level systems (TLSs), which are located in disordered interfaces or dielectric materials [38–40], or (2) quasiparticles generated by high-energy particles [41, 42]. Moreover, new superconductor materials, such as Ta [43], Nb [44], or TiN [45, 46], are found to have low loss and replace the traditional metal Al to improve the qubit lifetime. Third, quantum-limited amplifiers utilizing the nonlinearity from JJs [47, 48] or the kinetic inductance of superconductors [49] provide a large signal gain with a small added noise and enhance the readout fidelity. Fourth, noise insensitive designs are proposed to protect qubits from decoherence i.e., transmon [35], fluxonium [50] or 0-$\pi$ [51] qubits, which have delocalized wavefunctions either in charge or/and in phase. Lastly, SC qubits are relatively easy to scale compared to other systems. Due to the compatibility with the well-developed complementary metal-oxide semiconductor (CMOS) techniques, one can design quantum systems on two or three chips with high-density qubits and attach them together [52, 53].

However, when the qubit processors are made more compact, complicated crosstalk between qubits would be an issue that is hard to be classified and be prevented. Moreover, the problems of heating from readout pulses, complex coax cables for qubit frequency control, or insufficient spacing for cryogenic microwave components in cryostat cast a few daunting challenges. In current standard decoherence time ($T_1$ $\sim$100 $\mu$s), the requirement of an arbitrary

quantum algorithm would be millions of qubits and would pose challenges for cryogenic engineering [17]. Additionally, even though the physical size of a qubit is small, it is still larger than that of its classical counterpart. These problems present challenges to the manufacture of high-quality qubits with scalability to fulfill the advantage of quantum computing. In this thesis, we aim to understand TLSs, the dominating loss source, in aluminum oxide, especially their microwave properties and microscopic information. The technique we used would be powerful for future TLS characterization on other materials as well.

### 1.1.1 The Bloch sphere

As mentioned above, the qubit can be described by two levels, the ground state $|0\rangle$ and the excited state $|1\rangle$. A general expression for a qubit state in the basis of $|0\rangle$ and $|1\rangle$ is

$$|\Psi\rangle = \alpha\,|0\rangle + \beta\,|1\rangle\,, \tag{1.1}$$

where $\alpha$ and $\beta$ are two complex numbers. The probabilities of $|0\rangle$ and $|1\rangle$ are $|\alpha|^2$ and $|\beta|^2$, respectively, which can be confirmed in measurements. As expected, the probabilities follow the normalization rule of

$$|\alpha|^2 \;+\; |\beta|^2 \;=\; 1. \tag{1.2}$$

It is useful to imagine the state as a vector on a sphere, also called the Bloch sphere, as shown in Fig. 1.1. We define that two orthogonal basis states, $|0\rangle$ and $|1\rangle$, are on north and south poles on the z-axis, respectively, and $\frac{|0\rangle+|1\rangle}{\sqrt{2}}$ points to the positive x-axis on the Bloch sphere. Each vector on the sphere can also be represented by two real value bases: $\theta$ and $\phi$. $\theta$ is the angle between

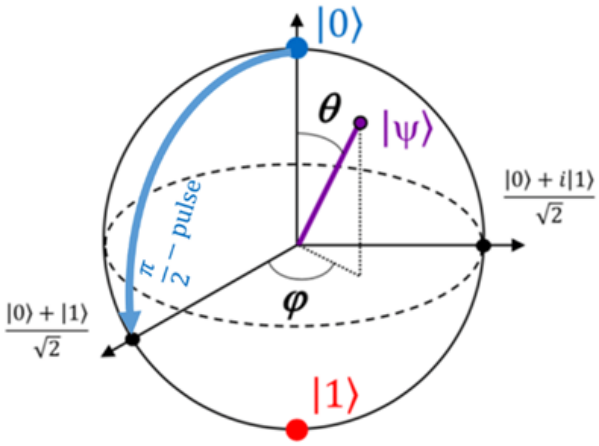


Figure 1.1: The Bloch sphere provides a visualization of a single qubit state. Any point on this sphere can be represented by a linear combination of the $|0\rangle$ and $|1\rangle$ states with complex coefficients as mentioned in Eq. 1.3. A $\frac{\pi}{2}$-pulse 'rotates' a qubit from the $|0\rangle$-state to $\frac{|0\rangle+|1\rangle}{\sqrt{2}}$ along the y-axis. Figure is from Ref. [1]

the vector and the z-axis. $\phi$ is the angle between the vector and the positive x-axis measuring counter-clockwise. The state can be rephrased as

$$|\Psi\rangle = \cos\frac{\theta}{2}|0\rangle + e^{i\phi}\sin\frac{\theta}{2}|1\rangle\,. \tag{1.3}$$

### 1.1.2 Density matrix

A state is called "pure" if it can be represented by a vector $|\Psi\rangle$. For a pure state, the density matrix

$$\rho = |\Psi\rangle\langle\Psi| = \begin{pmatrix} \rho_{00} & \rho_{01} \\ \rho_{10} & \rho_{11} \end{pmatrix} = \begin{pmatrix} |\alpha|^2 & \alpha\beta^* \\ \alpha^*\beta & |\beta|^2 \end{pmatrix}. \tag{1.4}$$

However, it is insufficient if we want to describe qubits in "mixed" states by a vector. Mixed states cannot be represented as linear superpositions of normalized state vectors. Traces of the square $\rho^2$ is smaller than 1, $\mathbf{Tr}(\rho^2) < 1$, for a mixed state. Here $\mathbf{Tr}(A)$ is the sum of all elements on the

diagonal. Mostly, the off-diagonal term, $|\rho_{01}|$, is smaller than $|\alpha\beta^*|$ due to the decoherence or the measurement. For example, due to the nature of a quantum mechanical system, the qubit state would collapse or project on the measurement axis after the measurement. The post-measurement state becomes a mixed state and

$$\rho' = \begin{pmatrix} |\alpha|^2 & 0 \\ 0 & |\beta|^2 \end{pmatrix} \tag{1.5}$$

after measuring in z-axis.

### 1.1.3 Qubit gate and Pauli matrices

For accurate qubit controls, fast operations of a set of quantum gates are essential to maximizing the operation number within the qubit lifetime. Theoretically, all single qubit gates can be comprised of Pauli matrices

$$\sigma_x = \begin{pmatrix} 0 & 1 \\ 1 & 0 \end{pmatrix}, \quad \sigma_y = \begin{pmatrix} 0 & -i \\ i & 0 \end{pmatrix}, \quad \sigma_z = \begin{pmatrix} 1 & 0 \\ 0 & -1 \end{pmatrix} \tag{1.6}$$

and

$$\sigma_+ = \begin{pmatrix} 0 & 2 \\ 0 & 0 \end{pmatrix}, \quad \sigma_- = \begin{pmatrix} 0 & 0 \\ 2 & 0 \end{pmatrix} \tag{1.7}$$

in the basis of $|0\rangle$ and $|1\rangle$. Operators describing the angle $\theta$ of rotation about three axes are $R_x$, $R_y$, and $R_z$, where

$$R_i(\theta) = e^{-i\frac{\theta}{2}\sigma_i} = \cos\left(\frac{\theta}{2}\right)\hat{I} - i\sin\left(\frac{\theta}{2}\right)\sigma_i \tag{1.8}$$

for i = $x,\ y,\ z$. A $\pi$ pulse $R_y\ (\pi)$ or $\frac{\pi}{2}$ pulse $R_y\ (\frac{\pi}{2})$ (see Fig. 1.1), for example rotates the qubit state along the y-axis, is one of the most common gates. A $\frac{\pi}{2}$ pulse rotates the state from $|0\rangle$ to the positive x-axis and is shown in Fig. 1.1.

### 1.1.4 Qubit decoherence

Classically, a bit of 1 that gradually switches to 0 due to noise can be protected by thresholding [21]. However, unlike classical bits, thresholding does not help qubits since qubits no longer carry quantum information after measurements. Additionally, qubits lose their information exponentially via environmental interactions and collapse into a random axis. One kind of noise is "bit-flip" errors that switch the ground state to the excited state and vice versa. Another noise acts on $\phi$ and causes "phase" error corresponding to the unstable energy of a qubit, which has no analogy to the classical one. It is unique because it involves no energy loss.

To incorporate the dissipative environment, one would need to know the Hamiltonian and density operator of the complete system consisting of both the qubit and the environment. This approach is not feasible due to the size of the computation basis. However, this problem can be mitigated by explicitly adding a dissipation term for incoherent interactions with the environment to the qubit Hamiltonian $\mathcal{H}$. The resulting equation is the so-called Lindblad master equation [54]

$$\frac{d\rho}{dt} = -\frac{i}{\hbar}\ [\mathcal{H}, \rho] + \sum_k \Gamma_k D_{\hat{L}_k}(\rho)\,, \tag{1.9}$$

where the jump operators $\hat{L}_k$ describes the exchange of single quanta with the environment at an interaction rate $\Gamma_k$ for the decoherence channel "k", and the Lindblad operator $D_M(\rho) = M\rho M^\dagger - \frac{1}{2}(M^\dagger M\rho + \rho M^\dagger M)$.

For instance, the energy relaxation from a bip-flip error is encoded in the operator $L_1 = |0\rangle\langle 1| = \sigma_-/2$ at a decay rate $\Gamma_1 = 1/T_1$. And the dephasing process from a phase error has operator $L_2 = \sigma_z/\sqrt{2}$ at a dephasing rate $\Gamma_\phi$. Inserting these two error types into Eq. 1.9 yields

$$\frac{d}{dt}\begin{pmatrix} \rho_{00} & \rho_{01} \\ \rho_{10} & \rho_{11} \end{pmatrix} = -\frac{i}{\hbar}\,[\mathcal{H},\rho] + \begin{pmatrix} -\Gamma_1\,\rho_{00} & -\left(\frac{\Gamma_1}{2}+\Gamma_\phi\right)\rho_{01} \\ -\left(\frac{\Gamma_1}{2}+\Gamma_\phi\right)\rho_{10} & \Gamma_1\,\rho_{11} \end{pmatrix}. \tag{1.10}$$

Following standard convention, I define the off-diagonal decay rate (or decoherence rate) $\Gamma_2 = \frac{\Gamma_1}{2} + \Gamma_\phi = 1/T_2$.

In a relaxation measurement, we apply a $\pi$ pulse and readout the qubit of the z-axis after a certain waiting time. An exponential decay is expected and $\rho_{11}(t) = e^{-t/T_1}$ for a state initialized in $|1\rangle$. After measuring on the z-axis several times, we access $\rho_{11}(t)$ by counting the number of the states in $|0\rangle$ and $|1\rangle$. In order to measure the decoherence or the $\phi$ decay, we change the measurement axis by applying two $\frac{\pi}{2}$ pulses with waiting time in between. We determine the performance of a single qubit by these two measurements in Chapter 4.

## 1.2 Wave and Quantum electrodynamics

Cavity quantum electrodynamics (cQED) is a physics subfield that describes a quantum system (with quantized energy levels such as atoms or electrons) interacting with discrete harmonic modes (photons, electromagnetic fields, etc). The quantum electrodynamics of microwave fields and quantum bits implemented in superconducting circuits is called circuit QED (also abbreviated as cQED). cQED plays an important role in superconducting qubit readout [55, 56] and quantum simulations [57]. Following standard methods, I start with the quantized electro-

magnetic field by collective harmonic modes. Second, I will describe the quantization of the field of superconducting LC circuits as a harmonic oscillator or a resonator. Finally, I will use the Jaynes-Cummings (JC) model to describe the whole system including a qubit (atom) and a resonator.

### 1.2.1 Quantization of the electromagnetic field

The first one to describe radiation and matter was Dirac who came up with the idea of the quantization of the electromagnetic field as an ensemble of harmonic oscillators and introduced the concept of creation and annihilation operators of particles [58]. He was able to describe the spontaneous emission probability of an atom. One of the standard strategies to describe a light-matter system involves quantization of the electromagnetic (EM) field. It is convenient to consider an EM field without a source as a collection of infinite harmonic oscillator modes. From Maxwell equations, I can write the electrical field ($\boldsymbol{E}$) and magnetic field ($\boldsymbol{B}$) which must satisfy the vector potential ($\boldsymbol{A}$) and scalar potential ($\Phi$) as

$$\begin{aligned} \boldsymbol{E} &= -\frac{1}{c}\frac{\partial \boldsymbol{A}}{\partial t} - \nabla\Phi \\ \boldsymbol{B} &= \nabla \times \boldsymbol{A} \\ \nabla \cdot \boldsymbol{E} &= 0 \\ \nabla \times \boldsymbol{B} - \frac{1}{c}\frac{\partial \boldsymbol{E}}{\partial t} &= 0 \end{aligned} \tag{1.11}$$

For the total field in a volume $V$ supposing periodic boundary conditions, we can perform a Fourier expansion on $A$ over a collection of these modes $\mathbf{k}$:

$$\boldsymbol{A}(\mathbf{r}, \boldsymbol{t}) = \frac{1}{\sqrt{V}} \sum_{\mathbf{k}} \boldsymbol{A}_{\boldsymbol{k}}(t)\, e^{i\mathbf{k}\cdot\mathbf{r}}, \tag{1.12}$$

where

$$\int d^3\mathbf{r}\; e^{i\mathbf{k}\cdot\mathbf{r}} e^{-i\mathbf{k}'\cdot\mathbf{r}} = V\delta_{\boldsymbol{k}\boldsymbol{k}'}. \tag{1.13}$$

Two potentials are put in the radiation gauge such that any set of the potential has the properties $\Phi = 0$ and $\nabla \cdot \boldsymbol{A} = 0$ resulting in $\boldsymbol{k} \cdot \boldsymbol{A}_{\boldsymbol{k}} = 0$. From Eq. 1.11, the vector potential satisfies a wave equation $\nabla^2 \boldsymbol{A} - \frac{1}{c^2}\frac{\partial^2 \boldsymbol{A}}{\partial t^2} = 0$ and we can further choose $\boldsymbol{A}_{\boldsymbol{k}}(t) = \boldsymbol{A}_{\boldsymbol{k}}\, e^{-i\omega_{\boldsymbol{k}} t}$ and $\omega_{\boldsymbol{k}} = |\boldsymbol{k}|c$. In the case of a standing wave in a box, the standing wave is a combination of positive and negative wavevector $\boldsymbol{k}$ and we obtain a new equation from Eq. 1.12:

$$\boldsymbol{A}(\boldsymbol{r}, t) = \frac{1}{2\sqrt{V}} \sum_{\boldsymbol{k}} \boldsymbol{A}_{\boldsymbol{k}} e^{i\boldsymbol{k}\cdot\boldsymbol{r} - i\omega_{\boldsymbol{k}} t} + \boldsymbol{A}_{-\boldsymbol{k}} e^{-i\boldsymbol{k}\cdot\boldsymbol{r} + i\omega_{\boldsymbol{k}} t}. \tag{1.14}$$

Since $\boldsymbol{A}^* = \boldsymbol{A}$, we get $\boldsymbol{A}_{-\boldsymbol{k}} = A^*_{\boldsymbol{k}}$. The energy $\mathcal{H}_{EM}$ in the space contains energy from the electric field and magnetic field, and

$$\mathcal{H}_{EM} = \frac{1}{8\pi} \int d^3x (\boldsymbol{E}^2 + \boldsymbol{B}^2) = \frac{1}{8\pi} \int d^3x \left[ \frac{1}{c^2} \left( \frac{\partial \boldsymbol{A}}{\partial t} \right)^2 + (\nabla \times \boldsymbol{A})^2 \right]. \tag{1.15}$$

Substituting $\boldsymbol{A}$ from Eq. 1.14 yields

$$\mathcal{H}_{EM} = \frac{1}{8\pi} \sum_{\boldsymbol{k}} \frac{\omega_{\boldsymbol{k}}^2}{c^2} |\boldsymbol{A}_{\boldsymbol{k}}|^2 + \boldsymbol{k}^2 |\boldsymbol{A}_{\boldsymbol{k}}|^2, \tag{1.16}$$

which looks similar to the Hamiltonian of a classical harmonic oscillator. Inspired by Dirac and harmonic motions, we can introduce annihilation operators, $a_{\boldsymbol{k}}$ and $a_{-\boldsymbol{k}}$, for the $\boldsymbol{k}$ and -$\boldsymbol{k}$ mode. Since $\boldsymbol{k} \cdot \boldsymbol{A_k} = 0$, there are two transverse unit vectors corresponding to photon polarization $\hat{\boldsymbol{e}}_\alpha$, where $\alpha$ = 1, 2. Therefore, we obtain

$$\boldsymbol{A_k} = \sqrt{\frac{4\pi c^2 \hbar}{\omega_{\boldsymbol{k}}}} \sum_\alpha \frac{a_{\boldsymbol{k\alpha}} + a^\dagger_{-\boldsymbol{k\alpha}}}{\sqrt{2}} \hat{\boldsymbol{e}}_\alpha, \tag{1.17}$$

and

$$\mathcal{H}_{EM} = \frac{\hbar}{4} \sum_{\boldsymbol{k}\alpha} \left( a_{\boldsymbol{k}\alpha} a^\dagger_{\boldsymbol{k}\alpha} + a^\dagger_{\boldsymbol{k}\alpha} a_{\boldsymbol{k}\alpha} + a_{-\boldsymbol{k}\alpha} a^\dagger_{-\boldsymbol{k}\alpha} + a^\dagger_{-\boldsymbol{k}\alpha} a_{-\boldsymbol{k}\alpha} \right) = \hbar \sum_{\boldsymbol{k}\alpha} \left( a^\dagger_{\boldsymbol{k}\alpha} a_{\boldsymbol{k}\alpha} + \frac{1}{2} \right). \tag{1.18}$$

We can recast $\boldsymbol{A}(\boldsymbol{r}, t)$ as

$$\boldsymbol{A}(\boldsymbol{r}, t) = \frac{1}{2\sqrt{V}} \sum_{\boldsymbol{k}\alpha} \hat{\boldsymbol{e}}_\alpha \left[ \sqrt{\frac{4\pi c^2 \hbar}{\omega_{\boldsymbol{k}}}} \left( \frac{a_{\boldsymbol{k}\alpha} + a^\dagger_{-\boldsymbol{k}\alpha}}{\sqrt{2}} \, e^{i\boldsymbol{k}\cdot\boldsymbol{r} - i\omega_{\boldsymbol{k}} t} + \frac{a_{-\boldsymbol{k}\alpha} + a^\dagger_{\boldsymbol{k}\alpha}}{\sqrt{2}} \, e^{-i\boldsymbol{k}\cdot\boldsymbol{r} + i\omega_{\boldsymbol{k}} t} \right) \right]. \tag{1.19}$$

Finally, $\boldsymbol{E}$ and $\boldsymbol{B}$ are quantized as

$$\boldsymbol{E}(\boldsymbol{r}, t) = i \sqrt{\frac{2\pi\hbar}{V}} \sum_{\boldsymbol{k}\alpha} \sqrt{\omega_{\boldsymbol{k}}} \, \hat{\boldsymbol{e}}_\alpha \, \left( a_{\boldsymbol{k}\alpha} \, e^{i\boldsymbol{k}\cdot\boldsymbol{r} - i\omega_{\boldsymbol{k}} t} - a^\dagger_{\boldsymbol{k}\alpha} \, e^{-i\boldsymbol{k}\cdot\boldsymbol{r} + i\omega_{\boldsymbol{k}} t} \right) \tag{1.20}$$

$$\boldsymbol{B}(\boldsymbol{r}, t) = i \sqrt{\frac{2\pi\hbar c^2}{V}} \sum_{\boldsymbol{k}\alpha} \frac{\boldsymbol{k} \times \hat{\boldsymbol{e}}_\alpha}{\sqrt{\omega_{\boldsymbol{k}}}} \, \left( a_{\boldsymbol{k}\alpha} \, e^{i\boldsymbol{k}\cdot\boldsymbol{r} - i\omega_{\boldsymbol{k}} t} - a^\dagger_{\boldsymbol{k}\alpha} \, e^{-i\boldsymbol{k}\cdot\boldsymbol{r} + i\omega_{\boldsymbol{k}} t} \right). \tag{1.21}$$

### 1.2.2 Quantization of LC circuit

An LC circuit is also a harmonic oscillator (resonator), and, therefore, can be quantized using the same methods as mentioned in Chap. 1.2.1. Quantizing resonators are important to understand the fundamental of our quantum system. To begin with, I will start from the classical LC circuit. From current $I$ and voltage $V$ relationship in inductor $L$ and capacitor $C$, we have

$$\begin{aligned} I(t) &= C\frac{dV(t)}{dt} \\ V(T) &= L\frac{dI(t)}{dt} \\ \frac{d^2}{dt^2}I(t) + \frac{1}{LC}I(t) &= 0 \end{aligned} \tag{1.22}$$

with the angular resonant frequency $\omega = \frac{1}{\sqrt{LC}}$. The energies store in $C$ and $L$ are $U_C = \frac{1}{2}CV^2$ and $U_L = \frac{1}{2}LI^2$, respectively, and the Lagrangian

$$\mathcal{L} = \frac{1}{2}CV^2 - \frac{1}{2}LI^2. \tag{1.23}$$

Choosing a more convenient pair of variables (branch flux $\phi$ and branch charge $Q$) [59] by the definition that

$$Q(t) = \int_{-\infty}^{t} I(\tau)d\tau \tag{1.24}$$

and

$$\phi(t) = \int_{-\infty}^{t} V(\tau)d\tau = \int_{-\infty}^{t} \frac{Q(\tau)}{C}d\tau, \tag{1.25}$$

I get

$$\mathcal{L} = \frac{Q^2}{2C} - \frac{\phi^2}{2L} \tag{1.26}$$

or

$$\mathcal{L} = \frac{C\dot{\phi}^2}{2} - \frac{\phi^2}{2L}. \tag{1.27}$$

Since $\frac{\delta \mathcal{L}}{\delta \dot{\phi}} = \mathcal{L}\dot{Q} = \phi$, $\phi$ and $Q$ are a pair of conjugate variables . Therefore, the Hamiltonian $\mathcal{H}_{LC}$ in terms of $\phi$ and $Q$ is

$$\mathcal{H}_{LC} = \frac{\phi^2}{2L} + \frac{Q^2}{2C}. \tag{1.28}$$

The transformation from classical to quantum mechanics is similar to the Hamiltonian of a mechanical oscillator $\mathcal{H}_{mec} = \frac{\hat{p}^2}{2m} + \frac{m\omega^2}{2}\hat{x}^2$ through $\hat{p} \to \hat{Q}$, $\hat{x} \to \hat{\phi}$, $m \to C$ and $m\omega^2 \to \frac{1}{L}$. The annihilation operator $a$ for LC circuit can be written as $a = \frac{1}{\sqrt{\hbar\omega}}\left(\frac{\hat{\phi}}{\sqrt{2L}} - i\frac{\hat{Q}}{\sqrt{2C}}\right)$ such that

$$\hat{\phi} = \sqrt{\frac{\hbar Z}{2}}(a^\dagger + a) \tag{1.29}$$

and

$$\hat{Q} = -i\sqrt{\frac{\hbar}{2Z}}(a^\dagger - a), \tag{1.30}$$

where $Z = \sqrt{\frac{L}{C}}$. A useful expression of voltage operator $\hat{V} = \frac{\hat{Q}}{C} = -i\sqrt{\frac{\hbar\omega}{2C}}(a^\dagger - a)$ [60]. The amplitude of $\hat{V}$ is $V_{zpf} = \sqrt{\frac{\hbar\omega}{2C}}$ and is frequently used in later chapters for calculation of the Rabi frequency or the coupling strength of TLS-resonator. For example, the zero-point electrical field of a tri-layer capacitance $C$ in an LC resonator is

$$E_{zpf} = \frac{V_{zpf}}{d} = \frac{\sqrt{\frac{\hbar\omega}{2C}}}{d} = \sqrt{\frac{\hbar\omega}{2\varepsilon V}}, \tag{1.31}$$

where the dielectric has a thickness $d$, a dielectric constant $\varepsilon$ and a volume $V$.

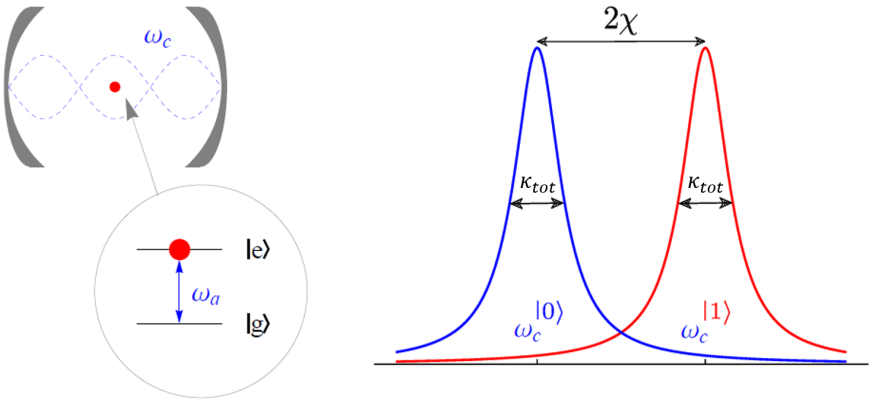


Figure 1.2: Left: Illustration of the Jaynes-Cummings model. An atom with two states sits inside a cavity. Figure is from Wiki (link). Right: The cavity resonant frequency depends on qubit's state and the frequency shift is $2\chi$. To obtain high readout fidelity, it is important to have $2\chi > \kappa_{tot}$, where $\kappa_{tot}$ is the total decay rate of the resonator. Figure is from Ref. [2]

## 1.3 Jaynes-Cumming model

The Jaynes-Cumming (JC) model describes the system of a two-level atom interacting with a quantized mode of a harmonic oscillator (or a bosonic field) shown in Fig. 1.2. The JC model is particularly important in describing qubit-resonator systems due to the readout scheme. The full Hamiltonian is

$$\mathcal{H} = \mathcal{H}_{field} + \mathcal{H}_{atom} + \mathcal{H}_{int}, \tag{1.32}$$

which consists of the field Hamiltonian $\mathcal{H}_{field}$, the atom Hamiltonian $\mathcal{H}_{atom}$, and the interaction of atom-field Hamiltonian $\mathcal{H}_{int}$. Here, $\mathcal{H}_{field} = \hbar\omega_c a^\dagger a$, $\mathcal{H}_{atom} = \frac{\hbar\omega_a}{2}\sigma_z$ and $\mathcal{H}_{int} = \hbar g(a + a^\dagger)(\sigma_+ + \sigma_-)$, where $g$ is the coupling strength, $\omega_c$ is the harmonic mode frequency, and $\omega_a$ is atom frequency.

The special case where the detuning $\Delta = \omega_c - \omega_a$ is much larger than $g$ gives the so-called dispersive regime. In this limit, the qubit and the cavity do not exchange energy, meaning

the eigenstates of the system can be well approximated by the product states of the qubit and the cavity. Starting from the JC model, I apply a unitary transformation $\hat{D} = \exp(\lambda X_-) = \exp\{(\frac{g}{\Delta}(\sigma_- a^\dagger - \sigma_+ a^-))\}$ on $\mathcal{H}$ and expand the dispersive Hamiltonian

$$\mathcal{H}_{disp} = \hat{D}^\dagger \mathcal{H} \hat{D} = \mathcal{H} + \lambda [H, X_-] + \frac{\lambda^2}{2} [[H, X_-], X_-] + \mathcal{O}(\lambda^3), \tag{1.33}$$

where $\lambda = \frac{g}{\Delta}$ is a small value. I further simplify the equation while considering only the first order of $\lambda$ and

$$\mathcal{H}_{disp} = \frac{1}{2}\left(\omega_a + \frac{g^2}{\Delta} a^\dagger a\right)\sigma_z + \hbar\omega_c a^\dagger a \tag{1.34}$$

or

$$\mathcal{H}_{disp} = \frac{1}{2}\hbar\omega_a\sigma_z + \hbar\left(\omega_c + \frac{g^2}{\Delta}\sigma_z\right) a^\dagger a. \tag{1.35}$$

The above Eq. 1.35 indicates the possibility of quantum non-demolition (QND) measurements. A QND measurement would leave the qubit in its measured eigenstate, e.g. if one measures $|1\rangle$ the state will remain in $|1\rangle$ upon repeated measurements. Mathematically, it means that a QND measurement operator $\hat{M}$ is commuting with the full Hamiltonian: $[\mathcal{H}_{disp}, M] = 0$. We can realize QND measurement by probing the cavity frequency which yields $\hat{M} = a^\dagger a$. Experimentally, we will observe that the cavity frequency $\omega_c \pm \chi$ is depending on the state of a qubit, where $\chi = \frac{g^2}{\Delta}$. The illustration of the state-dependent resonator frequencies, $\omega_c^{|0\rangle}$ and $\omega_c^{|1\rangle}$, is shown in Fig. 1.2. A high-fidelity readout is shown when the two times the dispersive shift larger than the total decay rate $\kappa_{tot}$ of a resonator: $2\chi > \kappa_{tot}$ [56].

## 1.4 Overview of thesis

In our group, we try to understand the loss mechanisms of superconducting devices which could direct a path for further improving the single qubit performance. My thesis is divided into three parts: (a) characterization and analysis of TLS individually in bulk dielectrics, (b) fast-switching behavior of Al surface TLS, and (c) measurement of all-optical lithography made transmons. The goal of the thesis is to increase the understanding of nanoscale TLS defects.

In Chapter 2, I describe the standard tunneling model of TLS together with the design of my defect sensors. In Chapter 3, I describe the experimental setup along with the equipment for device fabrications. In Chapter 4, I introduce transmons solely made by optical lithography. In Chapter 5, I introduce the TLS spectrum in two structural phases of alumina. In addition, I describe the factors that prevent dipole extraction. Chapter 6 describes vacuum-gap resonators which provide evidence of interacting TLS. Finally, I summarize the thesis in Chapter 7.

# Chapter 2: Superconducting Devices and Nanoscale Two-Level Defects

## 2.1 Quantum engineering

Exploiting the ultralow resistance of superconductors makes high-quality resonators possible. In 1911 Heike Kamerlingh Onnes discovered the first superconductor. He measured the disappearance of the resistivity of mercury at temperature below 4.25K. In the 1950s, the theory proposed by Bardeen, Cooper, and Schrieffer (BCS) microscopically describes the superconductivity [61]. They find that a weak attractive interaction between electrons and phonons can cause the formation of bound pairs of electrons which they called Cooper pairs.

Resonators made by superconductors will have very small energy loss from Joule heating and, therefore, secure high-quality factors $Q$. For example, bulk niobium resonators used in particle accelerators reach quality factors of $10^{11}$ [62]. In superconducting circuit, clean superconducting materials such as aluminum and niobium can be grown easily by a physical vapor deposition method and are compatible with the standard lithography fabrication processes. Moreover, the Josephson effect, describing Cooper pairs tunneling between two superconductors separated by a thin insulator, provides the nonlinearity for superconducting qubits [63].

In this section, I will introduce the concepts of lossless transmission lines and LC circuits as resonators for material characterization.

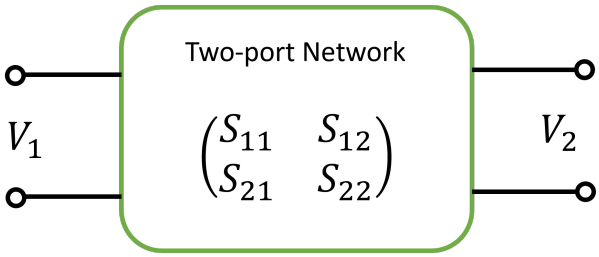


Figure 2.1: Schematic of a two-port network characterised by its scattering matrix.

### 2.1.1 Two-port network and scattering matrix

A two-port network shown in Fig. 2.1 is an electric circuit with two pairs of terminals. Mathematically, a two-port network is fully described by a 2 by 2 scattering matrix of complex numbers

$$\hat{S} = \begin{pmatrix} S_{11} & S_{12} \\ S_{21} & S_{22} \end{pmatrix}. \tag{2.1}$$

Defining the incident voltage waves as $V_k^+$ and the reflected (output) wave as $V_k^-$ from port k,

$$S_{11} = \frac{V_1^-}{V_1^+} \text{ and } S_{22} = \frac{V_2^-}{V_2^+}. \tag{2.2}$$

Similarly,

$$S_{12} = \frac{V_1^-}{V_2^+} \text{ and } S_{21} = \frac{V_2^-}{V_1^+}. \tag{2.3}$$

For instance, a lossless ideal transmission line mentioned later in Chap. 2.1.2 has magnitudes of $S_{12}$ and $S_{21}$ equal to 1 and that of $S_{11}$ and $S_{22}$ equal to 0. The scattering matrix is particularly important for resonator measurements as they directly reflect the properties such as $Q$ and accessible through the measurement from a vector network analyzer (VNA).

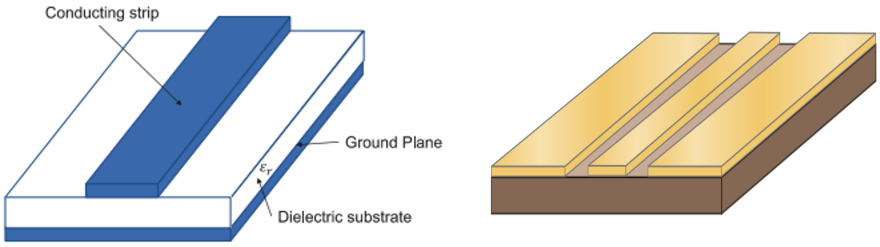


Figure 2.2: Left: Microstrip transmission line. It consists of 3 layers, conducting strip, dielectric and ground plane. Right: Coplanar waveguide transmission line. It is formed from a center trace separated from a pair of ground planes, all on the same plane, atop a substrate.

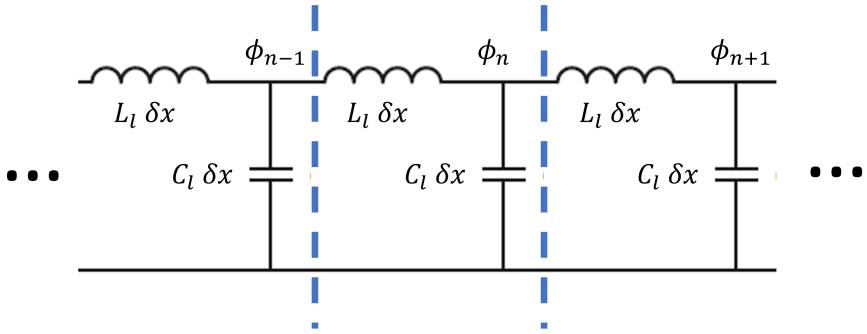


Figure 2.3: Lossless transmission line model: A lumped element representation of infinitesimal sections of inductors and capacitors. A unit is comprised of a small inductor in wave transmission direction and a capacitor to ground.

### 2.1.2 Transmission line

Transmission lines are one-dimensional waveguides and form an important part of quantum circuits since they provide channels for transmitting signals. Microstrips, which have a center trace and ground plane separated by dielectrics, and coplanar waveguides (CPW), which have a center trace and ground planes on the same level, are two of the transmission line types (Fig. 2.2). CPW is more widely used due to the fewer fabrication steps and lower loss per meter than microstrips. Both types can be described by a model of infinitesimal sections along two conductors in the transverse direction of propagation [64]. In a simple case, we only consider the lossless transmission line for CPW since the loss per meter is generally close to 0. The illustration

of a lossless model is shown in Fig. 2.3.

In the case of a uniform capacitance and inductance per length, $C_l$ and $L_l$, respectively, the n-th infinitesimal section with length $\delta x$ contains a small capacitor $\delta C = C_l \delta x$ and inductor $\delta L = L_l \delta x$. The Lagrangian is given by the sum over the energies of all nodes or sections,

$$\mathcal{L}_{TL} = \sum_n \left( \frac{1}{2} \delta C \dot{\phi}_n^2 + \frac{1}{2} \frac{(\phi_n - \phi_{n-1})^2}{\delta L} \right), \tag{2.4}$$

where $\phi_n$ is the flux of the n-th node and is defined in Eq. 1.2.2. Further, if $\delta x \to 0$, we yield

$$\mathcal{L}_{TL} = \int_{-L}^{L} dx \left[ \frac{C_l}{2} \dot{\phi}(x,t)^2 - \frac{1}{2L_l} (\phi'(x,t))^2 \right]. \tag{2.5}$$

The equation of motion for this Lagrangian is

$$C_l \ddot{\phi}(x,t) = \frac{1}{L_l} \frac{\partial^2 \phi(x,t)}{\partial x^2}. \tag{2.6}$$

The phase velocity with which a signal propagates through the CPW structure is given by $\nu_{ph} = \frac{1}{\sqrt{L_l C_l}}$, and electromagnetic waves propagating along a transmission line depend only on $C_l$ and $L_l$ [65]. This model can build open systems, resonators, or semi-infinite systems with one or two shorted ends. The differences are given by the boundary condition of the circuit configuration. Next, I will describe CPW transmission lines with one or two openings as a common type of resonator.

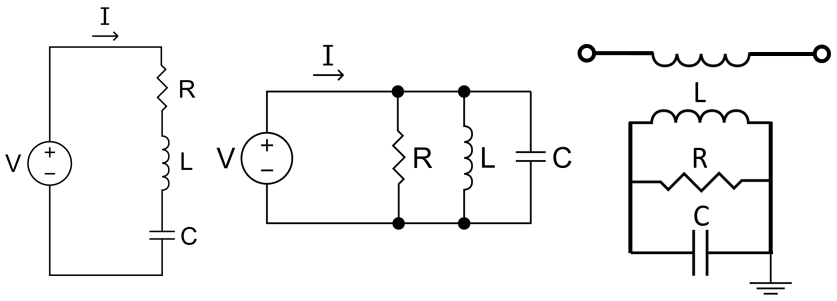


Figure 2.4: Lumped element representations of RLC circuit. Left: a series RLC. Middle: a parallel RLC. Right: a RLC circuit inductively couples to a transmission line. Energy is exchanged through the mutual inductance between the transmission line and the resonator.

### 2.1.3 Overviews of superconducting resonators

In superconducting quantum information, LC oscillators are typically used to control and read out the state of a qubit. Generally, LC oscillators cannot be used as a qubit solely, (exceptions see [66]). Energies with $\hbar\omega$ could excite the ground state to the first excited state but also lead to the excitation of the first excited state to the second state as $\omega_{10} = \omega_{12}$. One can avoid this by using a non-linear element, which is the Josephson junction and will be mentioned in Chapter 4, to change the energy potential from harmonic to anharmonic: $\omega_{10} \neq \omega_{12}$.

Electrical circuits comprising inductive and capacitive elements have a resonance frequency due to the opposite phase shift between their impedance. The most general model here is an RLC circuit, named after its components: resistor ($R$), inductor ($L$), and capacitor ($C$). These can be arranged in series or parallel (see Fig. 2.4). The model we used the most in our group is the one in the right panel where the resonator is inductively coupled to the transmission line. The effective input impedance $Z_{in}$ of our resonators is

$$Z_{in} = \left(\frac{1}{R} + \frac{1}{i\omega L} + i\omega C\right)^{-1}. \tag{2.7}$$

$Z_{in}$ becomes a purely real value, when $\omega$ is the resonance frequency $\omega_0 = \frac{1}{\sqrt{LC}}$.

Resonators or cavities made with superconductors show a high total quality factor $Q = \frac{\omega_0}{\Delta\omega_0}$, where $\Delta\omega_0$ is the bandwidth. The quality factor can be characterized into two groups, external or internal quality. The internal quality factor is defined as

$$Q_i = \omega_0 RC. \tag{2.8}$$

$Q_i$ describes the energy loss into the resistance which represents an environmental bath (TLSs, quasiparticles, etc). The $Q_i$ of the resonators relates to similar superconducting structures, e.g. coplanar shunting capacitors [67], and the qubit relaxation time

$$T_1 \sim \frac{Q_i}{\omega_0}. \tag{2.9}$$

Loss due to the coupling to the transmission line is characterized by the external quality factor $Q_e$. A moderate $Q_e$ is important for qubit measurements. If $Q_e$ is too small, noise or thermal photons would easily accumulate and reduce the coherence time [68]. If $Q_e$ is too large, it takes too long for readout photons to ring up. Lastly, the total decay rate $\kappa_{tot}$ is the sum of the external decay rate $\kappa = \frac{\omega_0}{Q_e}$ and the internal decay rate $\Gamma_r = \frac{\omega_0}{Q_i}$, and

$$\kappa_{tot} = \frac{\omega_0}{Q} = \kappa + \Gamma_r = \frac{\omega_0}{Q_i} + \frac{\omega_0}{Q_e}. \tag{2.10}$$

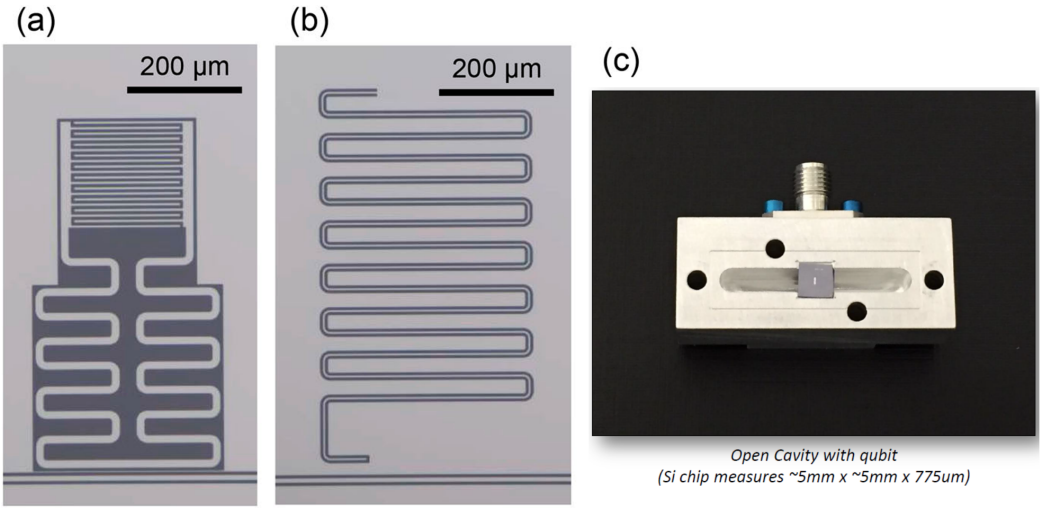


Figure 2.5: Images of different types of resonators. (a) Lumped element resonator. Distinguishable inductance part in a meander shape on the bottom and capacitance part in an inter-digital shape on the top are shown. (b) Coplanar waveguide resonator. The length of the resonator determines the resonant frequency. Panel (a) and (b) from Ref. [3]. (c) 3D cavity containing a transmon on a Si chip measured in Chap 4.

### 2.1.4 Types of resonators

The common resonator types include "2D" and "3D" geometries and are shown in Fig. 2.5. For planar or 2D geometry, lumped-element (LE) resonators and coplanar waveguide (CPW) resonators are two well-known types. In an LE resonator, the inductive region is a thin length of wire in a meander or spiral shape, and the capacitor is two pads of metal separated by a gap. Generally, there is only one fundamental resonance $\omega_0$ which equals $\frac{1}{\sqrt{LC}}$. an LE resonator can couple to the transmission line inductively or capacitively and usually has the same coupling strength to two ports ($\kappa_1 = \kappa_2$). On the other hand, CPW resonators have an infinite number of standing wave modes and the resonance depends on the boundary condition of whether the resonator has one or two openings. No current can flow at the open ends which leads to voltage anti-nodes and current nodes. Oppositely, closed ends require the voltage relative to the ground must be zero. The opening of the transmission line is an anti-node for voltage and a node for

current. A resonator with two openings is called $\frac{\lambda}{2}$ resonator and needs to fulfill the boundary condition: $\lambda_n = \frac{2}{n}\, l$, where $\lambda_n$ is the wavelength, $n$ is an integer and $l$ is the length of CPW. A resonator with one opening is called $\lambda/4$ resonator and the resonant condition is $\lambda_n = \frac{4}{2n+1}\, l$.

Generally, the dielectric loss is larger when the distance between two superconductor planes is closer due to the larger filling factor in the dielectric. It means the trade-off between the resonator's physical size and its internal loss. Long single-photon lifetimes on the order of milliseconds are observed in 3D cavities, whose size is thousands of times larger than the size of a 2D resonator [69]. In recent years, 3D cavities attract considerable interest because of the increased coherence times of qubits within a 3D cavity [70] and the proposals of bosonic qubits [71,72]. A 3D cavity can have rectangular or cylindrical shape and its dimension defines the modes. For a rectangular waveguide terminating both sides, we can compute the modes as [64]

$$f_{kmn} = \frac{c}{2\pi\sqrt{\mu_r \epsilon_r}} \sqrt{\left(\frac{\pi \cdot k}{l_a}\right)^2 + \left(\frac{\pi \cdot m}{l_b}\right)^2 + \left(\frac{\pi \cdot n}{l_c}\right)^2}, \tag{2.11}$$

where $c$ denotes the speed of light in vacuum, $\mu_r$ is the relative magnetic permeability and $\epsilon_r$ is the relative permittivity of the material inside the cavity, $l_a$, $l_b$ and $l_c$ are the dimensions of the cavity, and $k$, $m$ and $n$ are integers.

$\kappa_1$ and $\kappa_2$ can be set differently in CPW and 3D resonators by choosing different input and output capacitors $C_{in}$ and $C_{out}$. It is favorable to make the output capacitor large for maximizing the signal power sent into the output port which connects to the amplification chain for readout. The total external quality factor

$$Q_e = \frac{C}{\omega_0 Z_0 (C_{in}^2 + C_{out}^2)}, \tag{2.12}$$

where $Z_0$ is the impedance of the line and usually equals 50 $\Omega$.

### 2.1.5 Resonator transmission equation

The quality factor of a resonator can be determined by the transmission rate of two ports as a function of frequency, $S_{21}(\omega)$. I define $a$, $a_{i,in}$ and $a_{i,out}$ as the annihilation operators for the cavity, the input wave from port i and the output wave to port i, respectively. According to the input-output theory [73], I can get

$$\begin{aligned} \frac{da}{dt} &= -i\left(\omega-\omega_0\right) - \frac{\kappa_1+\kappa_2+\Gamma_r}{2}a + \sqrt{\kappa_1}a_{1,in} + \sqrt{\kappa_2}a_{2,in}, \\ a_{1,out} &= a_{1,in} - \sqrt{\kappa_1}a, \\ a_{2,out} &= a_{2,in} - \sqrt{\kappa_2}a, \end{aligned} \tag{2.13}$$

where $\kappa_1$ and $\kappa_2$ are the coupling rate to port 1 and port 2, respectively. If assuming a symmetric coupling $\kappa_1 = \kappa_2 = \frac{k}{2}$, I obtain a Lorentzian function

$$S_{21} = \frac{a_{2,out}}{a_{1,in}} = 1 - \frac{\frac{k}{2}}{i(\omega-\omega_0)+\frac{k+\Gamma_r}{2}} = 1 - \frac{\frac{Q}{Qe}}{1+2iQ\left(\frac{\omega-\omega_0}{\omega_0}\right)}, . \tag{2.14}$$

In reality, the resonator response usually is not symmetric in $\omega$ due to impedance mismatches. Mismatches can be from the cables, the printed circuit board (PCB) of the sample box, or CPW on a chip. The correction is derived in Ref. [74], where I replace $Q_e$ in Eq. 2.14 by a complex $\hat{Q}_e = |\hat{Q}_e|e^{i\phi}$ and $\Delta = \omega - \omega_0$:

$$S_{21} = 1 - \frac{\frac{Q}{\hat{Q}_e}}{1+2iQ\Delta/\omega_0} = 1 - \frac{\frac{Q}{|\hat{Q}e|}e^{-i\phi}}{1+2iQ\Delta/\omega_0}. \tag{2.15}$$

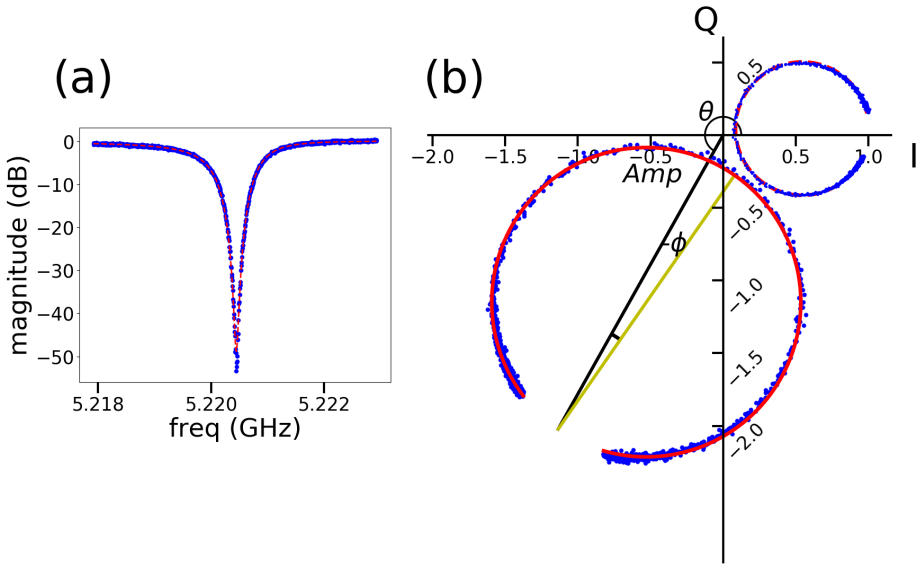


Figure 2.6: An example of transmission data $S_{21}$ and fitting curve. (a) Magnitude of $S_{21}$ vs frequency. (b) Real and imaginary part of $S_{21}$. The red line is the fitting of Eq. 2.16. The black line represents the scaling of amplitude and the rotation from (1,0). The yellow line represents a $\phi$ rotation from a small impedance mismatch. We plot the data with a normalized amplitude and an electric delay correction on the right hand side of this figure.

We denote a new definition for $Q_i^{-1} = Q^{-1} - Re(\hat{Q}_e^{-1})$.

The amplitude and phase of transmission signal after a series of attenuation and amplification are usually not normalized. A more general case is

$$S_{21} = Amp \times e^{i\theta} \times \left(1 - \frac{Q|\hat{Q}_e^{-1}|e^{-i\phi}}{1 + 2iQ\Delta/\omega_0}\right). \tag{2.16}$$

We show an example of fit in Fig. 2.6 in red, where the magnitude of $S_{21}$ and IQ data in panels (a) and (b), respectively. In panel (b), we observe a small impedance mismatch rotation $\phi = 5.66°$ in the yellow line (on the lower left). The $\phi$-corrected and normalized $S_{21}$ is displayed with its opening facing (1,0).

### 2.1.6 Number of photon in resonators

In quantum physics, the electromagnetic field inside the resonator can be quantized. Therefore, it is convenient to express the energy (microwave power) as an average number of photon $n_{ph}$. When the resonator is probed with an applied power $P_{in}$ at frequency $\omega$, the average number of input photon $n_{1,in} = \langle a^{\dagger}_{1,in} a_{1,in} \rangle = P_{in}/\hbar\omega$. From Eq. 2.13 and a real external coupling $\kappa = 2\kappa_1 = 2\kappa_2$, we have

$$\begin{aligned} \sqrt{\kappa/2} a_{1,in} &= \left(i\Delta + (\kappa + \Gamma_r)/2\right) a \\ n_{ph} &= \frac{\frac{\kappa}{2}}{\left(\frac{\kappa+\Gamma_r}{2}\right)^2 + \Delta^2} n_{1,in}. \end{aligned} \tag{2.17}$$

In the case of $\omega = \omega_0$,

$$n_{ph} = 2\frac{Q^2}{Q_e}\frac{P_{in}}{\hbar\omega_0^2}, \tag{2.18}$$

which agrees with Ref. [75].

## 2.2 Two-level systems

In 2005, it was the first time Martinis et al. [34] reported that dielectrics were the dominant loss mechanism in their superconducting qubits. They observed that dielectric loss was saturated by high-power microwave in resonators. Similar phenomena had been previously understood as arising from resonant absorption of the acoustic wave by a bath of two-level systems (TLS) possessing a strain dipole moment [76, 77]. Likewise, TLSs with electric dipole moment would couple to qubits or resonators and absorb their energy. This chapter will start with the history and background of amorphous glass studied in the 1970s and then the refinements of models

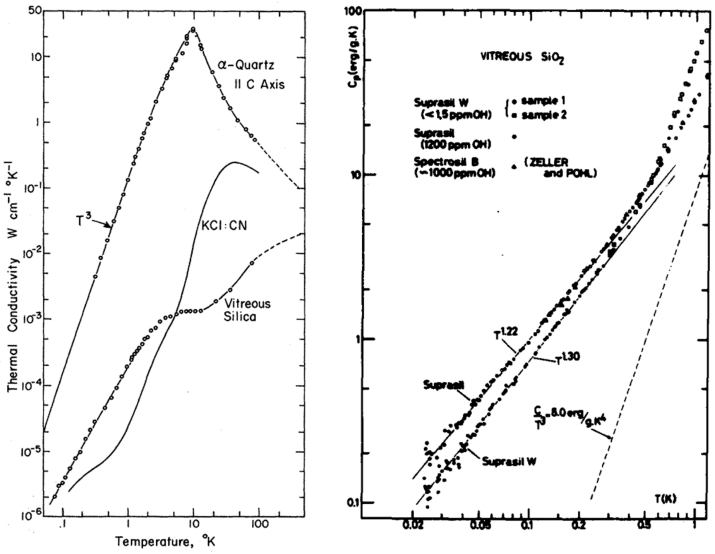


Figure 2.7: (a) Thermal conductivity of vitreous (amorphous) quartz and crystal quartz at low temperatures. The vitreous quartz shows a much smaller thermal conductivity and has a different temperature dependency ($\propto T^2$) at very low temperatures compared to the crystal one ($\propto T^3$). Data from Ref. [4]. (b) specific heat of vitreous quartz and crystal quartz at low temperatures. Below 0.5 K the specific heat $C_p$ of the vitreous quartz is proportional to $T^{1.3}$, deviating from the Debye model. Data from Ref. [5]

including TLS-TLS interaction.

### 2.2.1 Amorphous glass behaviors in low temperature

Amorphous materials are referred to as glassy materials. Below 1 K, glassy materials, regardless of the structure or composition, are quantitatively very similar in the phonon scattering properties including the specific heat [78], thermal conductivity [79] and the resonant ultrasonic attenuation [80]. It has been known for some time, but the explanation is mainly phenomenological.

In crystals, long-wavelength phonons from the collective excitation of the lattice are responsible for both the transport of heat and the specific heat of crystals. In the Debye model, we introduce $\omega = vq$, where the phonon frequency $\omega$, the speed of sound in the crystal $v$, and the

wave number $q$. The phonon density of states $D(\omega)$ is related to the volume $V_n$ of the solid and is given by

$$D\left(\omega\right)d\omega = \frac{V_n}{2\pi^2}\frac{\omega^2}{v^3}\,d\omega. \tag{2.19}$$

The heat capacity $C_V$ can be calculated from the small change of internal energy $U$ over temperature at a fixed volume $V$ and

$$C_V = \left(\frac{\partial U}{\partial T}\right)_V = \frac{\partial}{\partial T}\int_0^{\omega_D} \hbar\omega D\left(\omega\right) f\left(\omega, T\right) d\omega, \tag{2.20}$$

where Bose-Einstein distribution

$$f\left(\omega, T\right) = \frac{1}{e^{\frac{\hbar\omega}{k_B T}} - 1}. \tag{2.21}$$

Since the total number of atoms $N$ is the integral of $D\left(\omega\right)$ from 0 to a cut-off $\omega_D$, we get

$$N = \int_0^{\omega_D} D\left(\omega\right) d\omega. \tag{2.22}$$

For low temperatures, Eq. 2.20 can be solved analytically, and I obtain the well-known $T^3$-dependency of

$$C_V = \frac{12\pi^4}{5}\, N\, k_B \left(\frac{T}{\theta}\right)^3, \tag{2.23}$$

where Debye temperature $\theta = \frac{\hbar\omega_D}{k_B}$. The thermal conductivity $\kappa_{th}$ can be treated within the framework of the kinetic theory of gases considering the transport processes of a phonon gas $\kappa_{th} = \frac{1}{3} C_V\, v\, l$, whereas $l$ is the mean free path of the phonons. At low temperatures, the phonon-phonon scattering is negligible. In the case of a crystalline solid, the mean free path is limited by

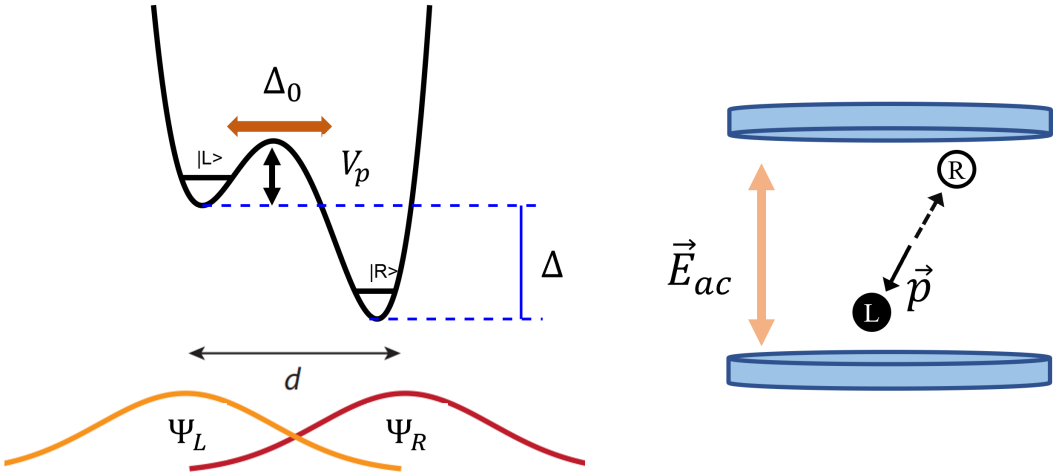


Figure 2.8: (a) Drawing of a double-well potential. $V_p$ is the barrier height separating the two wells, $\Delta$ is the asymmetry energy (energy difference between right and left well), $\Delta_0$ is the tunneling energy, and $d$ is the spatial separation of the potential minima. The tunneling object has a mass $m$ in an isolated single harmonic well $\Psi_{L/R}$. (b) A TLS with the dipole moment $\boldsymbol{p} = q\boldsymbol{d}/2$, under an external AC electric field $\vec{E}_{ac}$.

the sample's diameter itself $l \approx$ constant. A $T^3$-dependence of the phononic heat conductivity $\kappa_{th}$ is expected as well. $\kappa_{th} \propto T^3$ is observed in a crystal quartz as shown in Fig. 2.7 left panel. However, specific heat $C_p \propto T^{1.3}$ and $\kappa_{th} \propto T^2$ are seen in vitreous quartz which is a disordered material.

### 2.2.2 Standard tunneling model

Several models are proposed to explain these discrepancies. Among them, a microscopic model proposed independently by Phillips [77] and Anderson et al. [76] is the most successful. The theory is known as the standard tunneling model (STM) [76, 77], describing a tunneling object might be a single atom or a group of atoms with mass $m$. The tunneling object lives in two equilibrium isolated well states (left well $|L\rangle$ and right well $|R\rangle$) which differ by the energy $\Delta$

and are separated by the potential barrier height $V_p$. Since the transition energy to the first excited state from the ground state in each isolated well is far larger than any other energy scale, we can ignore any excited states in single well. The barrier height is chosen to be general soft-potential such that the overlap of the two well's wavefunction is considered as perturbation. Therefore, the Hamiltonian $\mathcal{H}_0 = \mathcal{H}_L + \mathcal{H}_R + V_{int}$, where $\mathcal{H}_L$ and $\mathcal{H}_R$ are the Hamiltonian of left and right well, respectively, and $V_{int}$ is the interaction of two wells. It is equivalent to

$$\mathcal{H}_0 = \begin{pmatrix} \varepsilon_L + \langle L| V_{int} |L\rangle & \langle L| \mathcal{H}_0 |R\rangle \\ \langle L| \mathcal{H}_0 |R\rangle^* & \varepsilon_R + \langle R| V_{int} |R\rangle \end{pmatrix} \tag{2.24}$$

in the basis of the ground states of the two wells ($|L\rangle$ and $|R\rangle$).

It is convenient to assume $\langle L| V_{int} |L\rangle$ and $\langle R| V_{int} |R\rangle$= 0. One typically uses the expression $\langle L| \mathcal{H}_0 |R\rangle /2 = \Delta_0 = \hbar\Omega e^{-\lambda_p}$ obtained from the WKB approximation. Here

$$\Omega = 4\left(\frac{2V_p^2}{\hbar^2 m d^2}\right)^{\frac{1}{4}} \text{ and } \lambda_p \approx \frac{d}{2\hbar}\sqrt{2mV_p} \tag{2.25}$$

and the distance of two wells is $d$. Therefore, a simplified Hamiltonian

$$\mathcal{H}_0 = \frac{1}{2}\begin{pmatrix} -\Delta & \Delta_0 \\ \Delta_0 & \Delta \end{pmatrix}, \tag{2.26}$$

where asymmetry energy $\Delta = \varepsilon_R - \varepsilon_L$.

In the STM, the TLSs are believed to have a uniform spatial distribution in a bulk amorphous dielectric. Also, the TLS spectral distributions in $\Delta$ and $V_p \propto \log(\Delta_0)$ are assumed to be

uniform as well. Therefore, the energy distribution of TLSs per volume can be written as

$$d^2n = P_0\, d\Delta\, d\left(\log(\Delta_0)\right) = \; P_0\, \frac{d\Delta_0}{\Delta_0}\, d\Delta, \tag{2.27}$$

where $P_0$ is a material-related constant denoting the TLS spectral and spatial density and has a typical value of $10^{44} J^{-1} m^{-3}$. It is useful to write the distribution in the basis of TLS energy $E_{tls} = \sqrt{\Delta^2 + \Delta_0^2}$:

$$d^2n = P_0 \left| \frac{\partial \Delta}{\partial E_{tls}} \right| dE_{tls}\, d\Delta_0 = P_0 \frac{E_{tls}}{\Delta_0} \frac{1}{\sqrt{E_{tls}^2 - \Delta_0^2}}\, dE_{tls}\, d\Delta_0. \tag{2.28}$$

The integration over $\Delta_0$ yields the density of states

$$D(E) = \int_{\Delta_{0,min}}^{E} d^2n = P_0 \ln\left(\frac{2E}{\Delta_{0,min}}\right) \approx D_0. \tag{2.29}$$

Here, $\Delta_{0,min}$ is the low energy cutoff and $D(E_{tls})$ is usually approximated as a constant $D_0$ over our measurement range.

### 2.2.3 Field absorption by TLSs

If charges are involved in a tunneling process of a distance, the system owns a dipole moment which I denoted $\mathbf{p} = \frac{q\mathbf{d}}{2}$. For small fields, one can use the first order perturbation theory and add the perturbation $\mathcal{H}_1 = \delta H_0$ into the unperturbed Hamiltonian $\mathcal{H}_0$:

$$\mathcal{H} = \mathcal{H}_0 + \mathcal{H}_1 = \; \frac{1}{2} \begin{pmatrix} -(\Delta + \delta\Delta) & \Delta_0 + \delta\Delta_0 \\ \Delta_0 + \delta\Delta_0 & \Delta + \delta\Delta \end{pmatrix}. \tag{2.30}$$

Under the field $\mathbf{F}$, it is assumed that the modification on the barrier height $V_p$ is ignorable so that $|\delta\Delta| \gg |\delta\Delta_0| \approx 0$. The field changes $\Delta$ linearly as $\delta\Delta = 2\mathbf{p}\cdot\mathbf{F} = 2|\mathbf{p}|\,|\mathbf{F}|\cos\theta$, where $\theta$ is the angle between $\mathbf{p}$ and $\mathbf{F}$. Experiments like [9, 81] strongly support this assumption. For convenience, here we discuss electrical dipoles and there is no change of the concept from $\mathbf{p}$ to a strain dipole moment [81] or a magnetic dipole moment. However, the effect of magnetic dipole moment is less studied [82, 83]

Applying an unitary matrix to diagonalize $\mathcal{H}_0$, the new Hamiltonian is $\mathcal{H}' = \mathcal{H}'_0 + \mathcal{H}'_1$, where

$$\mathcal{H}'_0 = \frac{E_{tls}}{2}\sigma_z, \tag{2.31}$$

$$H'_1 = \left[\frac{\Delta}{E_{tls}}\sigma_z + \frac{\Delta_0}{E_{tls}}\sigma_x\right]\mathbf{p}\cdot\mathbf{F},. \tag{2.32}$$

If $\mathbf{F}$ is oscillating with frequency $\omega$ and $\mathbf{F} = \mathbf{F}_{ac}\cos\omega t$, $\mathcal{H}'$ is equivalent to a classical spin-$\frac{1}{2}$ rotating under a magnetic field $\vec{B}$: $\mathcal{H}_{spin} = -\gamma_e\vec{B}\cdot\vec{S}$, where $\gamma_e$ is the gyromagnetic ratio and $\vec{S}$ is the spin vector. We can map $\mathcal{H}'$ to $\mathcal{H}_{spin}$ by a total magnetic field $B(t)$, which is a combination of a strong static field $B_{0,z}$ in z-direction and an oscillating perturbation field $B_1(t)$ in x- and z-direction:

$$B(t) = B_{0,z} + B_1(t) = \begin{pmatrix} B_{1,x}\cos(\omega t) \\ 0 \\ B_{0,z} + B_{1,z}\cos(\omega t) \end{pmatrix}. \tag{2.33}$$

The relationship of between the magnetic fields and TLS parameters is

$$\begin{aligned} -\gamma_e \hbar B_{0,z} &= E_{tls} \\ -\gamma_e \hbar B_{1,x}(t) &= 2\frac{\Delta_0}{E_{tls}}\,\mathbf{p}\cdot\mathbf{F}(t) \\ -\gamma_e \hbar B_{1,z}(t) &= 2\frac{\Delta}{E_{tls}}\,\mathbf{p}\cdot\mathbf{F}(t). \end{aligned} \tag{2.34}$$

The dynamics of the spin is described by the well-known Bloch equations [84]:

$$\begin{aligned} \frac{d}{dt}\langle S_x\rangle &= \gamma_e\left[\langle S_y\rangle B_z(t) - \langle S_z\rangle B_y\right] - \Gamma_2\langle S_x\rangle \\ \frac{d}{dt}\langle S_y\rangle &= \gamma_e\left[\langle S_z\rangle B_x(t) - \langle S_x\rangle B_z\right] - \Gamma_2\langle S_y\rangle \\ \frac{d}{dt}\langle S_z\rangle &= \gamma_e\left[\langle S_x\rangle B_y(t) - \langle S_y\rangle B_x\right] - \Gamma_1\left(\langle S_z\rangle - \langle S_z\rangle_{eq}\right). \end{aligned} \tag{2.35}$$

Here $\langle S_i\rangle$ is the ensemble average of the spin operator, $\Gamma_1$ and $\Gamma_2$ are the relaxation and decoherence rate of the spin, respectively, and $\langle S_z\rangle_{eq}$ is the spin z-component when $t\to\infty$. With a new set of definitions

$$\begin{aligned} \boldsymbol{F} &= \frac{1}{2}\boldsymbol{F_{ac}}\left(e^{i\omega t}+e^{-i\omega t}\right) \\ \xi &= \frac{\Delta_0}{E_{tls}} \\ \hbar\Omega_0 &= |\mathbf{p}||\boldsymbol{F_{ac}}|\cos\theta = p\,F_{ac}\cos\theta \\ \omega_0 &= \frac{E_{tls}}{\hbar}, \end{aligned} \tag{2.36}$$

we simplify Eq. 2.34 to

$$\begin{aligned} \gamma_e B_{0,z} &= -\omega_0 \\ \gamma_e B_{1,x}(t) &= -\xi\,\Omega_0\left(e^{i\omega t}+e^{-i\omega t}\right) \\ \gamma_e B_{1,z}(t) &= -\sqrt{1-\xi^2}\,\Omega_0\left(e^{i\omega t}+e^{-i\omega t}\right). \end{aligned} \tag{2.37}$$

Substituting Eq. 2.35 by Eq. 2.37 and $m_0 = \langle S_z \rangle_{eq} = \frac{1}{2}\tanh\left(\frac{\hbar\omega_0}{2k_BT}\right)$, I have

$$\begin{aligned}
\frac{d}{dt}\langle S_x \rangle &= \omega_0 \langle S_y \rangle - \Gamma_2 \langle S_x \rangle \\
\frac{d}{dt}\langle S_y \rangle &= \left[\omega_0 + \sqrt{1-\xi^2}\,\Omega_0\,\left(e^{i\omega t} + e^{-i\omega t}\right)\right]\langle S_x \rangle - \Gamma_2 \langle S_y \rangle - \xi\,\Omega_0\,\left(e^{i\omega t} + e^{-i\omega t}\right)\langle S_z \rangle \\
\frac{d}{dt}\langle S_z \rangle &= \xi\,\Omega_0\,\left(e^{i\omega t} + e^{-i\omega t}\right)\langle S_y \rangle - \Gamma_1\left(\langle S_z \rangle - m_0\right).
\end{aligned} \tag{2.38}$$

To solve the Bloch equations, I write all three components, $\langle S_x \rangle$, $\langle S_y \rangle$ and $\langle S_z \rangle$, in a sum of frequency components at $\omega_k = k \cdot \omega$ for $k \in \mathbf{Z}$ and $\langle S_i \rangle = \sum_k S_{i,k} e^{i\omega_k t}$ and $S_{i,k} = S^*_{i,-k}$ for $i = x,\ y,\ z$ .

Comparing the existing $\omega$ term, only the terms with $k$ = -1, 0, and 1 survive. In addition, since when $t \to \infty$, $S_{x,0}$ and $S_{y,0}$ are irreverent, $S_{x,0} = S_{y,0}$ = 0. Along with $S_1^{\pm} = S_{x,1} \pm iS_{y,1}$, I obtain

$$\frac{d}{dt}S_1^+ = i\left[(\omega_0 - \omega) + i\Gamma_2\right]S_1^+ - i\xi\Omega_0 S_{z,0} \tag{2.39}$$

and

$$\frac{d}{dt}S_{z,0} = \xi\,\Omega_0\ \mathrm{Im}\left(S_1^+\right) - \Gamma_1(S_{z,0} - m_0). \tag{2.40}$$

The stationary solution

$$S_1^+ = \frac{\xi\,\Omega_0\,(\omega - \omega_0 - i\Gamma_2)m_0}{(\omega - \omega_0)^2 + \Gamma_2^2 + \xi^2\,\Omega_0^2\,\Gamma_2\,\Gamma_1^{-1}}. \tag{2.41}$$

Eq. 2.41 can be seen as a single dipole being polarized by the field. Since the dipole moment after unitary transformation in the off-diagonal part of Eq. 2.32 is now $\xi\mathbf{p}$, we define the dipole operator $\hat{\pi} = |\mathbf{p}|\cos\theta\,\xi\,S_1^+$ [85]. The collective effect of the polarization $P_d = \sum_{TLS}\hat{\pi}$ is the summation of all TLSs and the polarization energy is $P_d F_{ac}$. The power dissipation density $P_{tls}$

is given by the time average of the imaginary part of the polarization energy, and

$$P_{tls} = \mathrm{Im}\left\langle \frac{\omega}{2} F_{ac} \sum_{TLS} \hat{\pi} \right\rangle. \tag{2.42}$$

The ratio of $P_{tls}$ to the storage power density in the dielectric film $\frac{1}{2}\epsilon F_{ac}^2$ is the definition of loss tangent

$$\tan\delta = \frac{P_{tls}}{\frac{\omega}{2}\epsilon F_{ac}^2} = \frac{1}{\epsilon}\sum_{TLS} \frac{p\,\cos\theta\,\xi^2\frac{\Omega_0}{F_{ac}}\,\Gamma_2\,m_0}{(\omega-\omega_0)^2+\Gamma_2^2+\xi^2\,\Omega_0^2\,\Gamma_2\Gamma_1^{-1}} = \frac{1}{\epsilon}\sum_{TLS} \frac{p^2\,\cos^2\theta\,\xi^2\,\Gamma_2\,m_0}{(\omega-\omega_0)^2+\Gamma_2^2+\xi^2\,\Omega_0^2\,\Gamma_2\Gamma_1^{-1}}. \tag{2.43}$$

In the assumption of uniform TLS density in $\Delta$, $\log\Delta_0$, and $\cos\theta$ (i.e., isotropic $\mathbf{p}$ and $|\mathbf{p}| = p$, the integration of Eq. 2.43 over all TLSs is

$$\tan\delta = \frac{P_0\,p^2}{\epsilon}\int_{\Delta_{min}}^{\Delta_{max}} d\Delta \int_{\Delta_{0,min}}^{\Delta_{0,max}} \frac{d\Delta_0}{\Delta_0}\int_{-1}^{1} d(\cos\theta)\frac{\cos^2\theta\,\Gamma_2^{-1}\,m_0}{1+(\omega-\omega_0)^2\Gamma_2^{-2}+\xi^2\,\Omega_0^2\,\Gamma_2^{-1}\Gamma_1^{-1}}. \tag{2.44}$$

Eq. 2.43 is an approximation of Eq. (G.2) in Ref. [86] when $\omega+\omega_0 \gg \Gamma_2$. Proven in Ref. [86], the integration over $\theta$ is solely associated to $p$ and is equivalent to replacing $p^2$ by averaged $\langle p^2\rangle = \frac{p^2}{3}$.

According to Ref. [76], the energy decay of a TLS is only via TLS-phonon coupling (i.e., phonon emission and absorption), and

$$\Gamma_1 = \left(\frac{\Delta_0}{E_{tls}}\right)^2 \Gamma_{1,min} \tag{2.45}$$

$$\Gamma_{1,min} = \Gamma_{1,0}\,E_{tls}^3\,\coth\left(\frac{E_{tls}}{2k_BT}\right), \tag{2.46}$$

where $\Gamma_{1,0}$ is a constant depending on the material intrinsic properties such as sound velocity and mass density of the material [76, 86]. When TLS-TLS interaction is ignorable, $\Gamma_1 = 2\Gamma_2$, I can simplify Eq. 2.44 to the well-known power-dependent loss tangent

$$\tan\delta = \frac{\pi P_0\, p^2}{3\epsilon} \frac{\tanh\left(\frac{\hbar\omega}{2\,k_B\,T}\right)}{\sqrt{1+\left(\frac{\Omega_0}{\Omega_c}\right)^2}}, \tag{2.47}$$

where $\Omega_c = \sqrt{3\,\Gamma_1\,\Gamma_2}$. When $F_{ac}$ is an electrical field, we have $F_{ac} = E_{ac} = \langle\beta|\, E_{zpf}(a^\dagger + a)\,|\beta\rangle = 2\sqrt{n_{ph}}E_{zpf}$, where $|\beta\rangle$ is a coherent state (and $\beta$ is a real number) and $n_{ph} = \beta^2$ is the photon number mentioned in Chapter 2.1.6. Since $n_{ph}$ is generally more accessible than $E_{ac}$ which can be geometric-dependent (especially in planar resonators), it is useful to transfer the equation from $\Omega_0$ to $n_{ph}$ by

$$\left(\frac{\Omega_0}{\Omega_c}\right)^2 = \left(\frac{4p^2\,E_{zpf}^2\,n_{ph}}{3\,\hbar^2\,\Gamma_1\,\Gamma_2}\right) = \frac{n_{ph}}{n_c} \tag{2.48}$$

and

$$n_c = \frac{3\,\hbar^2\,\Gamma_1\,\Gamma_2}{4p^2\,E_{zpf}^2}. \tag{2.49}$$

The TLS loss at a small field ($n_c \gg n$) is called "single-photon" loss

$$\tan\delta_{tls}^0 = \frac{\pi P_0\, p^2}{3\epsilon}. \tag{2.50}$$

However, there are differences between the approximated solution Eq. 2.47 and a full numerical integration of Eq. 2.44 when $\Gamma_1 \ll \Gamma_2$. The calculations of the full integration at

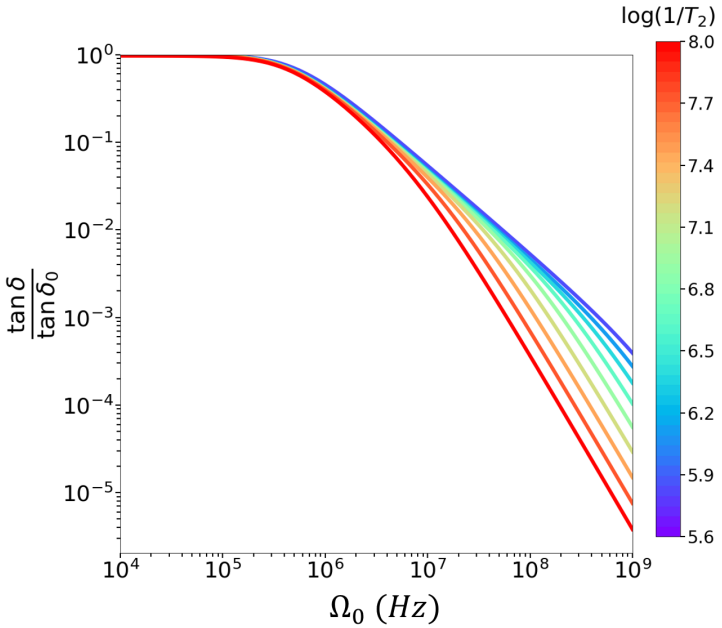


Figure 2.9: Power-dependent loss tangent $\tan\delta$ derived from a full numerical integration of Eq. 2.44. The color represents different values of $T_2$ (sec) and all curves have a constant $T_1T_2 = 10^{-11}(\text{sec}^2)$. The constant value of $T_1T_2$ ensures the $\Omega_c$ is the same for all curves. When $T_2$ is close to $T_1$, $\tan\delta$ can be approximated to Eq. 2.47, e.g., the violet curve.

various $T_2$ (sec) are shown in Fig. 2.9. A constant $T_1T_2$ (sec$^2$) ensures the $\Omega_c$ is the same for all curves. When $T_2$ is small and $T_1$ is large (e.g. the red curve), we observe the loss tangent would deviate from Eq. 2.47 at large $\Omega_0$. Only if $T_2 \approx T_1$ as shown in the violet curve, Eq. 2.47 is a good approximation of Eq. 2.44.

### 2.2.4 TLS loss in microwave resonator

Several different mechanisms can contribute to the loss of energy in a superconducting resonator. To quantify these losses, we characterize the different contributions and the general expression for the internal quality factor is given by

$$\frac{1}{Q_i} = \frac{1}{Q_{tls}} + \frac{1}{Q_{qp}} + \frac{1}{Q_{rad}} + ..., \tag{2.51}$$

where $Q_{tls}$ is TLS-related and a function of power and temperature, $Q_{qp}$ is quasiparticle-related and a function of power and temperature, and $Q_{rad}$ is radiation-related. Since only the TLS loss decreases with power and most of other loss mechanisms are power-insensitive or slightly increasing with power, we can determine the TLS loss

$$\tan\delta_{tls} = \frac{1}{Q_{i,tls}} \approx \frac{1}{Q_{i,L}} - \frac{1}{Q_{i,H}}, \tag{2.52}$$

where $Q_{i,L}$ and $Q_{i,H}$ are the internal quality factor at low (or single-photon) and high power. Since TLSs are generally located in dielectric, TLS loss is called dielectric loss as well.

The geometry of superconducting qubits or resonators contains dielectric loss from various materials or components $k$. TLS loss contribution from region with a volume $V_k$ can be understood by the filling factor $F_{r,k}$ times its loss tangent $\tan\delta^k$ and

$$F_{r,k} = \frac{\int_{V_k} \varepsilon(\mathbf{r})\,|E_0(\mathbf{r})|^2\,d\mathbf{r}^3}{\int \varepsilon(\mathbf{r})\,|E_0(\mathbf{r})|^2\,d\mathbf{r}^3}, \tag{2.53}$$

where $\varepsilon(\mathbf{r})$ is the dielectric constant, $E_0$ is the electric field and $\mathbf{r}$ is the position. The total loss tangent is written as

$$\tan\delta_{tls} = \sum_k F_{r,k}\tan\delta^k. \tag{2.54}$$

In Ref. [87], they characterize intrinsic $\tan\delta_0^k$ from different interfaces and substrate by various resonators designs. They realize the limitation of $Q_i$ is from the superconducting surface or substrate surface which has $\tan\delta \approx 10^{-2} \sim 10^{-3}$ and the loss from Si substrate is usually small with $\tan\delta_{Si} = 2.6 \times 10^{-7} \pm 4 \times 10^{-8}$.

A strategy to lower $\tan\delta_{tls}$ is lowering $F_{r,k}$ by the geometry of the resonators. For instance,

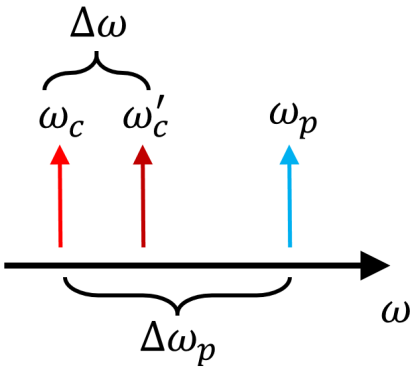


Figure 2.10: The pumping tone $\omega_p$ causes the original resonator frequency $\omega_c$ to shift to the final resonance $\omega_c'$

due to a large vacuum volume in the 3D cavity, most of the energy is stored in the lossless vacuum and the filling factor on the metal surface is minimized. It results in a high $Q_i > 10^7$ and the photon lifetime $\geq 100$ $\mu$s [70].

### 2.2.5 TLS two-tone spectroscopy

Here, I will introduce the technique [88, 89] to extract the TLS's Rabi frequency from two-tone spectroscopy and derive the equations of frequency and loss tangent shifts in the resonator. The two-tone technique uses a second strong pumping tone to saturate the TLS asymmetrically to cavity resonance. For a saturation tone detuned $\Delta\omega_p = \omega_p - \omega_c > 0$ from the original resonator frequency $\omega_c$, both the resulting resonance $\omega_c'$ and internal quality factor $Q_i'$ would increase because of the reduced TLS ground-state population on the upper side of $\omega_c$. See Fig. 2.10 for illustration of the tones.

First of all, I start by deriving the small complex frequency shift due to a single TLS. From the Jaynes-Cummings Hamiltonian and a pumping tone at frequency $\omega_p$, we have

$$\mathcal{H} = \hbar\omega_c a^\dagger a + \frac{\hbar\omega_{tls}}{2}\sigma_z + \hbar\, g\, \left(a^\dagger\sigma_- - a\sigma_+\right) + \hbar J\left(a^\dagger e^{-i\omega_p t} - a e^{i\omega_p t}\right), \tag{2.55}$$

where $a$ is the annihilation cavity operator, $\omega_c$ is the cavity frequency, $\omega_{tls}$ is the TLS frequency, $g = \frac{\Omega}{2}$ is the TLS-cavity coupling strength, $\vec{\sigma}$ is the TLS spin operator, and $J$ is the strength of the pumping tone. To cancel out the rotating part $e^{i\omega_p t}$, I apply a unitary operator $U = e^{i\omega_p t a^\dagger a}$ and the Hamiltonian in the rotating frame is

$$\widetilde{\mathcal{H}}(t) = i\frac{dU}{dt}\,U^\dagger + U\mathcal{H}U^\dagger. \tag{2.56}$$

Since

$$e^{i\alpha a^\dagger a} a e^{-i\alpha a^\dagger a} = e^{-i\alpha} a, \tag{2.57}$$

$$e^{i\alpha a^\dagger a} a^\dagger e^{-i\alpha a^\dagger a} = e^{i\alpha} a^\dagger, \tag{2.58}$$

and

$$\frac{dU}{dt} U^\dagger = i\omega_p a^\dagger a, \tag{2.59}$$

I have

$$\widetilde{\mathcal{H}}(t) = (\omega_c - \omega_p)\, a^\dagger a + \frac{\hbar\omega_{tls}}{2}\sigma_z + \hbar\, g\, \left(a^\dagger \sigma_- e^{i\omega_p t} - a\sigma_+ e^{-i\omega_p t}\right) + \hbar J\left(a^\dagger - a\right). \tag{2.60}$$

A second rotating unitary $U' = e^{i\omega_p t \frac{\sigma_z}{2}}$ is applied to $\widetilde{\mathcal{H}}(t)$ with rules of

$$e^{i\alpha\frac{\sigma_z}{2}} \sigma_- e^{-i\alpha\frac{\sigma_z}{2}} = e^{-i\alpha}\sigma_- \tag{2.61}$$

and

$$e^{i\alpha\frac{\sigma_z}{2}} \sigma_+ e^{-i\alpha\frac{\sigma_z}{2}} = e^{i\alpha}\sigma_+. \tag{2.62}$$

I have

$$\widetilde{\mathcal{H}}'(t) = (\omega_c - \omega_p)\, a^\dagger a + \frac{\hbar(\omega_{tls} - \omega_p)}{2}\sigma_z + \hbar\, g\, \left(a^\dagger \sigma_- - a\sigma_+\right) + \hbar J\left(a^\dagger\ - a\right). \tag{2.63}$$

The dissipation of TLS density matrix $\rho$ is described by the Lindblad equation [54] mentioned in Eq. 1.9:

$$\frac{d\rho}{dt} = -\frac{i}{\hbar}\left[\widetilde{\mathcal{H}}', \rho\right] + \Gamma_1 D_\sigma(\rho) + \frac{\Gamma_\phi}{2} D_{\sigma_z}(\rho) + \Gamma_r D_a(\rho), \tag{2.64}$$

where $\Gamma_1$ and $\Gamma_\phi$ are the relaxation and the dephasing rate of TLS, $\Gamma_r$ is the cavity photon decay rate. Using the fact that $\langle \mathbf{A} \rangle = \mathrm{Tr}(\mathbf{A}\rho)$, we yield equations similar to Eq. 2.38:

$$\frac{d}{dt}\langle a\rangle = \left(-i\Delta_r - \frac{\Gamma_r}{2}\right)\langle a\rangle - ig\langle\sigma_-\rangle + J \tag{2.65}$$

$$\frac{d}{dt}\langle\sigma_-\rangle = (-i\Delta_{tls} - \Gamma_2)\langle\sigma_-\rangle - ig\langle a\sigma_z\rangle \tag{2.66}$$

$$\frac{d}{dt}\langle\sigma_z\rangle = -2ig\left(\langle a^\dagger\sigma_-\rangle + \langle a\sigma_+\rangle\right) - \Gamma_1(\langle\sigma_z\rangle - m_0), \tag{2.67}$$

where $\Delta_{tls} = \omega_{tls} - \omega_p$ and $\Delta_r = \omega_c - \omega_p$. Note that $m_0 = \tanh\left(\frac{\hbar\omega_{tls}}{2k_BT}\right)$. From the derivation of the Bloch equations in Chapter 2.2.3, we know only the terms of $\omega_m$ with m = -1,0,1 are important. I decompose $\langle a\rangle$ to a semi-classical stationary components ($\alpha$) and modulated components $\delta a(t)e^{i\Delta_r t}$, where $\delta a(t)$ is a slow varying function:

$$\langle a\rangle = \alpha + \delta a(t)e^{i\Delta_r t}. \tag{2.68}$$

The same decomposition process applies to $\langle\sigma_-\rangle$ and $\langle\sigma_z\rangle$:

$$\langle\sigma_-\rangle = \sigma_{-,0} + \delta\sigma_-(t)e^{i\Delta_r t} \tag{2.69}$$

and

$$\langle\sigma_z\rangle = \sigma_{z,0} + \delta\sigma_z(t)e^{i\Delta_r t}. \tag{2.70}$$

From the hindsight of the Bloch solution, $\langle\sigma_z\rangle$ has no oscillating term when $t \to \infty$ and $\delta\sigma_z(t) = 0$. The semi-classical stationary solutions are

$$0 = \left(-i\Delta_r - \frac{\Gamma_k}{2}\right)\alpha - \ ig\sigma_0 + J \tag{2.71}$$

$$0 = \left(-i\Delta_{tls} - \Gamma_2\right)\sigma_{-,0} - ig\alpha\sigma_{z,0} \tag{2.72}$$

$$0 = \ 2ig\left(\alpha^*\sigma_{-,0} + \alpha\sigma^*_{-,0}\right) - \Gamma_1(\sigma_{z,0} - m_0). \tag{2.73}$$

We obtain

$$\sigma_{-,0} = -\frac{ig\alpha\sigma_{z,0}}{i\Delta_{tls} + \Gamma_2} \tag{2.74}$$

and

$$\sigma_{z,0} = \ m_0\left(1 - \frac{4\Gamma_2\Gamma_1^{-1}\,g^2\,n_{pu}}{\Delta_{tls}^2 + \Gamma_2^2\left(1 + 4g^2 n_{pu}\Gamma_1^{-1}\Gamma_2^{-1}\right)}\right), \tag{2.75}$$

where we denote the photon number in the cavity from pumping tone is $n_{pu} = |\alpha|^2$. The Rabi frequency is given by

$$\Omega = 2g\sqrt{n_{pu}} = 2\frac{\Delta_0}{\hbar^2\omega_{tls}} p\,E_{zpf}\cos\theta\sqrt{n_{pu}}. \tag{2.76}$$

For considering only the oscillating terms and a slow TLS dynamic, I can adiabatically

eliminate $\frac{d}{dt}(\delta\sigma) = 0$ and get

$$\delta\dot{\alpha} = -\frac{\Gamma_r}{2}\delta\alpha - ig\delta\sigma_- \tag{2.77}$$

and

$$\delta\sigma_- = \frac{-ig\,\sigma_{z,0}\,\delta\alpha}{-i\,(\omega_c - \omega_{tls}) - \Gamma_2}. \tag{2.78}$$

Eventually, the small amplitude of $\delta\alpha$ is depending on the TLS state $\sigma_{z,0}$ by substituting Eq. 2.78 into Eq. 2.77:

$$\delta\dot{\alpha} = \left(-\frac{\Gamma_r}{2} + \frac{g^2\sigma_{z,0}}{i\,(\omega_c - \omega_{tls}) + \Gamma_2}\right)\delta\alpha. \tag{2.79}$$

The second term in parenthesis is a complex pull from the TLS

$$\delta\omega = \frac{g^2\sigma_{z,0}}{i\,(\omega_c - \omega_{tls}) + \Gamma_2}. \tag{2.80}$$

Noted that the real part of $\delta\omega$ is a frequency shift and the imaginary part $\mathrm{Im}(\delta\omega) = 2\,\delta\Gamma_r$.

After integrating $\delta\omega$ over TLS distribution ($\Delta_0$, $\omega_{tls}$, $\cos\theta$), I obtain the equations of resonator frequency shift $\Delta\omega = \omega_c\prime - \omega_c$ and a new internal quality $Q_i'$ [88] related to $\Omega$:

$$\frac{\Delta\omega}{\omega_c} = \frac{3\pi\tan\delta}{4\sqrt{2}}\,\frac{\Delta\omega_p}{\Omega_0}\,\frac{\sqrt{1+\frac{\Omega_0^2}{2\Delta\omega_p^2}}-1}{\sqrt{1+\frac{\Omega_0^2}{2\Delta\omega_p^2}}+1} \tag{2.81}$$

and

$$\frac{Q_i}{Q_i'} = \left(\frac{\Delta\omega_p}{\Omega_0}\right)^2\left\{6 + 3\sqrt{1+2\left(\frac{\Delta\omega_p}{\Omega_0}\right)^2}\,\ln\left(1+\left(\frac{\Delta\omega_p}{\Omega_0}\right)^{-2}\left[1-\sqrt{1+2\left(\frac{\Delta\omega_p}{\Omega_0}\right)^2}\right]\right)\right\}, \tag{2.82}$$

where the maximum Rabi frequency $\hbar\Omega_0 = \frac{2}{\sqrt{3}}pE_{zpf}\sqrt{n_{pu}}$ (considering the averaging factor of

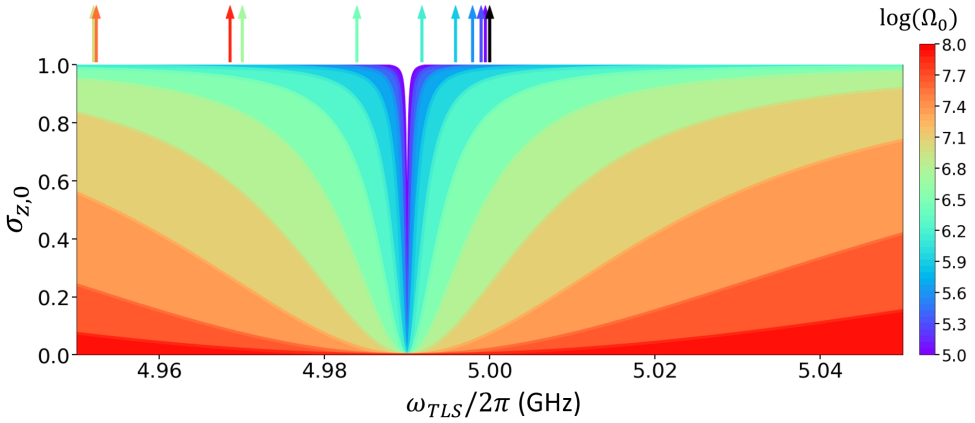


Figure 2.11: TLS ground state polulation $\sigma_{z,0}$ calculated from Eq. 2.75 versus TLS frequency over various TLS Rabi frequencies $\Omega$. A detuned tone pumps is at 4.99GHz and the resonator frequency is at 5GHz. The color represents the strength of pumping related to $\Omega$. On the top, arrows represents the shifted resonator frequency at different $\Omega$.

$\sqrt{3}$ for $p$). $n_{pu}$ can be obtained from the pumping power $P_{in}$ (see Chapt. 2.1.6) by

$$n_{pu} = \frac{2\kappa}{4\Delta\omega_p^2 + \kappa_{tot}^2} \frac{P_{in}}{\hbar\omega_p}. \tag{2.83}$$

Here $\kappa_{tot}$ and $\kappa$ are the total and external decay rate of the resonator.

$\sigma_{z,0}$ and resonator frequency shift from the calculations at various Rabi frequency are shown in Fig. 2.11. I plot $\sigma_{z,0}$ vs $\omega_{tls}$ over different $\Omega_0$ ($\propto \sqrt{n_{pu}}$) with a detuned pump at $\omega_p$ = 4.99GHz. On the top of the figure, I show $\omega'$ from its original resonance $\omega_c = 2\pi \cdot 5$ GHz. Fig. 2.12 shows $\Delta\omega$ versus the pump frequency. Each color represents a different $\Omega$. On the top of Fig. 2.12, I show the maximum of $\Delta\omega$ at each $\Omega_0$, and there is a saturate phenomenon in the maximum of $\Delta\omega$ which depends on the TLS single photon loss tangent obtained in Eq. 2.50.

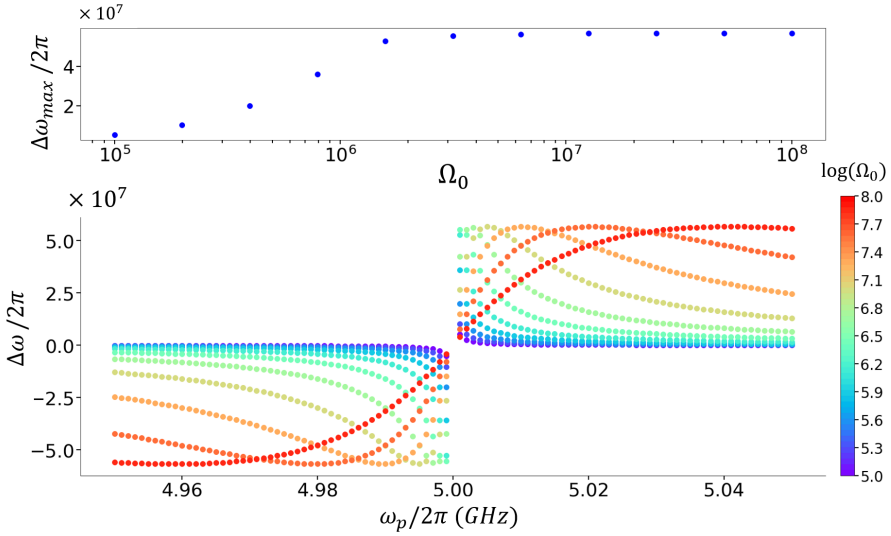


Figure 2.12: Frequency shift of the resonator $\Delta\omega = \omega_c' - \omega_c$ versus the pump frequency. Each color corresponds to a different TLS Rabi frequency $\Omega_0$, which positively related to the pumping power, ranging from $10^5$ to $10^8$ Hz. Points correspond to the calculation from Eq. 2.81. On the top, I show the maximum resonance shift for each $\Omega_0$.

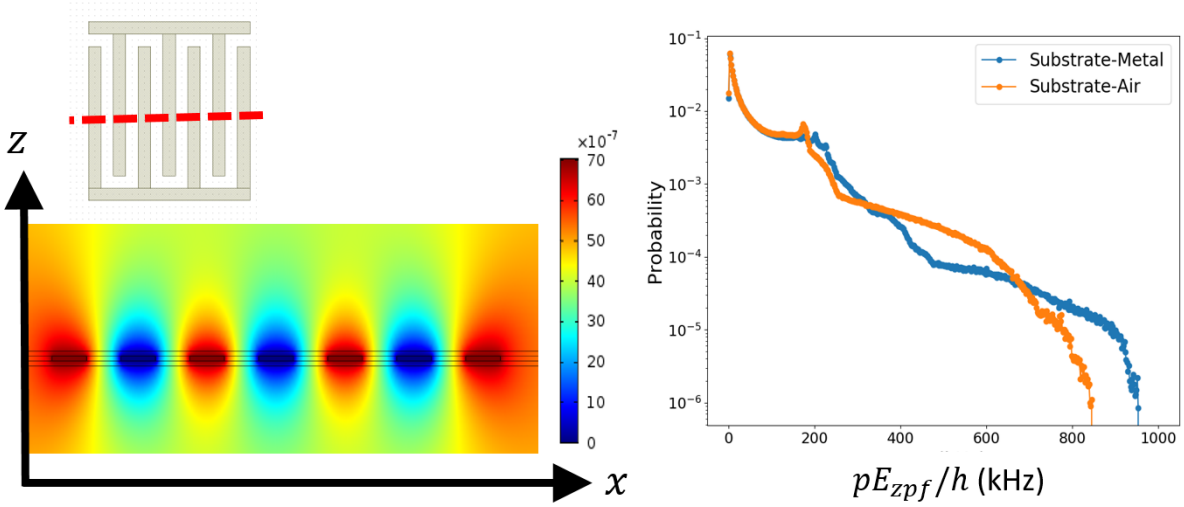


Figure 2.13: Left: The cross section of the simulated $E_{zpf}$ of IDC. IDC has width and gap = 0.5 $\mu$m. Right: The probability of $pE_{zpf}$ in substrate-metal or substrate-air interfaces. Since the wide spread of values, a single value $n_c$ is not preferred.

## 2.3 Puzzles in loss tangent

Sometimes, researchers find difficult to interpret their experiments in terms of Eq. 2.47. A phenomenological approach is adding a free fitting parameter $\phi$ (typically = 0.15 $\sim$ 0.4) [38, 90–93] in the denominator part of Eq. 2.47 and yields

$$\tan\delta = \tan\delta_{tls}^{0}\frac{\tanh\left(\frac{\hbar\omega}{2\,k_B\,T}\right)}{\left[1+\left(\frac{\Omega}{\Omega_c}\right)^2\right]^{\phi}}. \tag{2.84}$$

The motivation of $\phi$ comes from the non-negligible interactions between TLSs leading to frequency drifts of near-resonant TLSs caused by far-detuned TLSs such that stronger fields are required to saturate TLSs (see Chap. 2.3.1). However, those resonators with $\phi$ added are planar resonators which have position-dependent electric field distribution [94], and dielectric films may exhibit a wide spread of $p$ [9, 95], resulting in non-uniform $n_c$ which is a function of both parameters (Eq. 2.49). A simulation of $pE_{zpf}$ over interdigital-capacitor (IDC) with dipole moment $p$ = 2 Debye is shown in Fig. 2.13. As a result, instead of using a single $n_c$, we need to consider the different TLS effects (located in bulk or at the metal-air, substrate-air, and metal-substrate interfaces) contribute to the total loss tangent $1/Q_i$ [38, 90, 94]. Therefore, for scientific understanding, it is important to verify the correct explanation by some means. In the next two sections, I will provide the details for each explanation.

### 2.3.1 TLSs with mutual interactions

TLS models incorporating TLS interaction exist for describing the low temperature glassy material properties [96, 97]. A recent development in understanding TLS loss is that the TLS en-

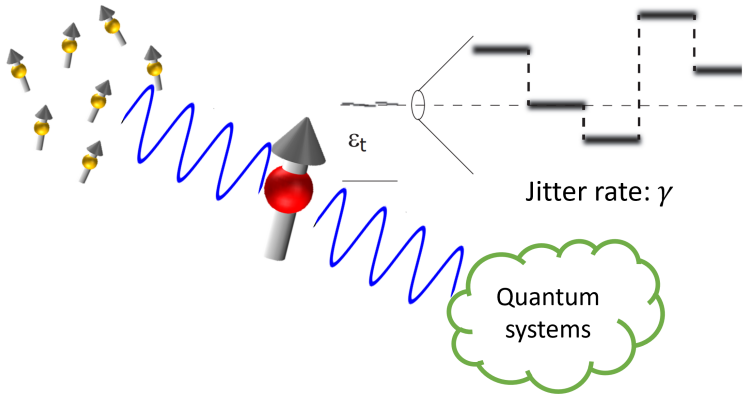


Figure 2.14: Interpretation of a coherent TLS (cTLS) coupled to thermal TLSs and quantum systems. A cTLS in red which has energy close to a certain quantum system, e.g., a resonator, interacts with low-frequency thermal TLSs in yellow. The quantum system is directly affected by the cTLS but not thermal TLSs. This cTLS energy is fluctuating over time depending on the states of thermal TLSs.

ergies are not stationary in time. Observations of phenomena induced by mutual TLS interactions such as TLS spectral diffusion [98] and TLS-TLS avoided crossings are reported recently [99]. Specifically, high-frequency TLSs (coherent TLSs or cTLSs) are near-resonant to the resonator resulting in dissipation. A bath of thermally activated low-frequency (LF) TLSs leads to fluctuations of cTLS energies and consequently alters the observed $Q_i$ value and resonant frequency in the time domain. Figure 2.14 illustrates a red cTLS interacts with a bunch of yellow thermal TLSs and the quantum systems. The cTLS energy is jittering at a rate $\gamma$. The fluctuations of the TLS energy in the time domain have an important consequence on the TLS loss. When the TLS energy shifts away from the resonator frequency, then it cannot absorb microwave photons from the resonator. In this case, Faoro shows that the power dependence of the TLS loss tangent is weak and becomes logarithmic [85]. In the condition that $\gamma > \Omega \gg \Gamma_2$, the logarithmic power

dependence loss tangent is formally given as

$$\tan\delta_{tls} = \tan\delta^{0}_{tls}\, P_{\gamma}\, \tanh(\frac{\hbar\omega}{2k_BT})\, \ln(\frac{\gamma_{max}}{\Omega} + C_1), . \tag{2.85}$$

Here, the TLS jitter rate ratio $P_{\gamma} = 1/\ln(\gamma_{max}/\gamma_{min})$, $\gamma_{max}$ and $\gamma_{min}$ are the maximum and minimum rate of TLS jitter respectively, and $C_1$ is a constant accounting for power-insensitive loss.

In a different region that $\gamma \cdot \Gamma_2 > \Omega^2$, one can obtain

$$\tan\delta_{tls} = \tan\delta^{0}_{tls}\, P_{\gamma}\, \tanh(\frac{\hbar\omega}{2k_BT})\, \ln(\frac{\gamma_{max}\Gamma_2}{\Omega^2} + C_1). \tag{2.86}$$

### 2.3.2 Multiple contributions from different material interfaces

In typical planar resonator designs, the loss from TLSs (located in bulk or at the metal-air, substrate-air, and metal-substrate interfaces) contribute differently to the total loss tangent $1/Q_i$ [87]. This yields an equation considering the filling factor for analyzing different material volumes with TLSs [38]:

$$\frac{1}{Q_i} = \tanh\left(\frac{\hbar\omega}{2k_BT}\right) \sum_i F_{r,i} \frac{\tan\delta^{0}_{i}}{\sqrt{1 + \frac{n_{ph}}{n_{c,i}}}}. \tag{2.87}$$

In volume $V_i$, the TLS loss properties ($p$, $E_{zpf}$, and $\Gamma_{1,2}$) are assumed to be the same. Another expression in Ref. [90], on the other hand, uses an integration but the concept is similar to Eq. 2.87 and we obtain

$$\frac{1}{Q_i} = \frac{\int \varepsilon(\mathbf{r})\, |E_0(\mathbf{r})|^2\, \tan\delta_{tls}(\mathbf{r})\, d\mathbf{r}^3}{\int \varepsilon(\mathbf{r})\, |E_0(\mathbf{r})|^2\, d\mathbf{r}^3}. \tag{2.88}$$

In the rest of this thesis, I will call Faoro's model a fast-switching (FS) TLS model, and call the model including different $n_c$ as a multi-contribution (MC) model. To our knowledge, there is no systematic study to verify which explanation is more convincing. In Chapter 6, we show the evidence that only the fast-switching TLS model is consistent with our data but not the MC model. Moreover, the absence of such a logarithmic power dependent loss in the alumina samples even with the observed TLS energy jitter is inspiring and more detail will be discussed in Chapter 5.

# Chapter 3: Experimental Setup and Fabrication Tools

In this chapter, I will provide detailed information about the experimental methods used within this thesis. The chapter starts with a brief introduction about performing measurements at a millikelvin environment. I specify the microwave setup for measuring the resonator's response of the aluminum oxide samples. Next, I will introduce fabrication tools and steps for resonators. This chapter also contains the specific DC voltage bias line setup that are of importance for the observation of individual TLSs.

## 3.1 Cryogenic setup

### 3.1.1 Dilution refrigerator

Superconducting quantum devices require a low temperature much lower than their superconducting transition temperature to suppress the quasiparticles and take advantage of low resistance. Another benefit of low temperature is suppressing thermal noise and thermal excitations in a quantum state [100]. For example, an common transition energy is equivalent to 250 mK ($\sim \frac{h \cdot 5GHz}{k_B}$) and the thermal population $\tanh\left(\frac{\hbar\omega}{2k_BT}\right)$ is very low at 10 mK. In this thesis, all the samples are measured in the CF-650 cryogen-free dilution refrigerator (DR), manufactured by Leiden Cryogenics BV, and the working temperature is at tens of mK. The image of DR, the

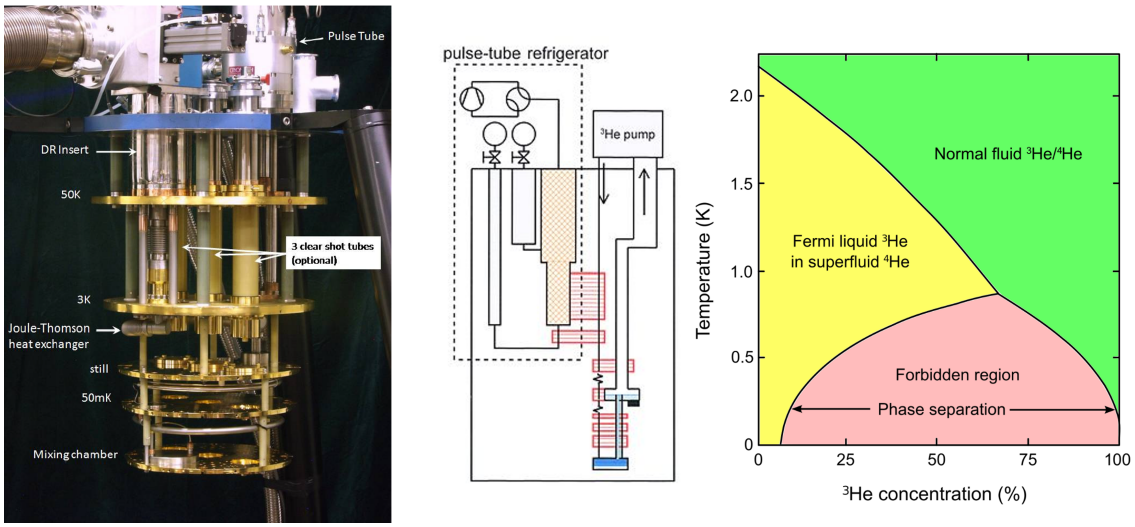


Figure 3.1: Left: Photo of our 3He/4He dilution refrigerator (DR). Middle: Schematic drawing of a DR. The dilution unit is placed inside a vacuum can and a 3He circulation is done by a scroll pump and turbo pumps. The devices are placed on the mixing chamber platform at the bottom of the cryostat. Right: 3He/4He phase diagram.

schematic, and the Helium phase diagram are shown in Fig. 3.1. The working principle of DR is explained below.

Cryogenic temperatures are reached by continuously circulating a mixture of 3He and 4He isotopes [101]. Below 0.867 K, 3He/4He mixtures separate into two phases. One phase is rich in 3He (the concentrated phase), and the other phase is rich in 4He (the dilute phase). The cooling power of the dilution refrigerator comes from the latent heat required when 3He atoms are transferred from the 3He rich side to the 3He poor side. By pumping with a turbo on the "still" chamber which has a 4He-rich phase at about 0.7 K, 3He is mostly removed because the vapor pressure of 3He is much larger than that of 4He. The difference in 3He concentration between the still and the mixing chamber reduces the 3He concentration in the dilute phase in the mixing chamber. In the mixing chamber, in order to maintain the lowest 6.6 % 3He concentration of the dilute phase, 3He crosses the phase boundary from the concentrated phase to the dilute phase. This process contains to absorb latent heat of 3He evaporation into 4He. The latent heat is

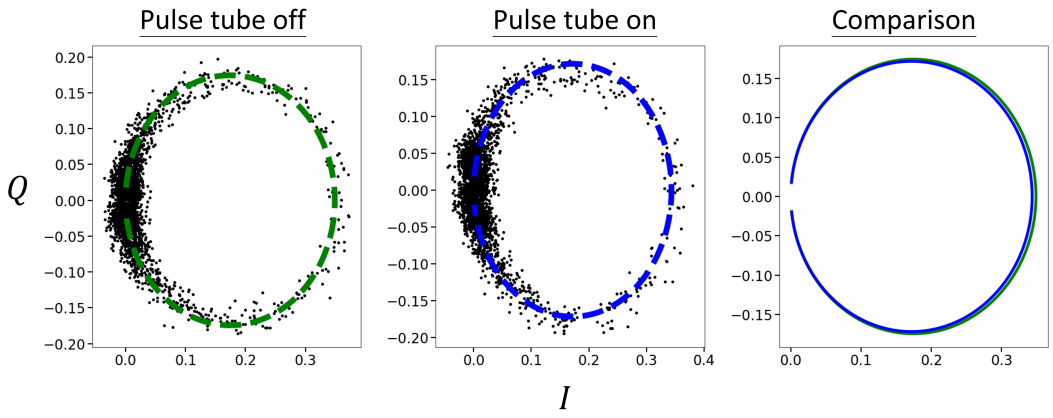


Figure 3.2: IQ plot of the resonator transmission measurement when the pulse tube is off (left panel) and is on (middle panel) along with loose cable connections. Two fitting dashed lines of Eq. 2.15 are plotted and compared in the right panel. We find that the mechanical noise from the pulse tube slightly reduces the internal quality factor $Q_i$. Note that if there is no loose connection, $Q_i$ would be unchanged whether pulse tube is working or not.

provided from the mixing chamber and results in the cooling of the mixing chamber.

A pulse tube cryo-cooler is used for initiating cool-down and keeps the inner vacuum can at $<$ 4K, and the cryostat is considered as "dry". However, this additional cryocooler creates some vibrations which might cause inaccuracy of $Q_i$. The mechanical noise is enhanced and obvious shot noises are seen in the time domain of $S_{21}$ measurement when cable connections are loose. In Fig. 3.2, $S_{21}$ traces of a resonator with loose cable connections are measured when the pulse tube is turned off or on. The green and blue dashed lines are the fits and the extracted $Q_i \approx$ 12k and 11k, respectively. The comparison of the fits is shown in the right panel where the green circle is slightly larger, which means a higher/better $Q_i$. It is worth checking the cables before cooldowns to prevent the pulse tube noise.

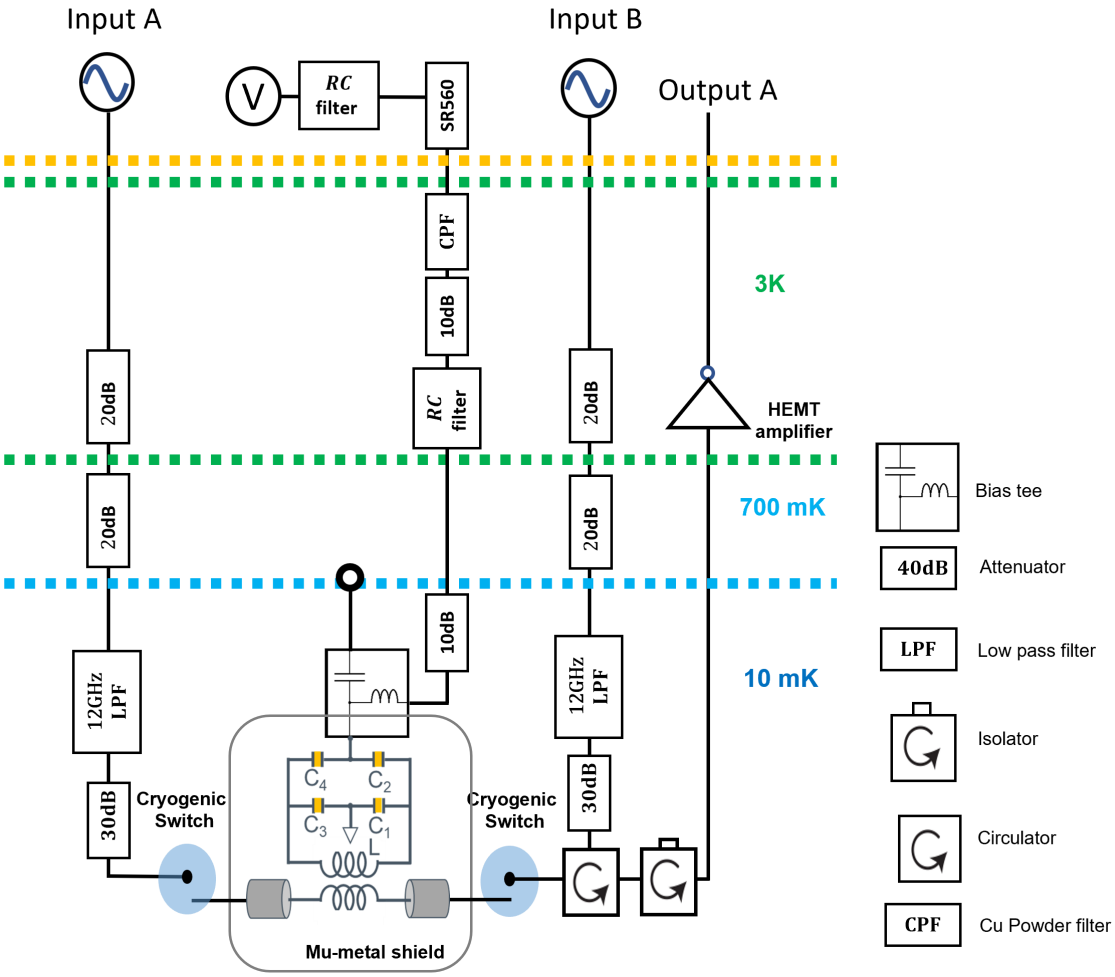


Figure 3.3: A schematic drawing of the electronic setup used in this thesis. Two microwave input lines, labeled "A" and "B", have the same microwave components and are measuring transmission and reflection rates, respectively. Attenuators at different temperature stages stop the thermal radiation from the environment. Two circulators after the cryogenic switch prevent the back-action of the amplifier noise.

### 3.1.2 Microwave measurement setup

A schematic of our microwave components in the DR is shown in Fig. 3.3. A network analyzer (Agilent N5242A PNA) generates a microwave signal from port 1 and measures the return signal in port 2. We choose either semi-rigid or rigid coaxial cables to carry RF signals, which have a small attenuation per meter. The cables in the cryostat are thermally anchored to the plates to allow the center conductor of the cable to be cooled. RF signal is attenuated strongly before the device under test (DUT) by several attenuators (Midwest Microwave model ATT-0298-10-HEX-02) on each plate. The cold attenuator is equally reducing the thermal and signal noise while adding thermal noise of its own temperature. One of the main thermal noises is Johnson–Nyquist noise and the mean squared noise voltage from a resistor $R$ at temperature $T$ in a bandwidth $\Delta f$ is

$$\langle v_N^2 \rangle = 4 k_B T \Delta f. \tag{3.1}$$

For ideal components, the resulting noise temperature $T_n$ seen by the DUT is

$$T_n = 10\,\mathrm{mK} + 700\,\mathrm{mK} \cdot A_1 + 3\,\mathrm{K} \cdot A_1 A_2 + 300\,\mathrm{K} \cdot A_1 A_2 A_3, \tag{3.2}$$

where $A_1$, $A_2$, and $A_3$ are the attenuation factors at the mixing chamber, the still plate and 3K plate, respectively. We choose $A_1 = -30$ dB, $A_2 = -20$ dB, and $A_3 = -20$ dB (see Fig. 3.3) and $T_n = 10.7$ mK is slightly larger than the base temperature = 10 mK. However, in reality, the thermalization of the electrical components is never perfect and the components have a higher temperature than their anchored stage's.

We install solenoid microwave switches (modified from Radiall R573423600 for reducing

the switching heat) at the input and output sides of the DUT and can perform an *in situ* through-transmission calibration [102]. Switches also allow us to connect up to six different samples without needing to warm up the DR. The switching-current-induced heat can be taken away in less than 15 min. From the DUT's output and before the network analyzer, there are two circulators to prevent the microwave from higher temperature stages and the noise from the amplifiers flow backwardly. A high-electron-mobility transistor (HEMT) low-noise amplifier (LNA: CIT-4254-077) on the 3 K plate follows after the circulators. This LNA has a very low noise level in the range of 4-8 GHz. On the output at room temperature, there is a low-phase-noise Miteq amplifier (AMF-5F-04000800-07-10P-LPN) with a maximum noise figure of 0.7 dB and a minimum gain of 50 dB in the frequency span of 4-8 GHz.

### 3.1.3 Voltage bias line

A low frequency (DC – 100MHz) voltage bias line is used for tuning the individual TLSs. In order to suppress noise in the voltage bias line, we spend efforts on filtering all noise above tens of Hz. We place multiple electronic components including a 100Hz cutoff low pass filter and an SR560 preamplifier at room temperature, and a copper powder filter, attenuators, a handmade RC filter, and a bias tee at cryogenic temperature.

The output of the DC voltage source is filtered by an RC filter with a cut-off below 100Hz and then connected to an SR560 pre-amplifier that has an integrated tunable low-pass filter. SR560 is operated on its internal battery mode to isolate 60Hz noise from the power cable, and I choose only DC voltage can pass. The output voltage of SR560 passes through a series of components thermally anchored on the 3 K plate including a copper powder filter (CPF) which has

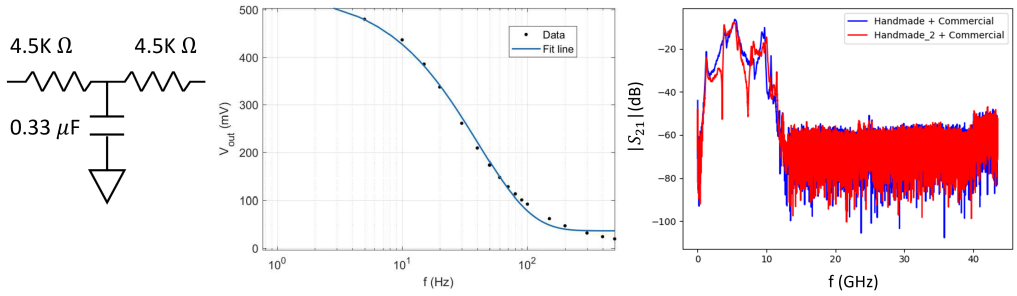


Figure 3.4: Left: The schematic of a handmade RC filter. The symmetric T-shape circuit has two resistors with 4.5 kΩ and a 0.33 $\mu F$ capacitor to the ground. Middle: The voltage response of the handmade RC filter vs frequency. A sine wave with an amplitude of 500 mV is applied from one port and is measured on the other output port. From the fit of an exponential decay function, $V_{out} = A\exp(-f/f_c)$, we find out the cutoff frequency $f_c$ is 40Hz. Right: Transmission rate of the RC filter in series with a commercial 12GHz-cutoff low-pass filter. If the DC line directly connects to the device and is not heavily attenuated, thermal photons from room temperature will affect quantum devices and a low-pass filter is needed. Although the RC filter works well in the low frequency, it cannot filter the frequency range of $>$ few GHz due to the imperfect residual resistance or inductance in the capacitor. In our measurement, there are more other types of filters and components in the DC line for mitigating the voltage noise.

a 10MHz cutoff, a 10 dB attenuator, and a low-pass RC filter with a cutoff frequency of 40Hz. Our handmade RC filter is a T-shape symmetric one-stage RC filter and the schematic and its microwave response are shown in Fig. 3.4. It contains two resistors with 4.5 kΩ and one $0.33$ $\mu$F capacitor to the ground. Although our handmade RC filter has a low cutoff frequency, we find the microwave above 1 GHz cannot be blocked effectively. At high frequency, the residual resistance or inductance in the capacitor dominates which reduces the effect of filtering. A CPF is required for blocking high frequency noise that leaks through the RC filter. On the mixing chamber plate, the DC line is equipped with another 10 dB microwave attenuator. Lastly, before connecting to DUT, the DC line connects to the DC port of a bias tee. With this arrangement, the DC voltage $V_{bias}$ across the capacitor is about 100 times smaller than the DC voltage at the voltage source.

In Ref. [103], we sweep TLSs periodically by a triangle wave up to 20 MHz and filter any frequency above 250 MHz. There is no filtering in the line between the voltage source and DR

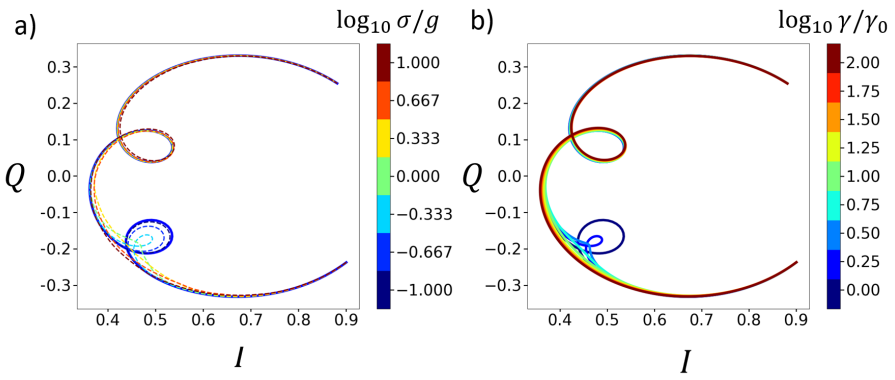


Figure 3.5: Simulation of Eq. 3.5 with two strong-coupled TLSs. Only one of them is affected by voltage noise (lower one). (a) The solid blue line shows a resonator coupled to two TLSs and both have no voltage noise. The colored dashed lines show the enhancement of $\sigma$ from $0.1 \times g$ to $10 \times g$ on the lower TLS. (b) Simulation of the lower TLS under an enhanced decoherence rate. The color lines indicate the behavior of the lower TLS is similar to the enhancement of $\sigma$ in (a).

at room temperature. We do not equip the CPF, the handmade RC filter, and the bias tee but add a 250 MHz low-pass filter (Mini Circuits PLP-250) on the 3K stage. The ratio of DC voltage across the capacitor and from the DC voltage source is 1:10. Moreover, it is worth mentioning, due to the huge impedance of the capacitor on the device at low frequency (as a open end), the oscillating voltage amplitude is two times higher than the value measured by DC voltage. It would affect the fitting result of the dipole moment value by a factor of 2 in the experiments such as Refs. [103, 104]. Moreover, we observe no heating of the fridge from the current during voltage biasing.

### 3.1.4 Individual TLSs under voltage noise

The change of TLS frequency $\delta\omega_{tls}$ due to a voltage noise $\delta V_{ex}$ within a parallel plate capacitor separated by $l_0$ is

$$\delta\omega_{tls} = \frac{\Delta}{\omega_{tls}}\delta\Delta = \frac{\Delta}{\omega_{tls}}\frac{2p\,\delta V_{ex}\,\cos\theta}{l_0}. \tag{3.3}$$

The transmission rate of a resonator coupled to multiple TLSs is [105]

$$S_{21}(\omega) = 1 - \frac{\kappa/2}{\frac{\kappa+\Gamma_r}{2} + i\left(\omega - \omega_0\right) + \sum_i \frac{g_i^2}{\gamma_i/2 + i\left(\omega - \omega_i\right)}}, \tag{3.4}$$

where $\gamma_i$ is the decoherence rate, $\omega_i$ is the frequency of the i-th TLS, and $\kappa$, $\Gamma_r$ and $\omega_0$ are resonator parameters defined in Chap. 2. Inspired by Ref. [106], we assume that every TLS experiences a frequency noise $\delta\omega_i$ having a Gaussian distribution and we rewrite $S_{21}(\omega)$ as

$$S'_{21}(\omega) = 1 - \frac{\kappa}{2} \int \frac{\prod_i \sqrt{\frac{1}{2\pi\sigma_i}} \exp\left(\frac{-\delta\omega_i^2}{2\,\sigma_i}\right) d\delta\omega_i}{\frac{\kappa+\Gamma_r}{2} + i\Delta_c + \sum_i \frac{g_i^2}{\frac{\gamma_i}{2} + i(\Delta_i + \delta\omega_i)}}, \tag{3.5}$$

where $\Delta_c = \omega - \omega_0$ and $\Delta_i = \omega - \omega_i$. The sensitivity of $\omega_i$ to $\delta\omega_i$ is described by the standard deviation $\sigma_i$ of the i-th TLS related to $\delta V_{ex}$ and $p_z$. Next, we show the enhancement of $\sigma_i$ will exterminate the effect of the i-th TLS. A simulation of different $\sigma_i$ is shown in Fig. 3.5 (a), where two TLSs are coupled to the resonator. The upper TLS in the plot is not affected by the voltage noise and the lower TLS in the plot has $g$, $\gamma_0$, and a random frequency shift with deviation, $\sigma$. Simulations show that the lower TLS has a smaller and smaller effect on the resonator while the voltage noise (or $\sigma$) increases. The phenomena of the voltage noise is qualitatively similar to the increasing decoherence $\gamma$ of TLS as shown in Fig. 3.5 (b). Later in Chapter 5.5.7, I will show that the individual TLSs disappear due to the unfiltered bias line.

### 3.1.5 Sample box preparation

We carry our chip in the middle of a PCB patterned with two ports for transmission and 4 ports for low-frequency bias. The image is shown in Fig. 3.6. The chip is held by a small amount

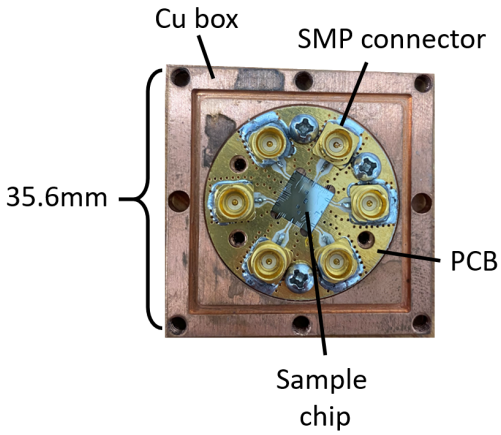


Figure 3.6: Image of a Cu sample box and a printed circuit board (PCB). A total of 6 SMP connectors includes two ports for transmission measurements and four ports for voltage biasing. A sample chip is glued by GE varnish and wire-bonded to the PCB.

of GE Varnish on four sides. The PCB is placed inside a 3.6x3.6x2 $cm^3$ sample box. Sometimes, the importance of the sample box is under looked. Impedance mismatches and parasitic modes lead to losses and spurious reflections especially when the signal wavelength is comparable to the feature size. We cooperate with A.R. Castelli and Y. J. Rosen who used HFSS to simulate the transmission rate of an entire sample box containing the coupler configuration (SMP-PCB connector), a dielectric film, wirebonds, etc. We ensure a close to 50$\Omega$ environment seen by the device. They minimized the impedance mismatch and found $< 0.25$ dB return loss in the crucial 4-8 GHz bandwidth.

## 3.2 Fabrication apparatus

In this section, I briefly describe the tools for fabricating devices in class 10k clean room at the Laboratory of Physical Science building. The processes include deposition, patterning, and etching. The characterization of alumina's structural phases will be described separately in Chapter 5.

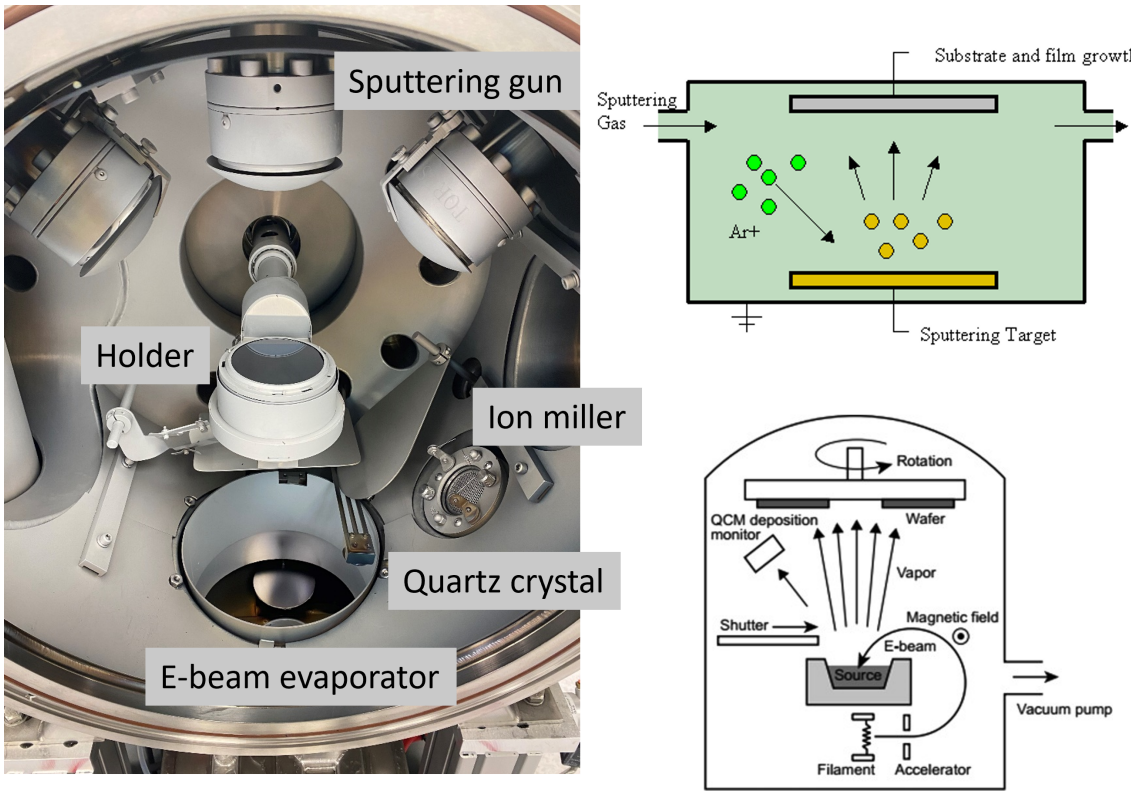


Figure 3.7: Left: Photo of the AXXIS chamber. Three sputtering guns on top and two of them can apply a DC voltage and one of them can apply an RF voltage. Our deposition system also carries an ion miller to remove substrate residues and an e-beam evaporator on the bottom. The substrate holder is in the middle of the chamber. Top right: Diagram of a sputtering process. The Ar ions are attracted to the target material and will dislocate atoms from it. These atoms fly through the chamber and deposit on the wafer. Bottom right: Diagram of an e-beam evaporation. Electrons generated by the filament fly through a magnetic field. Electrons will heat the source and atoms will be evaporated from the melted source.

### 3.2.1 Thin film deposition system

Figure 3.7 shows the Kurt J. Lesker model AXXIS deposition system that I used for depositing aluminum. The processing chamber (PC) is equipped with a cryopump titanium sublimation pump and the pressure can be pumped to $< 10^{-8}$ Torr. The substrate is loaded in the center of the PC and can be rotated to face the sputter targets on the top or the e-beam source on the bottom. The system accommodates two DC-sputtering guns and one RF-sputtering gun. For conductive metals, DC-sputtering guns usually are enough. For non-conductive materials such

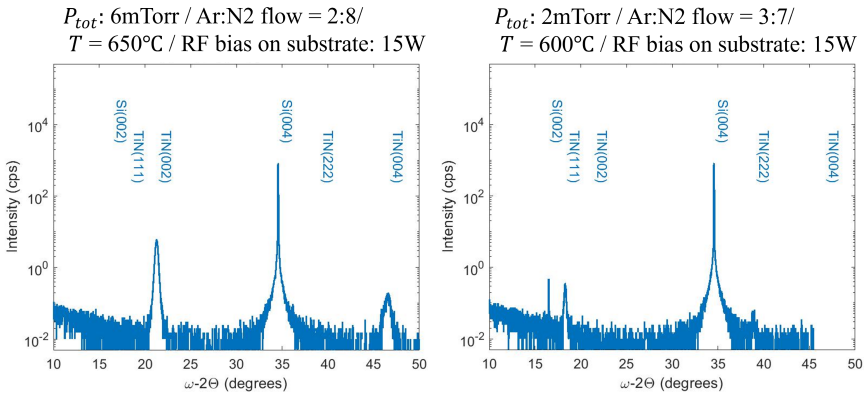


Figure 3.8: An example of reactive sputtering done in AXXIS. X-ray diffraction of titanium nitride (TiN) films deposited by two parameter-sets shows two different dominated peaks. Left: (200) peak $2\Theta = 22°$ is seen in a 100 nm-thick TiN film deposited at a total pressure $P_{tot} =$ 6mTorr, Ar to N2 flow ratio = 2:8, temperature $T = 650°C$ and a RF bias power = 15W. Right: (111) peak $2\Theta = 18°$ is seen in a 100 nm-thick TiN film deposited at $P_{tot} =$ 2mTorr, Ar to N2 flow ratio = 3:7, $T = 600°C$ and a RF bias power = 15W.

as silicon, RF-sputtering guns are needed to discharge the electron accumulating on the surface. A controlled flow of argon flies in the chamber to fill the pressure = 10 mT and a voltage bias is applied to create argon plasma. The argon ions are bombarded into the sputter target, and atoms of the target are ejected and form a thin film on the substrate. The top right panel in Fig. 3.7 shows an illustration of a sputtering chamber.

Additionally, a reactive gas, typically oxygen or nitrogen, can be introduced into the chamber and is ionized as well. The ions react with the ejected atoms forming compounds and this process is called reactive sputtering. The stoichiometry and the structural phase of the deposited film are controlled by many parameters: the total pressure and the partial pressure of the reactive gas in the chamber, temperature, voltage biasing power, etc. Fig. 3.8 shows an on-going project of depositing titanium nitride (TiN) in different crystalline textures. We perform X-ray diffraction measurements on two TIN films and realize the texture depends on the deposition parameters. (200) peak $2\Theta = 22°$ is seen in a 100 nm-thick TiN film deposited at a total presure

$P_{tot} = 6$ mTorr, ratio of Ar to N2 flow = 2:8, temperature $T = 650°$C and a RF bias power on substrate = 15 W. (111) peak $2\Theta = 18°$ is seen in a 100 nm-thick TiN film deposited at $P_{tot}$ = 2 mTorr, ratio of Ar to N2 flow = 3:7, $T = 600°$C and a RF bias power on substrate = 15 W.

AXXIS also has an e-beam evaporator in the bottom of the PC. Unlike sputtering which needs gases to activate the deposition, e-beam evaporations utilize electrons beam to heat up and melt the target material for deposition. Inside the chamber, a tungsten filament biased at a high voltage ($\sim$10 kV) emits electrons to heat up the target material inside the crucible. Once a sufficiently high temperature is reached, the target material melts and evaporates atoms. A quartz crystal is used to monitor the deposition rate of the material and a feedback loop ensures stable deposition conditions by controlling the beam current. The bottom right panel in Fig. 3.7 shows an illustration of an e-beam evaporator. An e-beam evaporated aluminum has a smaller stress than sputtered aluminum, which is necessary for the vacuum-gap resonators, an more detail will be described in Chapter 6 and Appendix A.

#### 3.2.1.1 Photolithography

To transfer geometric patterns onto thin layers of various materials, I rely on optical lithography fabrication technique. A thin layer of photoresist (PR) is spin-coated on the substrate and a pattern is then exposed onto the PR with a certain amount of energy density. For a positive PR, the exposed part of the PR becomes soluble in the developer, and the rest of the substrate is covered by the PR after the development. I perform the patterning using a 5X GCA stepper or a maskless Aligner (MLA150) from Heidelberg instruments. Before spinning a PR, I use isopropanol to clean off the dust and dehydrate the wafer at 90°C for a few minutes. I spin a positive

PR (Fujifilm OiR 906-10) at 3000 rpm, pre-bake it at 90°C for 60 sec, expose a dose of 180J/cm$^2$ and post-bake it at 120°C for 60 sec. The PR is then developed by OPD 4262 developer for 45 sec. An etching process is executed and the PR is then removed by the following procedure: sprayed by acetone, immersed in acetone and sonicated for a few minutes, and rinsed with isopropanol (IPA). Sometimes, a stronger solvent, e.g., N-methyl-2-pyrrolidone (NMP), is needed for a degraded PR caused by the heat from dry etching. Immersing the PR in 80°C for 3 hours can remove most of the residues.

### 3.2.2 Etching

After lithography, the material is chemically and/or physically attacked in areas not covered by a resist mask in an etching process. Etching processes can be divided into two types: dry and wet etching.

Reactive ion etching (RIE) is a form of dry etching that uses plasma to create vertical walls in a material. RIE uses chemically reactive plasma generated by RF power to remove materials. Two ways to create plasma: capacitively coupled plasma (CCP) and inductively coupled plasma (ICP). I use both types for different purposes. The gases typically used in our CCP reactor (Plasmatherm 790) are fluorine-based ($CF_4$, $SF_6$, $CHF_3$, etc). The ions in the plasma are attracted to the negative potential where the substrate is. I use 790 to create the vias. However, dry etching by CCP is mostly anisotropic. On the other hand, ICP is generated by an RF powered magnetic field and a substrate voltage bias can control the etch profiles to be more isotropic. I use our ICP reactor (Oxford PlasmaPro100) to etch SiNx sacrificial layers (SLs) isotropically (see also Appendix A). ICP of chlorine-based gases, i.e., $Cl_2$ and $BCl_3$, can be used to etch Al. However,

we find wet etched Al-resonators have a better resonator quality due to the residues generated after an unoptimized ICP etching process that has a high etch rate.

Ion milling is another kind of dry etching and usually performed before a metal deposition. An ion miller with a voltage of 300 V inside the chamber of AXXIS allows Ar ions to physically etch away the residues. Since ion milling generates heat, an iteration of turning on the shutter for 20 sec and turning off the shutter for 60 sec allows heat diffusion from the substrate, which is especially important in vacuum-gap resonators. If no off time, the PR (served as SLs) will be degraded.

Wet etching is a form of chemical etching where the material is immersed in a solution containing a liquid etchant. Liquid etchants usually have a high selectivity to the target material over others but etch isotropically. I perform two wet etching processes, pre-deposition substrate clean and aluminum wet etching. Pre-deposition substrate treatments optimize the deposited film's adhesion and eliminate TLSs. For silicon substrates, unwanted silicon oxide naturally grows on the silicon surface and should be removed prior to any processing for enhancing $Q_i$. This can be achieved using a solution of diluted hydrofluoric acid (generally 1% or 2%) or buffered oxide etch (BOE). HF cleaning removes the $\mathrm{SiO_2}$ and covers the surface with hydrogen (preventing oxide re-growth). Since the native oxide will still regrow eventually, we load the cleaned wafer in a vacuum as fast as possible. For sapphire substrates, I dip the wafer in a Piranha solution, a mixture of sulfuric acid, and hydrogen peroxide in a ratio of 3:1, at 50°C for 5 min. The solution removes amounts of organic residues which are the source of TLS loss as well.

### 3.2.3 Plasma-enhanced chemical vapor deposition

I deposit SiNx films using plasma-enhanced chemical vapor deposition (PECVD) in an Oxford Plasmalab System 100. In my devices, SiNx is served as an insulator supporting superconducting bridge cross-overs or as a SL for vacuum gap capacitors. Recipes with different flow ratios of $SiH_4$ to $N_2$ and temperature had been investigated in detail by Paik et al. in Ref. [107] and Bahman's thesis [105]. I choose the recipe which provides the lowest loss tangent ($< 10^{-4}$) and small film stress.

### 3.2.4 Dicing and packaging

After completing the fabrication process and before dicing, a thick PR (Fujifilm OiR 908-35) is spun at 3000 rpm for 1 min and baked for 2 min at 120°C. The blades to cut silicon are different than the blades for cutting sapphire. To cut silicon, I use Disco ZH05 SD2000-N1-50-HEEE2028S blades. To cut sapphire, I use Disco DVCA0186 VT07-SD400-VC100-75. After the wafer is diced into a size of 6.35X6.35 $mm^2$, individual chips can be extracted. The PR layer of a chip is removed with the standard organic removal procedure mentioned above. I attach each chip to a sample box using a GE low-temperature varnish. After letting the varnish dry for at least 2 hours, I wirebond the CPW launchers on the chip to the PCB.

# Chapter 4: Optical-Lithography-Made 3D Transmon

Superconducting quantum circuits based on Josephson junctions (JJs), which introduce the required nonlinearity, are a leading candidate for quantum computers and simulators [22, 23, 35, 36, 52]. The tunnel barrier in such junctions was typically formed by a thin amorphous aluminum oxide layer (a-$AlO_x$) sandwiched by two metallic electrodes. One common qubit type is transmon qubits consisting of a JJ in parallel with a coplanar shunted capacitor to form anharmonic oscillators [35]. A large shunted capacitor $\sim$ 100 fF exponentially suppresses the charge noise with a trade-off of low (but enough) anharmonicity.

Traditionally, JJs are defined by an electron-beam lithography method in order to pattern a small junction area, typically a few hundred nanometers wide. Double-angle evaporations, such as Dolan bridge [108] or Manhattan style [109], are commonly used to make overlapping structures, which require undercut or free-standing structures. A bilayer resist of a top thin layer and a bottom thick layer is spun. The bottom PR layer is more sensitive to electrons than the top PR, which results in a natural undercut of $\sim$100 nm after development. Between two evaporations, one would oxidize Al under a certain pressure and a certain period to control the supercurrent of the junction. For Dolan bridges, the free-standing bridges cause shadows and two Al evaporations under two angles would create an overlapping area. On the other hand, Manhattan style techniques have the absence of bridges which increases the mechanical robustness of the resist

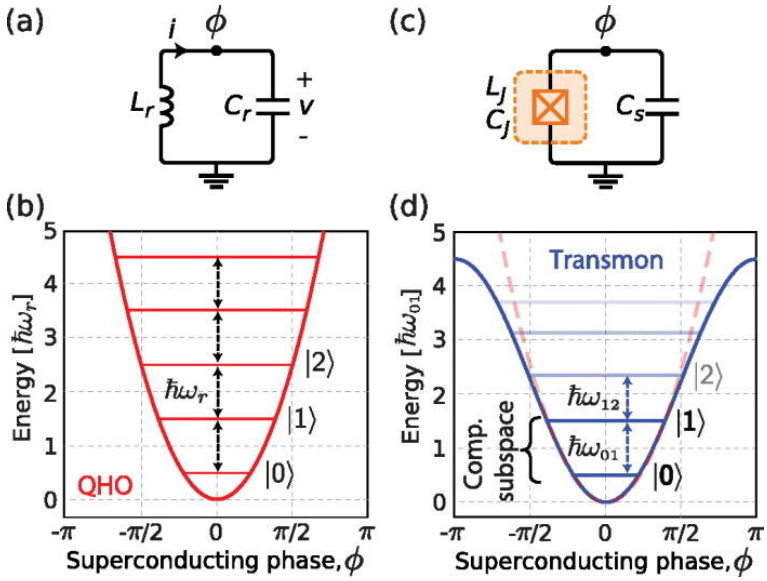


Figure 4.1: Comparison between a harmonic LC oscillator (a,b) and an anharmonic oscillator (c,d). The anharmonicity is from a Josephson junction replacing the inductor in the LC circuit. In the anharmonic oscillator, the energy spacing between each level is different, which allows for the confinement of the computational subspace to the lowest two energy levels. Figure is taken from Ref. [6]

mask and improves productivity. Although the well-developed fabrication process, using e-beam lithography has a huge drawback that it cannot have a massive and fast production compared to a CMOS fabrication using optical lithography. There are questions if optical-lithography-made qubits can perform as well as qubits made by an e-beam method.

In this chapter, I will present the transmon qubits fabricated solely from a optical lithography process and the publication can be found in Ref. [8] with more details. First, I will introduce the background of transmon qubits and provide the detailed fabrication process. Lastly, I will show the microwave setup and qubit measurement results.

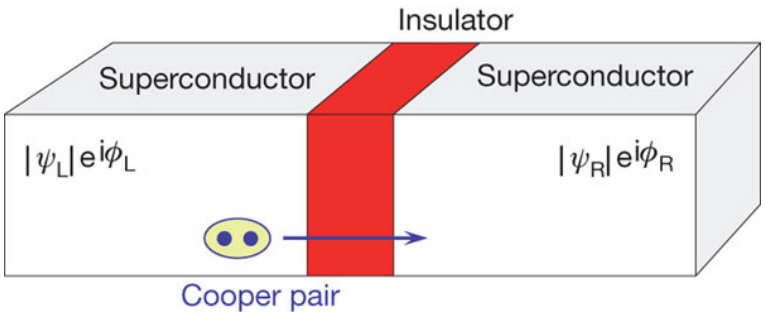


Figure 4.2: A Josephson junction and a junction phase $\phi = \phi_R - \phi_L$. A voltage can be applied on two superconductors resulting an oscillation in $\phi$. Credit to Ref. [7]

## 4.1 Transmon Background

Harmonic oscillators comprised of linear L and C components have equally spaced energy levels which are not easy to define $|0\rangle$ and $|1\rangle$ state (see Fig. 4.1 (a)). However, Josephson junctions provide the nonlinearity based on the tunneling of Cooper pairs [63]. The tunnel current across the junction depends on the relative superconducting phase $\phi = \phi_L - \phi_R$ of the two electrodes (see Fig. 4.2). When a voltage $V$ is applied across the junction, $\phi$ evolves according to $\frac{\partial \phi}{\partial t} = \frac{2\pi}{\Phi_0} V$, where the magnetic flux quantum $\Phi_0 = \frac{h}{2e}$.

According to the first Josephson relation, the tunneling current depends on $\phi : I = I_c \sin\phi$, where the critical current $I_c$ is the maximal supercurrent the junction can sustain. We can derive the below equation of the time derivative of the current from the chain rule:

$$\frac{\partial I}{\partial t} = \frac{\partial I}{\partial \phi}\frac{\partial \phi}{\partial t} = I_c \cos\phi \cdot \frac{2\pi}{\Phi_0} V \tag{4.1}$$

Rearranging the equation in the form of current-voltage characteristic of an inductor,

$$V = L(\phi)\frac{\partial I}{\partial t} = \frac{\Phi_0}{2\pi I_c \cos\phi}\frac{\partial I}{\partial t}. \tag{4.2}$$

A JJ acts as a nonlinear inductor and the inductance

$$L(\phi) = \frac{\Phi_0}{2\pi I_c \cos\phi}. \tag{4.3}$$

The energy stores in the junction is the integral of the power over time and

$$\Delta E = \int_1^2 IV dt = \int_1^2 I_c \sin\phi \frac{\Phi_0}{2\pi} d\phi = \frac{\Phi_0 I_c}{2\pi} \cos\phi \Big|_1^2 = E_J \cos\phi, \tag{4.4}$$

where $E_J = \frac{\Phi_0 I_c}{2\pi}$ is the Josephson energy. Besides the nonlinear inductor, the two electrodes separated by a dielectric themselves are an intrinsic capacitor $C_J$. A Josephson junction, therefore, can be considered as a qubit but with a low coherent time [110] and the Hamiltonian

$$\mathcal{H} = 4E_C \left(\hat{n} - n_g\right)^2 + E_J \cos\hat{\phi}, \tag{4.5}$$

where $E_C = \frac{e^2}{2C_J}$ is the charging energy, $\hat{n}$ is the charge operator in the number of Cooper pairs, $\hat{\phi}$ is the phase operator and $n_g$ is the offset gate charge number. We can also map the capacitor part of the energy to the Hamiltonian of a LC circuit equation (Eq. 1.28 in Chapter 1) by replacing the charge operator $\hat{Q} = 2e\hat{n}$.

Koch *et al.* show that transmons, containing a capacitor $C_s \gg C_J$ parallel to the junction, can exponentially suppress charge noise $\delta n_g$ by engineering a large ratio $\frac{E_J}{E_C} \geq 50$ [35]. A new charging energy $E_c = \frac{e^2}{2C_\Sigma}$ (see Fig. 4.1 (c) and (d)), where the total capacitance $C_\Sigma = C_J + C_s$. In this condition, we are able to transfer the charge and phase operators to a regular creation and

annihilation operators, $b$ and $b^\dagger$, and get

$$\hat{n} \;=\; -i\left(\frac{E_J}{8E_C}\right)^{\frac{1}{4}}\frac{(b-b^\dagger)}{\sqrt{2}} \tag{4.6}$$

and

$$\hat{\phi} = -i\left(\frac{8E_c}{E_J}\right)^{\frac{1}{4}}\frac{\left(b+b^\dagger\right)}{\sqrt{2}}. \tag{4.7}$$

We result in a Duffing oscillator type of Hamiltonian

$$\mathcal{H} = \sqrt{8E_CE_J}\left(b^\dagger b+\frac{1}{2}\right) - E_J - \frac{E_C}{12}\left(b+b^\dagger\right)^4 \tag{4.8}$$

and the corresponding m-th energy level is

$$E_m \cong\; -E_J + 8\sqrt{E_JE_C}\left(m+\frac{1}{2}\right) - \frac{E_C}{12}(6m^2+6m+3). \tag{4.9}$$

The magic in transmon is that the charge dispersion in $|0\rangle \rightarrow |1\rangle$ transition

$$\frac{\partial E_{01}}{\partial n_g} \propto E_c\left(\frac{E_J}{2E_C}\right)^{\frac{5}{4}} e^{-\sqrt{\frac{8E_J}{E_C}}} \tag{4.10}$$

by the fluctuation of the offset charge $n_g$ is decreased exponentially with $\frac{E_J}{E_C}$. However, the trade-off would be the reduction of the anharmonicity $\alpha = E_{12} - E_{10} \approx -E_c$.

In qubit design, we can estimate $E_J$ from the Ambegaokar-Baratoff formula [111] before a qubit measurement in cryogenic temperature. For tunnel junctions at T = 0 K, the relationship between the normal junction resistance $R_n$ measured at room temperature and aluminum super-

conducting gap $\Delta_{sc}$ is $I_c R_n = \frac{\pi \Delta_{sc}}{2e}$. With $\Delta_{sc}$ = 162 $\mu$eV and the finite-element simulation value of the shunted capacitance, one can predict the qubit frequency by

$$\omega_q = \sqrt{\frac{\pi \Delta_{sc}}{\hbar R_n C_\Sigma}} \tag{4.11}$$

.

### 4.1.1 Transmon-cavity couplings and qubit measurements

Since qubits are vulnerable to the environment, we are protecting qubits by placing a resonator in between qubits and the transmission line. The total Hamiltonian is a combination of the qubit Hamiltonian $\mathcal{H}_q = 4E_c \left(\hat{n} - n_g\right)^2 - E_J \cos\left(\hat{\phi}\right)$, the cavity $\mathcal{H}_{cav} = \hbar\omega_c(a^\dagger + a)$, and the qubit-cavity interaction $\mathcal{H}_{int} = \hat{q} \times \hat{V} = 2\,e\,\hat{n} \times \hat{V}$, where $\hat{V}$ is the voltage operator of resonator. Classically, voltage is the charge Q divided by capacitance C. In an operator form, we could write $\hat{V} = \frac{\hat{Q}}{C}$ and $\hat{Q} = -i\sqrt{\frac{\hbar}{2Z}}\left(a^\dagger - a\right)$ such that $\hat{V} = -i\sqrt{\frac{\hbar\omega}{2C}}(a^\dagger - a)$. However, only a portion of voltage from the resonators would act on a qubit and the actual voltage across the qubit is $\beta\hat{V}$, where $\beta$ is the coupling capacitance ratio [35]. Finally, a total Hamiltonian of a superconducting qubit and a resonator

$$\mathcal{H}_{tot} = 4E_c \left(\hat{n} - n_g\right)^2 - E_J \cos\left(\hat{\phi}\right) + \hbar\omega_c a^\dagger a + 2\,i\,e\beta\sqrt{\frac{\hbar\omega}{2C}}\left(a^\dagger - a\right)\hat{n}. \tag{4.12}$$

Simplifying the qubit Hamiltonian having only the ground and the first excited state, I obtain

$$\mathcal{H}_{tot} = \frac{\hbar\omega_{01}}{2}\sigma_z + \hbar\omega_c a^\dagger a + \hbar g_{01}(\sigma_+ - \sigma_-)(a^\dagger - a), \tag{4.13}$$

where $\omega_{01} = (E_1 - E_0)/\hbar$ and the coupling strength

$$\hbar g_{01} = 2\beta e \sqrt{\frac{\hbar\omega}{2C}} \langle 0| \hat{n} |1\rangle = e\beta \sqrt{\frac{\hbar\omega}{C}} \left(\frac{E_J}{8E_C}\right)^{1/4}. \tag{4.14}$$

A common choice of $g \sim 2\pi\cdot$100 MHz and detune $\Delta_{qc} = \omega_q - \omega_c \sim$ GHz makes the qubit-cavity system in a dispersive regime with the dispersive shift $\pm\chi = \frac{g^2}{\Delta_{qc}}$ given in Eq. 1.35. As long as $\chi$ is larger than the linewidth of the cavity $\kappa + \gamma \approx \kappa < 2\chi$, one can easily distinguish $|0\rangle$ from $|1\rangle$ state. More importantly, the measurement is QND if we choose the measurement operator $\hat{M} = a^\dagger a$, which commutes with $\mathcal{H}_{tot}$.

However, the transmon is not a pure two-level qubit but rather an anharmonic oscillator [35]. The Hamiltonian is

$$\mathcal{H}_{tot} = \hbar \sum_i \omega_i |i\rangle \langle i| + \hbar\omega_c a^+ a + \hbar \sum_n g_{n-1,n} \langle n-1|n\rangle \left(a^+ + a\right), \tag{4.15}$$

where $\hbar\omega_i$ denotes the transmon energy levels, and the coupling strength $g_{n-1,n} = g_{01}\sqrt{n}$ assuming no two-photon transition.

$\mathcal{H}_{tot}$ can be approximated into a Jaynes-Cummings style Hamiltonian $\mathcal{H}_{JC}$ by diagonalizing and then truncating into the lowest two levels ($|0\rangle$ and $|1\rangle$) and

$$\mathcal{H}_{JC} = \hbar\widetilde{\omega}_c\, a^\dagger a + \frac{1}{2}\widetilde{\omega}_{10}\sigma_z + \hbar\chi' a^\dagger a \sigma_z, \tag{4.16}$$

where a new dispersive shift $\chi' = \frac{g_{01}^2\alpha}{\Delta(\Delta-\alpha)}$, a new cavity frequency $\widetilde{\omega}_c = \omega_c - \frac{g_{01}^2}{\Delta_{qc}-\alpha}$ and a new qubit frequency $\widetilde{\omega}_{10} = \omega_{10} + \frac{g_{01}^2}{\Delta_{qc}}$. $\chi'$ is now a function of anharmonicity such that the larger the capacitor is, the smaller the $\chi'$ is. A moderate choice of the shunted capacitor is important to

assure $\alpha$ is larger enough and also $2\chi' > \kappa$.

### 4.1.2 Importance of JJ resistance variance

Crosstalks are identified as a dominant source for gate error and can be described as an unwanted interaction between coupled qubits [112, 113]. For superconducting qubits, the crosstalk depends on the detuning between two qubits. A good qubit frequency targeting, the process of reducing the mismatch between the designed and the measured qubit frequency during fabrication, allows to minimize the crosstalks. However, the designed qubit frequency is usually unmatched with the measured frequency due to the uncertainty of the $\mathrm{AlO_x}$ thickness. People are aware of the importance of clarifying the material science which governs the formation and stability of thin AlOx films.

There are a few methods used to avoid accidental resonance of qubits, which leads to strong ZZ interactions. The first method is to tune the qubit frequency using a tunable qubit and the second is to temporarily disable connections between qubits using tunable couplers [114]. The problem with using both tunable qubits and tunable couplers is that such an architecture generally is susceptible to flux noise. An alternative approach is IBM Q's works having fixed frequency qubits and fixed couplers but executing a laser-annealing technique [115]. Those fixed quantum elements are immune to the flux noise. However, the downside of this architecture is that the tuning range of qubit frequencies is small and the frequency targeting is still important. There are efforts of improving the qubit frequency variance through optimizing the fabrication process [116] in e-beam lithography. In this Chapter, we use only optical lithography and find the JJ resistance has a comparable variance to that made by e-beam lithography.

## 4.2 Fabrication process

The transmon qubits are fabricated and the room temperature junction properties are measured in SUNY Polytechnic Institute. The full fabrication content can be found in Ref. [8].

### 4.2.1 Motivation and Background

It is believed the same transmons have shorter $T_1$ times fabricated by optical lithography than by e-beam lithography. The main reason is the rough resolution ($\sim$500 nm) using 365 nm i-line or 435 nm g-line in a lab standard machine and the JJ area ends up being in $\mu\mathrm{m}^2$ size. Since the tunneling barrier $\mathrm{AlO_x}$ is a lossy material containing strong coupled TLSs, a small JJ area would be optimal. Furthermore, a large junction area means small $E_J$ and large self-capacitance $E_c$ which makes it harder to reach the transmon region.

Optical lithography, developed in the CMOS industry, is well known to produce nearly identical features over large areas. The narrowest resolvable lithographic line is given by ${}^{\mathrm{k_1}\lambda}/_{\mathrm{NA}}$, indicating the important variables of lithographic wavelength $\lambda$ and numerical aperture NA. A short wavelength and a close to unity numerical factor $\mathrm{k_1}$ are hard to reach in a lab. SUNY Polytechnic fabricated arrays of JJ on 300 mm wafers using an industry-standard 193 nm lithography. Submicron junctions could be realized in a wafer size ($>$ tens of cm) in a short time.

The fabrication process allows us to have a standard deviation of room temperature junction resistance as low as 2.8 - 3.6% across a 300 mm wafer. It is the first-time massive numbers of transmons on the large wafer are fabricated solely by optical lithography. The result is comparable to ebeam-lithography-made junctions in a 150 mm wafer [116].

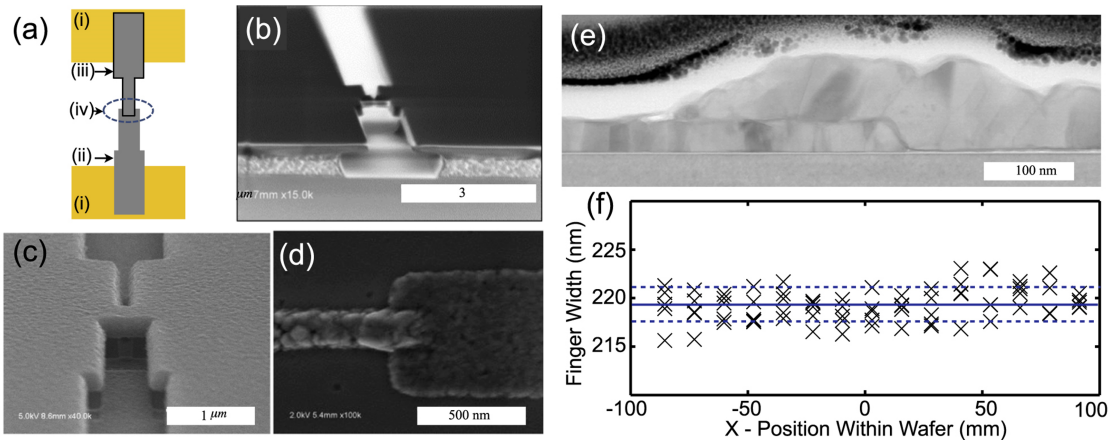


Figure 4.3: Figure is from Ref. [8]. (a) Patterns formed at various stages of the process flow:(i) TiN paddles, (ii and iii) leads and (iv) (in a dashed circle) connected Josephson junction which is formed by two angled evaporations and oxidation near the Dolan bridge. Top Al evaporation finger overlaps an oxidized Al base layer. (b)–(d) SEM images at consecutive stages. (b) Patterned Dolan bridge before evaporations (c) Bridge with JJ (d) JJ after liftoff (bridge removed). (e) Cross-sectional TEM image of angle-evaporated JJ. (f) Inline SEM measurements of finger width in resist, with a fit to mean (solid line) and standard deviations $\sigma$ (dashed line). Finger widths of top Josephson electrode with a standard deviation of 0.78%.

### 4.2.2 Detailed process

A resistivity $>$ 20 k$\Omega$-cm is chosen for small wafers in order to reduce the loss from the substrate. There is a limited choice of high wafer resistivity for 300 mm Si wafers leading to a question of whether high-performance qubits can be realized and we are choosing 10 k$\Omega$-cm for our wafer.

The surface of the wafer is carefully inspected. KLA-Tencor SP3 with a deep ultra-violet laser source found only 10 and 17 particulate defects $>$ 90 nm from two randomly selected wafers as a good starting surface cleanliness of the wafer. The native oxide of Si wafers is removed by a dilute HF. The choice of superconductor is TiN, which was measured to have a long coherence time in the past [117]. 40nm-thick TiN is grown using physical vapor deposition and found to have a (200) texture by X-ray diffraction analysis. The TiN film is then patterned to form the

probe pads in the Josephson junction arrays and the paddles in the qubits.

The bilayer photoresist is as follows. The bottom layer of 530 nm of polydimethylglutarimide-based resist (PMGI SF6 series, from MicroChem) is spun and baked. This is followed by spin-coating (and baking) a 208 nm-thick layer of a commercial 193 nm positive photoresist top layer. The pattern for the junctions is drawn using an ASML TWINSCAN AT:1200B system.

After exposure, the wafer is immediately baked and developed using a 0.26N TMAH-based solution. Through optimization of development time, PMGI SF6 resist is selectively removed to form the Dolan bridge. The undercut is confirmed using tilt-view SEM observations (see Fig. 4.3 (b)). The 300mm wafer is then diced into 5 mm chips and each chip contains one transmon. Each transmon is nominally the same, with a paddle spacing of 40 $\mu$m, paddle width of 250 $\mu$m, paddle length of 500 $\mu$m, for a total transmon length of 1.040 mm.

Starting from a pressure below $5 \times 10^{-7}$ Torr, the wafer is then sputtered with Ar for 4 minutes to clean organic contaminants. Separate tests determine that the sputtering decreases photoresist film thickness but not $SiO_2$ film thickness. After sputter cleaning for $\approx$ 60 s in base pressure, the bottom electrode of the JJ is formed by 0° tilt of 30 nm of aluminum evaporation, at a deposition rate of 0.1 nm/s. The aluminum is subjected to in-situ oxidation with a 20% $O_2$ in Ar mixture flowing at a controlled rate of 800 sccm, with the chamber connected to the only roughing pump. The system pressure under these flow conditions is $\approx$ 0.23 Torr based on measurements during several nominally identical runs and oxidation times fall in the range of 30 to 120 minutes.

After completing oxidation, we pump the chamber down and deposit 60 nm of Al using 55° tilt evaporation. The Al deposition made contact with the underlying TiN paddles. The chips are subjected to lift-off with NMP followed by an IPA rinse and $N_2$ blow-dry. The variance of

the JJ area is beyond the variance of finger width of resist pattern caused by rough evaporated Al features. The cross-sectional TEM image in Fig. 4.3 (d) confirms a thin oxide layer sandwiched by Al layers as a Josephson barrier but also in the interface of Al and Si substrate which would limit the performance of qubits. Figure 4.3 (e) shows a standard deviation of 1.7 nm or 0.78% of the median in the measured finger feature widths across a central 176 mm × 130 mm region of the wafer. We characterize JJs resistance using a voltage sweep from -0.2V to 0.2V. An open, shorted, or nonlinear I-V curve is defined as "bad". The yield of "good" junctions in the arrays is well over 90% for finger widths of 140 nm and greater.

## 4.3 Microwave setup

In qubit controls, fast qubit gates maximize the operation number one can do within the decay time. Fig. 4.4 shows the microwave measurement setup. To generate a pulse, I send a microwave from a frequency generator to the local oscillator (LO) port of an IQ mixer. The output signal from the RF port is generated when the voltage is set on either in-phase (I) or quadrature (Q) port. An arbitrary wave generator (Tektronix AWG 5014c) sends a voltage pulse to the I port with an additional offset voltage on the Q port to minimize signal leakage. We find at least a -40 dB on/off ratio with an optimal voltage offset on the Q port. To further reduce the microwave leakage, especially in readout pulses, we have a mechanical switch after the mixer and turn on the switch 50 ns before the readout pulse.

We read out qubit states in a homodyne measurement set-up. The high-power microwave signal from the Keysight E5072A vector network analyzer at cavity frequency is first split into two paths. The first path transfers the microwave for ringing up cavity's photon number as a

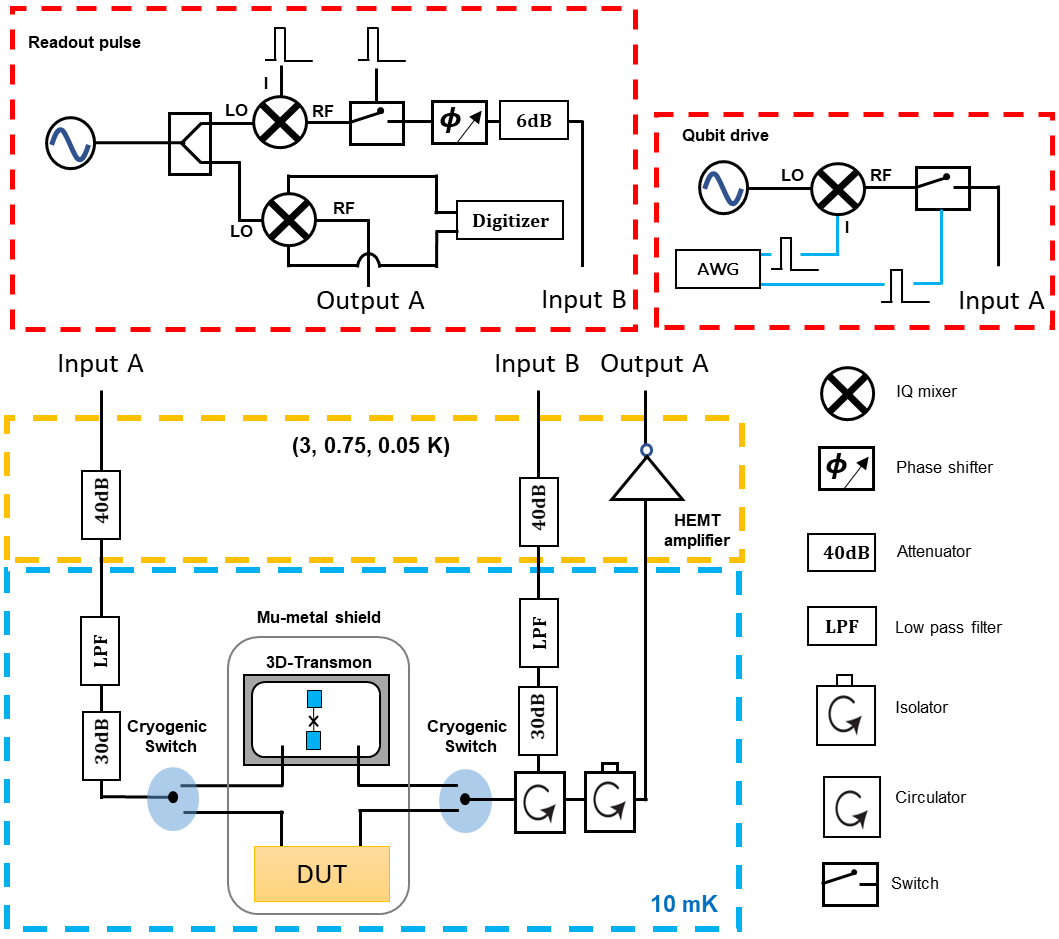


Figure 4.4: Qubit microwave measurement setup. Two input lines, A and B, transfer the microwave pulse for transmission and reflection measurements, respectively. Both input lines have a total 70 dB attenuation and a 12GHz low-pass filter. The 1-to-6 cryogenic switches allow us to measure up to 6 devices in one cooldown. There are two circulators to reduce the reflection noise from the HEMT amplifier. The control/measurement pulses are generated by a series of an IQ mixer and mechanical switches.

detection signal (see Fig. 4.4 orange box). The detection signal passes a IQ mixer and a switch as mentioned above to generate a short pulse ($\sim$3 $\mu$s). It is then phase shifted manually by a phase shifter such that the qubit information only appears in one phase. The detection signal is attenuated in room temperature before going into the DR and is further attenuated by 70 dB in the input line. The heavy attenuation is necessary to minimize thermal photons in the cavity and improve $T_2$ decoherence time [100]. A 12GHz cutoff low-pass filter is placed in the lowest temperature plate to filter thermal radial photons. The reflection signal from the cavity is amplified by a HEMT and a LNA and the output line set-up had been mentioned in Chapter 3.1.2.

The amplified qubit information signal is sent to the RF port of the mixer, which is downward converted by the microwave with the same frequency sent from the second path to the LO port of the mixer. The low frequency signals out from the I and Q port would carry the in-phase and out-of-phase informations of the cavity. We place a 100 MHz cutoff low-pass filter and an amplifier before the signal goes into an Aquiris data acquisition card (DAQ). The DAQ digitized the 10 MHz IF bandwidth filtered signal at 1 GSa/s or with a resolution of 1 ns.

## 4.4 Millikelvin Characterization

### 4.4.1 Qubit state readout

The readout scheme is following the "punch-out" high fidelity technique proposed in Ref. [55]. Cavity modes would inherit some nonlinearity because of hybridizing with a qubit, and the cavity is not a pure linear element. I show in Fig. 4.5 that when we drive much harder with input power around -40 dBm, we start to see the evidence of the cavity being non-harmonic. The cavity resonance splits into two states and behaves as a Kerr-Duffing oscillator. Further

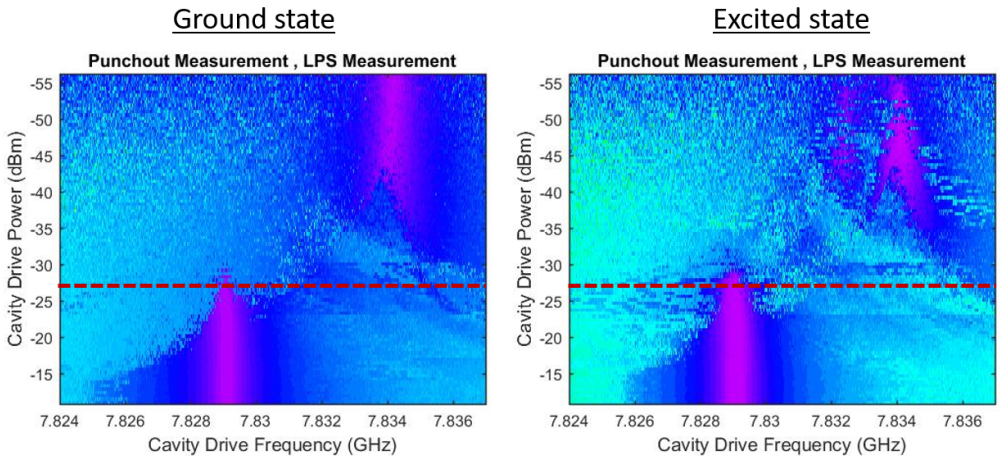


Figure 4.5: Punch-out qubit readout. Left: qubit is in $|0\rangle$. Right: qubit is in the mixed state of $|0\rangle$ and $|1\rangle$ by continuously pumping the qubit at its frequency. While increasing the cavity drive power, we start to notice the cavity resonant frequency shifts to a "bare" cavity frequency ($\approx$7.825 GHz) at high power. We find that it requires more power for panel (a) than panel (b) to switch into the bare resonance. The guideline is showing the readout power.

increasing the power, two peaks would be separated furthermore and the one being pushed down in frequency would dominate eventually around power $\sim$-30 dbm. This behavior indicates that the cavity anharmonicity is removed at a certain point and restores its linear response. The cavity is referred to as being in its bright state. Interestingly, the power of the cavity being in the bright state is slightly different when the qubit is in $|0\rangle$ or $|1\rangle$. The frequency where the cavity goes bright is always the same and we call this frequency the "bare" cavity frequency as if the cavity is in the absence of the qubit's nonlinearity. We use this phenomenon to measure qubit state: a readout tone at the bare cavity frequency with optimized power to distinguish qubit state for the maximal fidelity .

### 4.4.2 Continuous wave measurement

Transmon qubits are placed inside 3D Al cavities (see Fig. 2.5 (c)) and are measured at $\leq$ 20 mK. In our small JJs, most of the capacitance is from the large paddle and the paddle

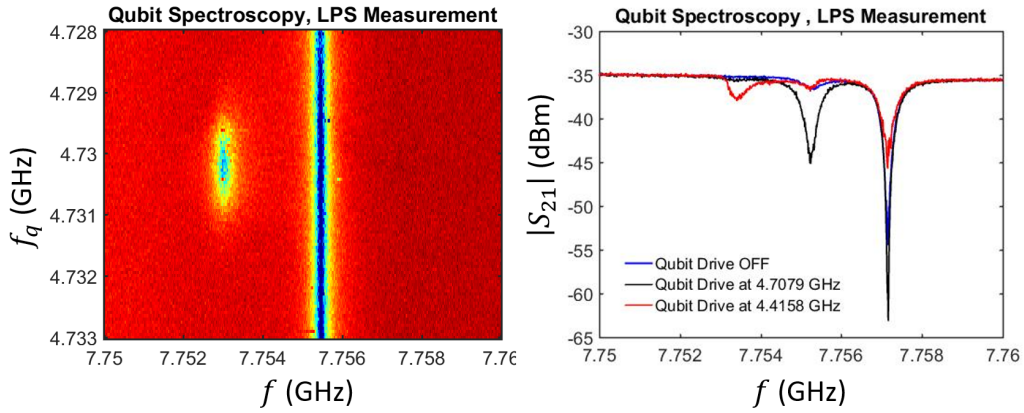


Figure 4.6: Continuous wave measurement $S_{21}$ near cavity resonant frequency $f$. Left: Intensity plot of $|S_{21}(f)|$ vs qubit drive frequency $f_q$. (b) $|S_{21}|$ when qubit drive frequency is around 4.71 and 4.42 GHz to excite $|0\rangle \rightarrow |1\rangle$ and $|1\rangle \rightarrow |2\rangle$ transition, respectively.

capacitance can be simulated in HFSS. Two cavities are over-coupled to the transmission line (external coupling rate $\kappa \approx 2\pi \cdot$ 350kHz $\gg$ internal decay rate) at $\omega_c/2\pi$ = 7.83 GHz and 7.77 GHz, and the qubit frequency is at around 5GHz.

We characterize the frequency of each qubit by a continuous microwave exciting tone scanning around the expected qubit frequencies and a probe tone measuring the transmission rate of the resonator. One example of such measurement is shown in Fig. 4.6 (a). In Fig. 4.6 (b), a distinguishable second dip shifted to the left side indicates that $\chi'/2\pi$ = -0.97 MHz $> 2\kappa$ and the qubit is in the mixed state. We can also determine the second excited state through an exciting tone near $\omega_{12}$, where a third dip would show up in $S_{21}$ (see Fig. 4.6 (b)). The rough qubit frequency is chosen when the second dip has the lowest value. A precise qubit frequency would be later determined by a Ramsey $\mathrm{T}_2$ experiment.

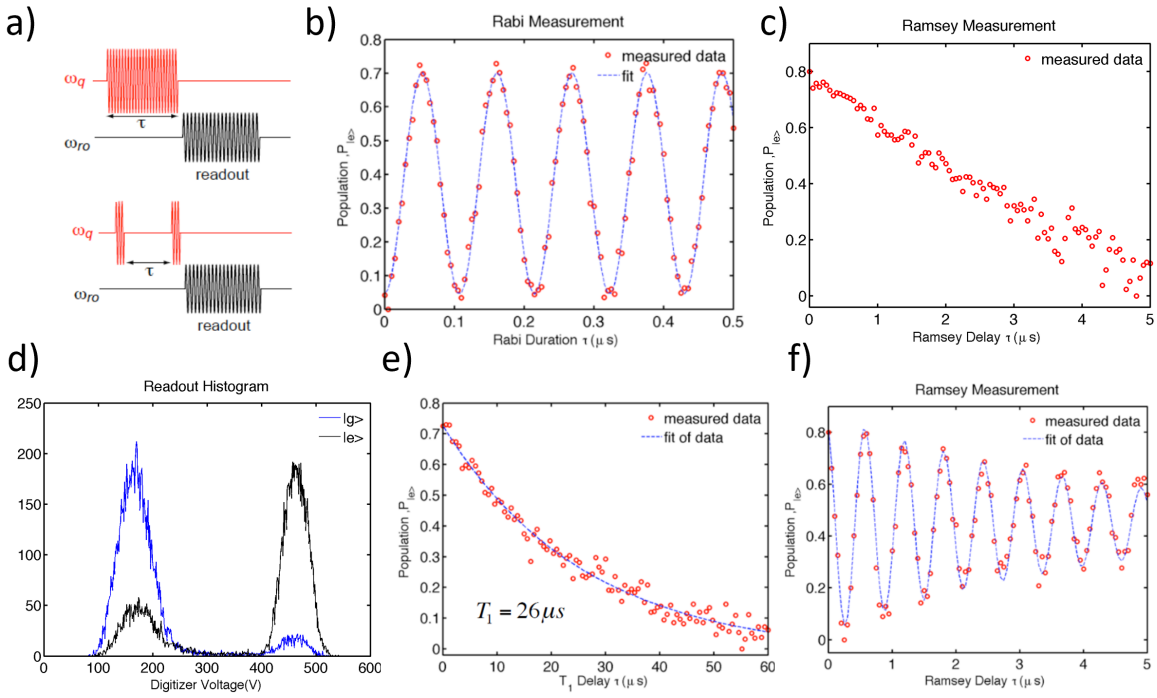


Figure 4.7: (a) Pulse sequences for Rabi and Ramsey measurement on top and bottom, respectively. (b) Rabi measurement to determine the pulse length. (c) Ramsey measurement to determent the qubit frequency and $T_2$. (d) The histogram of single shot measurement. We obtain the measurement fidelity $F_r$ = 1 - $P(e|g) - P(g|e)$ = 66%, where $P(e|g)$ is the probability of qubit initialed in the ground state but being measured as in the excited state.

### 4.4.3 Qubit $T_1$, $T_2$ and frequency determination

We determine the width of qubit pulses by a Rabi measurement as shown in Fig. 4.7 (b), where we apply a various qubit pulse length (see Fig. 4.7 (a)) and a 3 $\mu$s readout pulse is followed immediately after the end of the qubit pulse. The qubit state population is oscillating between the ground and the excited state. We increase the power until a $\pi$ pulse has a length of 50 ns.

We characterize the qubit frequency by a Ramsey measurement in Fig. 4.7 (c), which contains two $\pi$/2 pulses with a varying interval time. We fine tune the qubit pulse frequency until the Ramsey measurement has no oscillation. Ramsey measurements can also determine the $T_2$.

The readout pulse power is optimized after we set a good guess of qubit frequency and a duration of 50 ns. As shown in Fig. 4.7, 92% of single shot readouts show that the qubit is in the ground state when the qubit is prepared in the ground state and 74% of single shot readouts show that the qubit is in the excited state when the qubit is prepared in the excited state. The fidelity is defined as $F_r = 1 - P(e|g) - P(g|e)$ = 1 - 8% - 26% = 66%.

The qubit fidelity is limited by the imperfect $\pi$ pulse, the punch-out readout technique, no qubit-reset scheme, input line radiation, etc. The $\pi$ pulse we choose is a square pulse which contains a spread frequency component including $\omega_{12}$ and slight excites the qubit to $|2\rangle$ states. Better pulse shapes are a Gaussian pulse or a derivative removal via an adiabatic gate (DRAG) pulse [118], which can avoid the second excited state population and further increase the fidelity of readout.

High power readout is a good method in the absence of a quantum-limited parametric amplifier. Because of the high power, the readout pulse itself might switch the qubit state. It is also an issue for the authors with only 87% fidelity [55]. With the help of ultralow noise amplifiers

made by JJs, qubit read-out fidelity can reach above 99% in a shot pulse duration [47, 56].

Finally, we report the measurement of $T_1$ and $T_2$ on both qubits. The $T_1$ = 26 and 23 $\mu$s and $T_2$ is 4.9 and 4.4 $\mu$s and one example of measurement of $T_1$ and $T_2$ is in Fig. 4.7.

## 4.5 Conclusion

Our fabrication utilizes a 300 mm Si wafer with a resistivity of 10 k$\Omega$-cm as the substrate for transmon qubits and $T_1 = 26$ and 23 $\mu$s in two transmons are observed. In this study, we find a method to fabricate high-quality transmons using advanced optical lithography. For the JJ array portion of these chips, the standard deviation in resistance is 2.8 to 3.6%. Two qubits have a difference in $|0\rangle$–$|1\rangle$ transition frequency of 1.33% which is consistent with the JJ statistics on resistance.

# Chapter 5: Bulk Alumina TLSs Spectroscopy

## 5.1 Motivation

Two-level systems (TLSs) are present in the materials of qubits and are considered defects because they limit qubit coherence. Unwanted TLSs are generated not only upon oxygen exposure (metal-oxide) but also during various fabrication steps. For superconducting qubits, the quintessential Josephson junction barrier is made of amorphous alumina, which hosts numerous TLSs [34]. However, the microscopic identity of nanoscale TLSs in amorphous solids is generally unknown – either structurally or in atomic composition. Many different theoretical proposals exist to explain the origins of TLSs and their corresponding dipole moment $p$ [119–123]. Information on TLS dipole moments $p$ is of particular importance since TLSs absorb energies from quantum devices through $p$. Given the additional information obtained from more recent qubit experiments on strongly coupled TLS [99, 124], it is possible that we can compare the experimental results to theoretical models. The coupling depends on the dipole along the axis of the zero-point electric field $E_{zpf}$, which is set as z-direction. From qubit experiments, we are capable of obtaining dipole moment information from the coupling strength

$$\hbar g = \frac{\Delta_0}{E_{tls}} p_z \mathrm{E}_{zpf}, \tag{5.1}$$

where $p_z$ is the dipole moment $p$ projected on the direction of $E_{zpf}$. Here, we assume a uniform JJ barrier thickness $d_J$ (usually = 2 nm), and $E_{zpf} = \sqrt{\frac{\hbar\omega}{2C_\Sigma d^2}}$, where $\omega$ is the qubit frequency, $C_\Sigma$ is the total capacitance. For example, researchers obtain $\frac{\Delta_0}{E_{tls}} p_z \leq$ 2.5 - 6.0 (D) in $\mathrm{a-AlO_x}$ of JJs [34, 125]. However, researchers want more structural information of $p_z$, which is obscured by the added factor of the TLS tunneling energy $\Delta_0$ that is usually unknown. Moreover, the accuracy of $g$ is also limited by the variability of the JJ barrier thickness with a standard deviation of 0.35 nm [37].

To obtain $p_z$ information, we obtain individual TLS's $\Delta_0$ by tuning TLS to its minimum energy (= $\Delta_0$). The applied tuning parameter is an external electric field which is aligned with the $E_{zpf}$. Since the individual TLSs are strongly coupled to the resonator, $E_{tls}$ is extracted when TLSs are near-resonant and we get $p_z$ through Eq. 5.3 (but there is no access to orthogonal components $p_x$ and $p_y$). We use a $\sim$ 20 nm dielectric thickness which allows for a good accuracy of dipole moment $p_z$ extraction relative to in-JJ TLS studies.

In this Chapter, I will briefly overview the previous studies that tune TLS via fields and describe our devices. Later, I will give details of two alumina including the fabrication process, chemical properties, and the TLS spectrum. Last, I will compare our result to the theoretical models including O-H rotors, O-O bonds, H-bonds, etc. We acknowledge Stefan Fritz and Dagmar Gerthsen who deposit the amorphous alumina sample.

## 5.2 Field-tuned TLSs experiments

The schematic and optical image of the resonator used in this Chapter are shown in Fig. 5.1. We name our resonators with voltage tuning as Electrical-Bridge Quantum-Defect Sensor

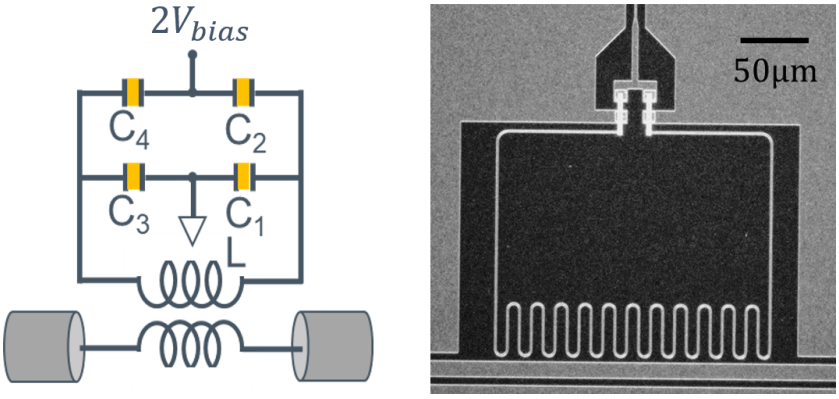


Figure 5.1: Left: the schematic of an Electrical-Bridge Quantum-Defect Sensor (EBQuDS). A voltage bias is applied on the bias port on top. The four equal capacitors have a voltage drop $V_{bias}$. Right: Image of a thin alumina film resonator used in this chapter.

(EBQuDS), which has a capacitor-bridge to minimize the microwave leakage through the voltage bias port. Four equal capacitors have a voltage drop $V_{bias}$, and TLSs are located in the dielectric of capacitors. SiNx TLSs in tri-layer capacitors [105] or on top of inter-digital capacitors [126] have been studied previously by applying static fields. Besides, dynamical fields are also applied to extract the averaged $\bar{p}_z$ but only with logarithmic accuracy [103, 104, 127]. TLSs experience a Landau-Zener (LZ) transition such that the loss tangent of the resonator returns to a universal single-photon loss at a high sweeping rate. This dynamical technique has recently provided evidence for an second type of TLS in amorphous silicon, which has an anomalously large $p$, and is revealed only at high field bias rates due to a gap in its density of states [103]. Other work shows that multiple LZ transitions with destructive interferences can dynamically decouple a quantum system from TLSs [128].

A brief recall of Chapter 2: the variation in the asymmetry energy due to the variation of the surrounding potential structures, electric and strain fields, is

$$\Delta = 2\boldsymbol{\gamma} \cdot \boldsymbol{S} + 2\boldsymbol{p} \cdot \boldsymbol{E} + \Delta'. \tag{5.2}$$

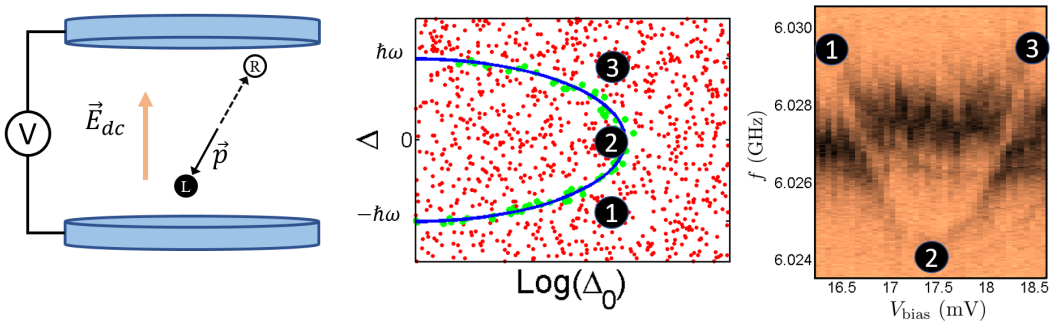


Figure 5.2: Left: An individual TLS within a parallel-plate (tri-layer) capacitor with an applied voltage across two electrodes. Middle: An illustration of the TLS being biased from position 1 to 3 and crossing the resonator frequency in the blue line. Right: The transmission as a function of frequency and the bias voltage for a biased tri-layer LC resonator [9]. One can see a hyperbola which shows how the TLS defects move in energy with bias.

Here $\gamma$ is a tensor defining the TLS's coupling strength to the strain field $S$, $\Delta'$ is the asymmetry energy without any external fields. The consequence of TLS energy in a tri-layer capacitor separated by $l_0$ with a bias voltage drop $V_{bias}$ is

$$E_{tls} = \sqrt{\Delta^2 + \Delta_0^2} = \sqrt{\Delta_0^2 + \left(2p\cos\theta\frac{V_{bias}}{l_0} + \Delta'\right)^2}. \tag{5.3}$$

An illustration and an example of the spectrum are shown in Fig. 5.2. In the right panel, a TLS is sweeping from position "1" to "3" and the according $\Delta$ is shown in the middle panel. The curvature of the hyperbola indicates us the dipole moment $p_z$.

Besides studies on SiNx, a few other field-tuning-studies are aiming on the most common qubit material, amorphous alumina $a - \mathrm{AlO_x}$, in SC qubits. In Ref. [81], they apply a piezo voltage $V_p$ underneath the qubit chip which changes $\boldsymbol{S}$ and observe individual TLSs tuned into their minimum energy as well. Although they are capable of obtaining the information of $\Delta_0$, the accuracy of $p$ is still poor due to the uncertainty of the thickness (or $E_{zpf}$) in JJ barriers. In addition, Brehm *et al.* develops a CPW resonator shunted with a tri-layer capacitor containing

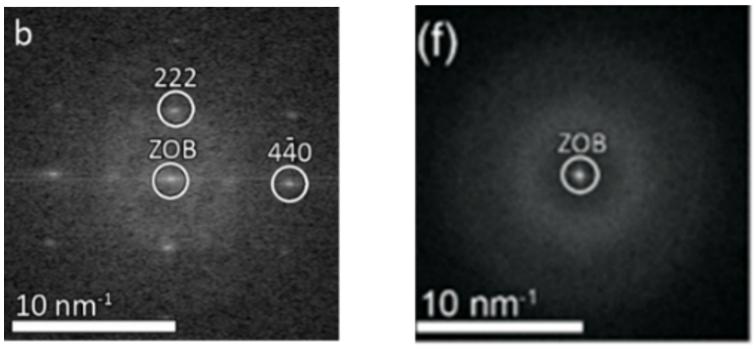


Figure 5.3: Transmission electron microscope diffraction pattern. Left: polyscrystalline sample. Right: amorphous sample. Figure from Ref. [10]

anodic oxidized AlOx, which has a good accuracy of $E_{zpf}$, and extracts a few TLSs with $p$ = 2.3 - 7.4 D [129]. Other field tuned measurements in $a - \mathrm{AlO_x}$, studying the barrier of JJs, detected several moments with $p_z$ = 1.0 - 2.9 D [130]. Below we report on not only alumina in an amorphous phase mimicking the growth of JJs, but also in a polycrystalline phase for comparison.

## 5.3 AlOx properties and deposition

To understand the properties of alumina, we execute the dipole extraction technique on two structural phases: polycrystalline ($\gamma - \mathrm{Al_2O_3}$) and amorphous ($a - \mathrm{AlO_x}$). We find a clear difference in the dipole moment distribution from the film types, indicating a difference in TLS structures. In this section, I will describe the nanochemical properties of these two alumina, where material information on the amorphous phase growth (a-AlOx) is from Ref. [10]. We are measuring two $a - \mathrm{AlO_x}$ films grown under two conditions, 70°C and 250°C, by Stefan Fritz and one $\gamma - \mathrm{Al_2O_3}$ film which is fabricated in-house.

### 5.3.1 Fabrication method of two alumina

- *Polycrystalline films*:

The $\gamma - Al_2O_3$ sample is grown in an LPS electron-beam evaporator. After the HF pre-treatment, a 100 nm Al bottom layer, a 20 nm alumina layer, and a 100 nm Al top layer are *in situ* deposited by the electron-beam evaporation. The alumina layer is evaporated from $\alpha - Al_2O_3$ pellets with 99.99% purity.

- *Amorphous films*:

The major-studied $a - AlO_x$ film is grown by Stefan Fritz in the Dagmar Gerthsen group, and the fabrication of the resonator is performed in the LPS cleanroom. The thermal Al oxidation process is self-limiting on the Al surface and yields $a - AlO_x$ layers with a thickness $\leq$ 2 nm. This thickness range is useful for JJs. However, thicker $a - AlO_x$ layers are required for both quantitative chemical analysis and dipole moment analysis due to the limitations of the used transmission electron microscope with an electron-beam diameter of 1.8 nm and the requirement of suppressing the Josephson effect during voltage biasing, respectively. For this reason, $a-AlO_x$ layers are deposited by iterative oxidation, i.e., after the first oxidation step, 1-nm Al is deposited at 0.1 nm/s and oxidized under a certain condition. We mainly focused on an $a - AlO_x$ sample in this thesis, which is oxidized at 250°C and 9.5 mbar.

Before the deposition, the Si wafer is dipped into diluted HF to remove silicon oxide and the tri-layer of Al/$a - AlO_x$/Al starts with the deposition of 100 nm-Al at 0.5 nm/s. Later, an iterative process is repeated 8 times using the same oxidation conditions (either 250°C or 70°C) and we get $\sim$14.7 nm-thick films. In the last step, a 100-nm-thick upper Al layer is deposited using the same Al-deposition parameters as for the lower Al layer. However, at 250°C, the heat transfer is so strong that the sample plate heater is not capable of keeping the temperature to the set value and the temperature decreases further until the end of the oxidation process. The actual

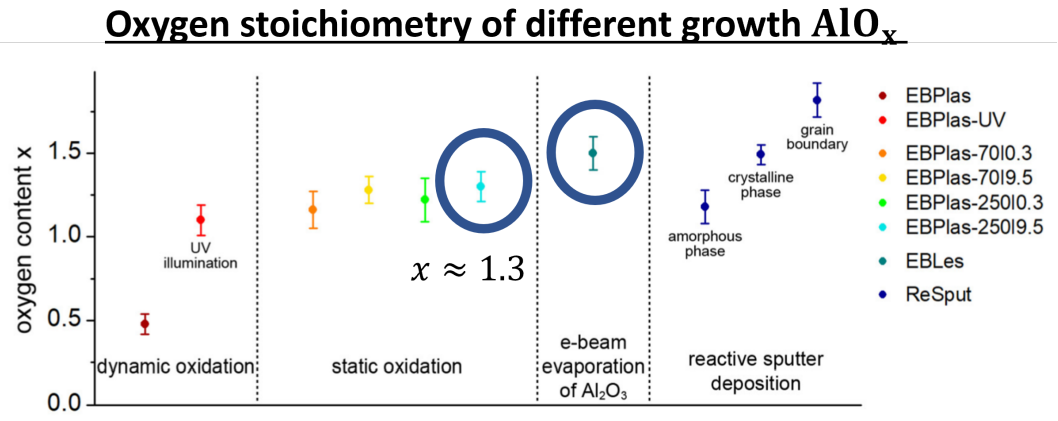


Figure 5.4: Oxygen content x of AlOx layers fabricated with different oxidation techniques and varying oxidation parameters. The two focused films are highlighted in circles. Figure from [10].

oxidation temperature ranges between 300 and 210 °C.

See Fig. 5.3 for the transmission electron microscope (TEM) diffraction patterns for both alumina from Ref. [10]. They find differences in the chemical properties between single and multiple oxidations also between two structural phases which will be discussed later in Chapt. 5.3.2).

### 5.3.2 Nanochemical properties of aluminum oxide

The analysis of nanochemical properties of aluminum oxide is done in Ref. [10]. Two structural phases of alumina have different oxygen content x, which depends on oxidation temperature, oxygen pressure, and growth technique. For amorphous alumina and a constant temperature of 70°C, the oxygen content increases with pressure from x = 1.16 (0.3 mbar) to x = 1.28 (9.5 mbar). The same effect is observed at 250 °C. Similarly, for a constant oxygen pressure, the oxygen content increases slightly with temperature. For example, at an oxygen pressure of 0.3 mbar the oxygen content increases from x = 1.16 (70 °C) to x = 1.22 (250 °C). Both effects can be used to maximize the O content which reaches x = 1.30 for alumina at an oxygen pressure =

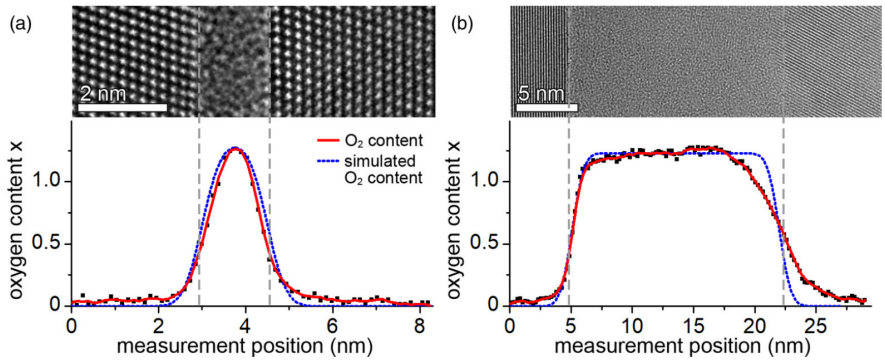


Figure 5.5: TEM images and O-concentration profiles of AlOx layers fabricated by a single oxidation process in (a) and iterative oxidation in (b). The oxidation condition is the same at 250°C and 0.3mbar. Blue dotted lines are simulated O-concentration profiles for AlOx layers with an ideal abrupt Al/AlOx interface. See Ref. [10] for more detail.

9.5 mbar and at 250 °C. On the other hand, the $\gamma - Al_2O_3$ sample contains an oxygen content of x = 1.5 as expected for the stoichiometric crystalline phase. See Fig. 5.4 (or Ref. [10]) for the oxygen content of alumina layers fabricated by different processes. The films types that we study with the EBQuDS are marked with blue circles.

The motivation is to study TLSs in the amorphous phase from a thicker film fabricated by the process similar to the one in JJ. However, thick $a - AlO_x$ layers deposited by an iterative Al-deposition/oxidation process may have modified the $a - AlO_x$ properties leading to differences between thin and thicker layers. One difference is the existence of nano-crystalline unoxidized Al islands, which are only present in the thick $a - AlO_x$ layers. For static oxidation at high oxygen pressure and high temperature, the amount of Al island is found to be less than 3% in volume. The other difference is the oxygen content distribution. The oxygen distribution throughout the thin and thick $a - AlO_x$ can be visualized by O-concentration profiles in Fig. 5.5. O-concentration gradients are identical at the upper and lower Al/$AlO_x$ interfaces of the thin layer. In contrast, the broadened O transition at the upper and lower interface of the thick layer are not the same, and

the reason is unknown. Note that the TLS properties might depend on oxygen content such that TLSs in the JJ barrier and our film are different.

## 5.4 TLS statistics analysis and intrinsic material density

We are able to extract hundreds of TLS dipole moments and analyze the histogram $H(p_z)$ (e.g. Fig. 5.8). Before showing our experimental result, I would like to introduce a transformation from $H(p_z)$ into intrinsic material properties, such as the TLS density $D(p_z)$ or single photon loss tangent. The derivation of $H(p_z)$ to $D(p_z)$ is adapted from Ref. [131] and Dr. Osborn's notes.

At a given electric field bias range $\Delta \mathrm{E}_{ex}$, TLSs with larger dipole moments have a larger shift in asymmetry energy $\Delta$ relative to smaller moments, and this leads to a higher probability of the former moments having their energy minimum within the resonator bandwidth. As a result, $H(p_z)$ is not an intrinsic material property instead of a statistical bias. To obtain the relationship between the $D(p_z)$ and $H(p_z)$, we start from the standard tunneling model [76, 77]. The authors assume that the density of levels per unit volume and energy, $n(\Delta, \Delta_0)$, depends on tunneling energy $\Delta_0$ but is uniform in $\Delta$ giving

$$n(\Delta, \Delta_0)\, d\Delta d\Delta_0 \;=\; \frac{P_0}{\Delta_0}\, d\Delta d\Delta_0, \tag{5.4}$$

where $P_0$ is a constant in unit of $1\,/(\,J\,m^3)$. However, the model only considers a single moment $|\overrightarrow{p}| = p$ and the dipole direction is isotropic. In our experiments, we notice the dipole moment in the z-axis is not uniform and we add distributions in dipole direction and moment value. For a

general case, we write

$$n(\Delta,\, \Delta_0,\, \overrightarrow{p})\, d\Delta d\Delta_0 d^3p \;=\; \frac{P_0'}{\Delta_0}\, D(\overrightarrow{p})\, d\Delta d\Delta_0 d^3p, \tag{5.5}$$

where $D(\overrightarrow{p})$ is a generalized material TLS distribution and $P_0'$ is a new constant. $D(\overrightarrow{p})$ depends on 3 Cartesian coordinates, but we only have measurement access to one component, $p_z$. The full investigation of $D(\overrightarrow{p})$ is beyond the scope of this thesis, and therefore we assume that $D(\overrightarrow{p})$ is separable in $p_x$, $p_y$, and $p_z$. Without loss of generality, we consider a simple case

$$n(\Delta,\, \Delta_0,\, p_z) d\Delta d\Delta_0 dp_z \;=\; \frac{D(p_z)}{\Delta_0}\; d\Delta d\Delta_0 dp_z, \tag{5.6}$$

where $\int D(p_z)\, dp_z \;=\; P_0$ and $D(p_z)$ is measurable in our experiments. In TLS spectroscopy, $V_{bias}$ is known such that $p_z$, $\Delta_0$, and $\Delta'$ can be extracted for individual TLSs and $\Delta \;=\; \Delta' + \frac{2\, p_z V_{bias}}{l_0}$. Next, we change variables to include $V_{bias}$ through Jacobian transformation giving

$$d\Delta dp_z \;=\; dp_z\, dV_{bias} \begin{vmatrix} \frac{\partial \Delta}{\partial p_z} & \frac{\partial \Delta}{\partial V_{bias}} \\ \frac{\partial p_z}{\partial p_z} & \frac{\partial p_z}{\partial V_{bias}} \end{vmatrix} = \frac{2\, p_z}{l_0}\, dp_z\, dV_{bias}. \tag{5.7}$$

$N_{tot}$ is the total number of observed TLSs from measurement histogram $H(p_{zi})$ and

$$N_{tot} \;=\; \sum_i\; H(p_{zi})\, \Delta p_{zi}, \tag{5.8}$$

where $p_{zi}$ is the center value and $\Delta p_{zi}$ is the bin width of the i-th bin. $N_{tot}$ can also be written

related to Eq. 5.6 as

$$N_{tot} = V \int n(\Delta,\, \Delta_0,\, p_z) d\Delta d\Delta_0 dp_z. \tag{5.9}$$

Substituting Eq. 5.7 into the above equation, we have

$$N_{tot} \,= V \int_{p_{min}}^{p_{max}} D(p_z) \cdot \frac{2\,p_z}{l_0}\, dp_z \int_{V_1}^{V_2} dV_{bias} \int \frac{d\Delta_0}{\Delta_0}. \tag{5.10}$$

Similarly, we consider the i-th bin of $H(p_{zi})$ and the number of TLSs in this bin

$$N_i = H(p_{zi})\, \Delta p_{zi} \tag{5.11}$$

If $\Delta p_{zi}$ and $\Delta_0$ are small enough, we obtain

$$H(p_{zi})\, \Delta p_{zi} = V\, \frac{2\,p_{zi}}{l_0}\, D(p_{zi})\, \Delta p_{zi}\, \Delta V_{bias}\, \frac{\Delta f_0}{f_0} \tag{5.12}$$

or

$$D(p_z) \,= \frac{1}{V}\, \frac{H(p_z)}{2\,p_z}\, \frac{l_0}{\Delta V_{bias}}\, \frac{f_0}{\Delta f_0}, \tag{5.13}$$

where $\Delta f_0$ = 50MHz is the measurement frequency span. Thus, we prove that $D(p_z)$ is not proportional to measured histogram $H(p_z)$, but $D(p_z) \propto \frac{H(p_z)}{p_z}$. Last, we can obtain the material constant

$$P_0 \,= \int D(p_z) dp_z$$

$$\approx \sum_i \frac{1}{V}\, \frac{1}{p_{zi}}\, \frac{l_0}{2\,\Delta V_{bias}}\, \frac{f_0}{\Delta f_0}. \tag{5.14}$$

## 5.5 TLS microwave measurements

All measurements in this chapter are done at temperature $< 15$ mK to minimize the thermal populations.

### 5.5.1 TLS spectrum of polycrystalline $\gamma - \mathrm{Al_2O3}$

An example single transmission trace $|S_{21}|$ vs frequency $f$ is shown in Fig. 5.6 top panel in blue. Within the bandwidth of the resonator, a few fine resonance dips reveal the energies of individual TLSs. Fig. 5.6 middle panel shows a TLS spectrum example, $|S_{21}(f)|$ at various dc-field $\mathrm{E_{ex}} = \frac{V_{bias}}{l_0}$ from a $\gamma - \mathrm{Al_2O_3}$ sample. TLS energies exhibit hyperbolic energies versus $\mathrm{E_{ex}}$ in agreement with Eq. 5.3. I estimate the $\Delta_0$ from the minimum of the TLS energy ($\min(E_{tls}) = \Delta_0$), and $p_z$ from the hyperbola – a steeper curvature gives a larger dipole moment. An optimized Monte Carlo fit is performed on each TLS energy to extract $p_z$ of the specific TLS (see Appendix. B.1). Only well defined TLS energy curves are selected for analysis. Two examples of extracted $p_z$ are labeled in the boxes and the fits are plotted as blue hyperbolas in Fig. 5.6 bottom panel.

Next, we obtain an approximate intrinsic material loss tangent $\tan\delta^0$ by using the averaged transmission rate $S_{21,avg} = \sum_i S_{21}(V_{bias,i}) / \sum_i 1$ from different voltage biases. $|S_{21,avg}|$ is shown as the solid black curve in Fig. 5.6 top panel. A fit (dashed red curve) to $S_{21,avg}$ yields $\tan\delta^0 = 1/Q_i = 1/680 = 1.5 \times 10^{-3}$ and $Q_e$ is extracted as $\mathrm{Q_e} = 2\pi f_0/\kappa_e = 590$.

TLSs change their energies randomly during cool-downs from room temperature. From four different cool-downs, we created different sets of TLSs in the two resonators. The two histograms and statistics are shown in Fig. 5.7 and Table. 5.1. The mean $p_z$ of $H(p_z)$ are 3.5(1) and 3.6(1), for Res1 with $f_0$ = 4.35 GHz and Res2 with $f_0$ = 4.95 GHz, respectively.

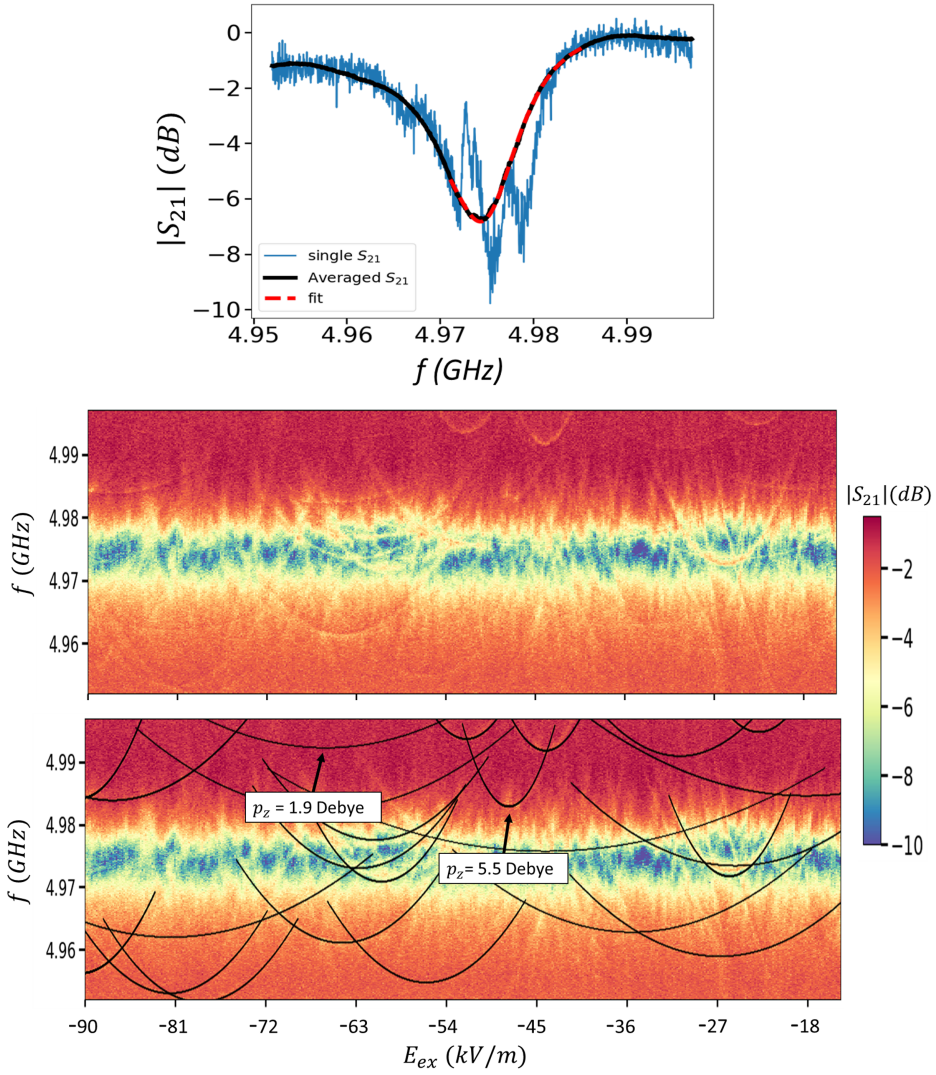


Figure 5.6: Top: $|S_{21}|$ of a $\gamma - Al_2O_3$ resonator. It shows multiple dips indicating TLSs strongly coupled to the resonator. The black curve is the ensemble average $|S_{21,avg}|$, obtained by averaging all $S_{21}$ in the next panel. The intrinsic quality $Q_i$ is $1\ /\ (1.47 \times 10^{-3}) \approx 680$ according to the red fitting line. Bottom: Color scale plot of $|S_{21}|$ vs probe frequency $f$ and electric field $E_{ex}$. Data show a main resonance at 4.974 GHz. Several local minima in $|S_{21}|$ reveal the energy of individual TLSs. Several TLSs in blue hyperbolas are fitted to the energy model (Eq. 5.3), where $p_z$ comes from the curvature of the energy hyperbola.

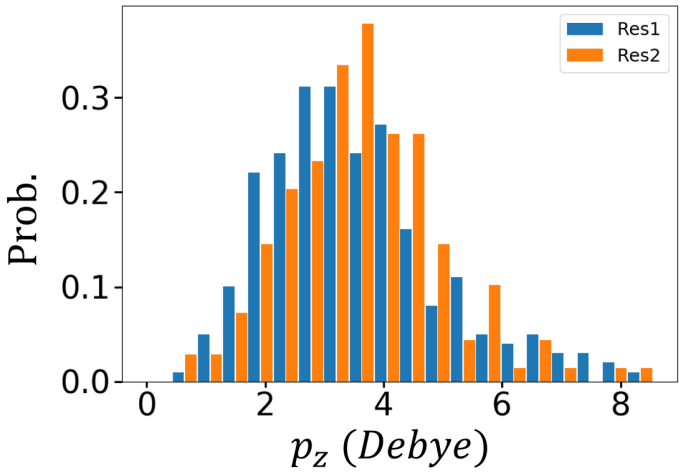


Figure 5.7: Histograms of $p_z$ from two different $\gamma - Al_2O_3$ resonators.

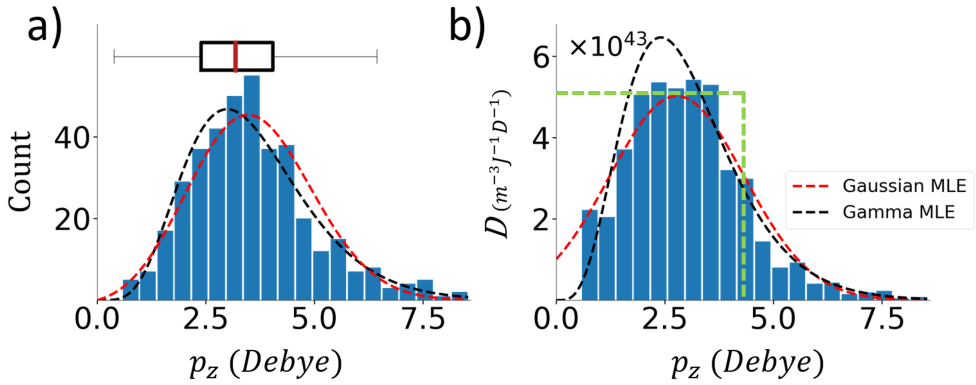


Figure 5.8: Histogram $H(p_z)$, material TLS density $D(p_z)$, and distribution fits. The chosen functions to fit $D(p_z)$ are a Gaussian function (red) and a gamma function (black). The fitting method is shown in Appendix B.2. (a) $H(p_z)$ of 394 TLS moments from polycrystalline phase. A Seaborn box is plotted to show measured (not material) statistics, including the mean moment, a 25% and 75% range (dark box), and data range (bar limits). (b) $D(p_z) \propto H(p_z)/p_z$ after accounting for the experimental weighing factor. From the Gaussian fit, we report the material mean $p_z$ of 2.6 D and standard deviation $\sigma$ = 1.6 D. The yellow-green dashed line illustrates a possible material density if we assume an isotropic TLS direction. Since we expect the distribution $> 0$ when $p_z = 0$, the gamma distribution is not preferred.

According to the standard TLS distribution [76, 77], TLSs have log-uniform $\Delta_0$ such that there are negligible distribution changes for TLS tunneling energies that are only 0.6 GHz different in our two resonator frequencies. We, therefore, combine all the data from different runs in the two resonators to enlarge the sampling number and improve the statistics. The accuracy of extraction is limited by the uniformity of thickness of alumina rather than the fitting process. A total of 394 TLSs from two resonators are analyzed to form the measured $p_z$ distribution $H(p_z)$ with an average of 3.5 $\pm$ 0.4 Debye (D) shown in Fig. 5.8 left panel. A Seaborn box is plotted on top of the left panel, where the red color line is the mean line, and the right and left sides of the box represent 25$^{\text{th}}$ and 75$^{\text{th}}$ percentage of dipole moment data. The intrinsic material TLS dipole distribution $D(p_z)$ is related to TLS material density $P_0 = \int D(p_z)\, dp_z$ (in units of $J^{-1}m^{-3}$). The transformation is derived in Eq. 5.13 with a $S_{21}$ span $\Delta f_0$ = 50.0 MHz, and $D(p_z)$ is shown in the right panel. The dashed lines in Fig. 5.8 show the fits using a maximum likelihood estimation (MLE) method (Appendix B.2). The chosen functions to fit $D(p_z)$ are a Gaussian function (red) and a gamma function (black). From the fit of a Gaussian related distribution, we find that $D(p_z)$ has a mean dipole moment $\bar{p}_z$ = 2.6 $\pm$ 0.3 D (= 0.54 $\pm$ 0.05 e$\mathring{A}$) and $\sigma$ = 1.6 D ( = 0.33 e$\mathring{A}$). The computed TLS density $P_0$ is $1.0 \pm 0.1 \times 10^{44}(\text{J}^{-1}\text{m}^{-3})$. This computed value of TLS density along with the dipole moments agrees with the measured loss tangent. As a result, we used the material units in the right panel.

| | mean measured $p_z$ (D) | standard deviation (D) |
|---|---|---|
| Res1 (4.35 GHz) | 3.55 | 1.47 |
| Res2 (4.95 GHz) | 3.64 | 1.3 |

Table 5.1: Mean and standard deviation of extracted TLS $p_z$ in $H(p_z)$ for each $\gamma - Al_2O_3$ resonator.

For amorphous samples or random voids within polycrystals, we expect TLS dipoles to be random in angle (isotropic). For the case of one single dipole magnitude $p_0$ and isotropic angle $\theta$, the distribution in $\cos\theta$ or $p_z$ is uniform. Therefore, $D(p_z)$ is expected to be independent of $p_z$ until the maximum value $p_0$. As a guide to the eye, an isotropic distribution (random angle) with dipole moment $p_0$ = 4.5 D is shown as a yellow-green dashed line in Fig. 2 5.8. The positive slope in the observed distribution indicates that we have a departure from isotropic distribution (since isotropic TLSs give only a non-positive slope or a monotonic decrease). Thus, data in Fig. 5.8 shows that TLSs can be different than the standard model for TLSs. The anisotropic angular distribution may be caused by the polycrystalline film texture (crystallite orientation) which influences the TLS orientation. Additionally, an interesting modified model attempts to explain the anisotropy [132], and more experiments are needed to characterize its validity.

### 5.5.2 TLS spectrum of 250°C amorphous oxide

Fig. 5.9 shows a TLS spectrum, an adjusted spectrum, spectrum with TLS fits. The $a-\mathrm{AlO_x}$ spectra are not as clear as $\gamma-\mathrm{Al_2O_3}$ ones due to higher noise in the spectra, despite using the same setup. In addition, since the 70° $a-\mathrm{AlO_x}$ has less clear spectra (see Fig. C.3) than that of 250° $a-\mathrm{AlO_x}$ probably due to a larger unoxidized Al island volume ratio, we focus on 250° $a-\mathrm{AlO_x}$ sample. To improve the TLS signal contrast, the $S_{21}$ data is shown after processing in panel (b). For our first processing step, we subtract $S_{21,avg}$ from $S_{21}$ and then multiple $|S_{21,avg}|$:

$$S'_{21}(f) = (S_{21}(f) - S_{21,avg}(f)) \times |S_{21,avg}(f)|. \tag{5.15}$$

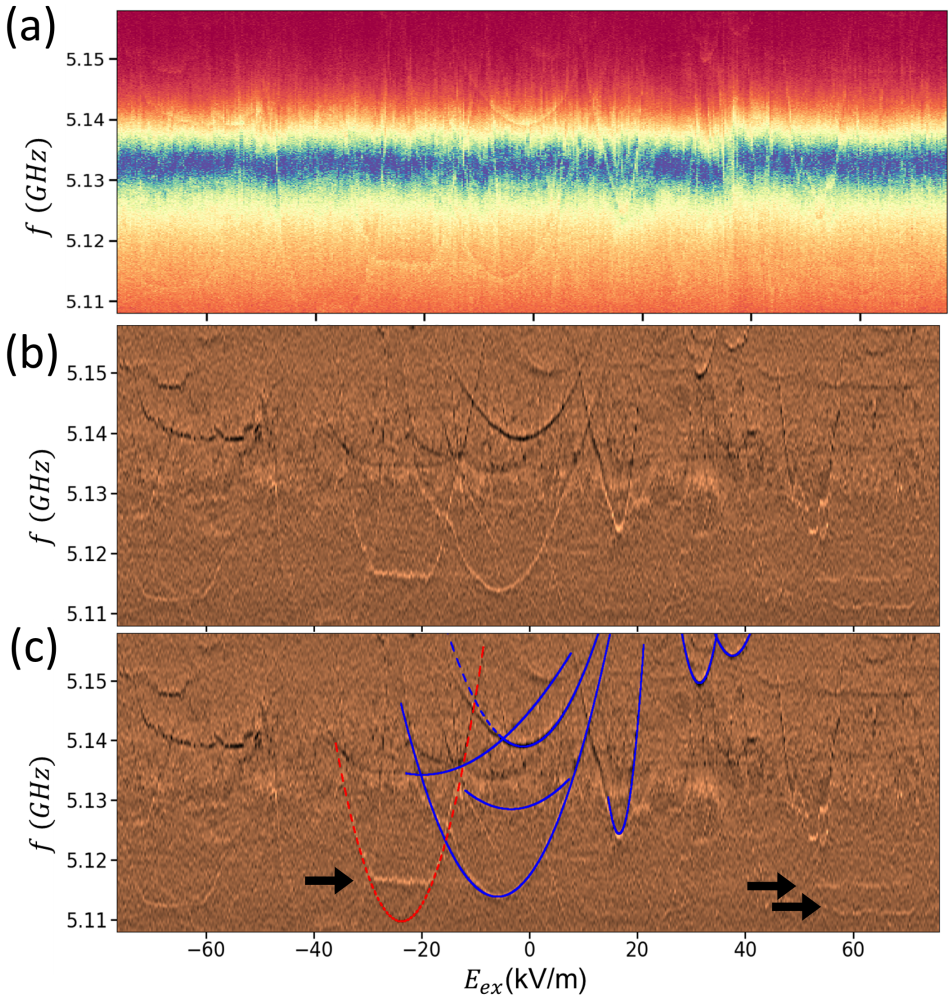


Figure 5.9: (a) Color scale plot of $|S_{21}|$ vs $f$ and electric field $\mathrm{E_{ex}}$ from a $\mathrm{a-AlO_x}$ resonator. (b) Example of processed transmission data. The LC resonance is approximately 5.132 GHz (no longer visible after data processing). (c) The same data with traces fit to TLS energy function. 7 fitted dipole moments are extracted at values of 3.2 - 12.7 D. TLSs whose energy does not depend on bias voltage are marked by arrows. Curved red dashed trace shows an anomalous TLS; it switches between a hyperbola and nearly constant energy of 5.116 GHz at $E_{ex} = -30$ kV/m and $E_{ex} = -18$ kV/m.

In the next processing step, we apply a low-pass filter function $\mathcal{F}(x)$ in the frequency domain and take the derivative with respect to frequency:

$$S_{21,plot} = \frac{d}{df}\left(\mathcal{F}(S'_{21}(f))\right) \tag{5.16}$$

We plot $S_{21,plot}$ in Fig. 5.9 (b) and (c) in an arbitrary unit and add hyperbolic fitting traces (blue lines) in the panel (c).

As we will show in detail below, TLSs within $a - \mathrm{AlO_x}$ are less stable than those in $\gamma - \mathrm{Al_2O_3}$. The $a-\mathrm{AlO_x}$ TLSs show sudden switchings in energy or even become invisible within the resonator bandwidth in time, making it more difficult to identify individual TLSs. This leads to a higher error in the Monte Carlo fit. We also observed energy features that are almost independent of $E_{ex}$, as indicated by black arrows. They are not expected because all coupled TLSs should be frequency tunable in the device. Surprisingly, one of them seems to be only partially described by hyperbola in the red-dashed curve. Increasing bias voltage at -30 kV/m, this TLS seems to switch from a regular TLS state to an unknown state which has constant transition energy under bias until -19 kV/m and finally switches back to normal TLS behavior. This indicates an unexpected state near its energy minima $\Delta_0$, which we believe has not been identified previously. At -8 kV/m, one hyperbola seems to change slope (as indicated by the start of a blue dashed line), although this event may represent two separate TLSs.

Unlike the polycrystalline sample, the amorphous films show most of the hyperbolas from TLSs in the bias range of $-30$ to $30$ $\mathrm{kV/m}$. Outside of this range, TLS tracks are seen, but they do not typically trace out a smooth hyperbola. Furthermore, we find that most TLSs do not appear with the same parameters ($\Delta_0$,$\Delta'$, and $p_z$) after repeating the voltage scanning within

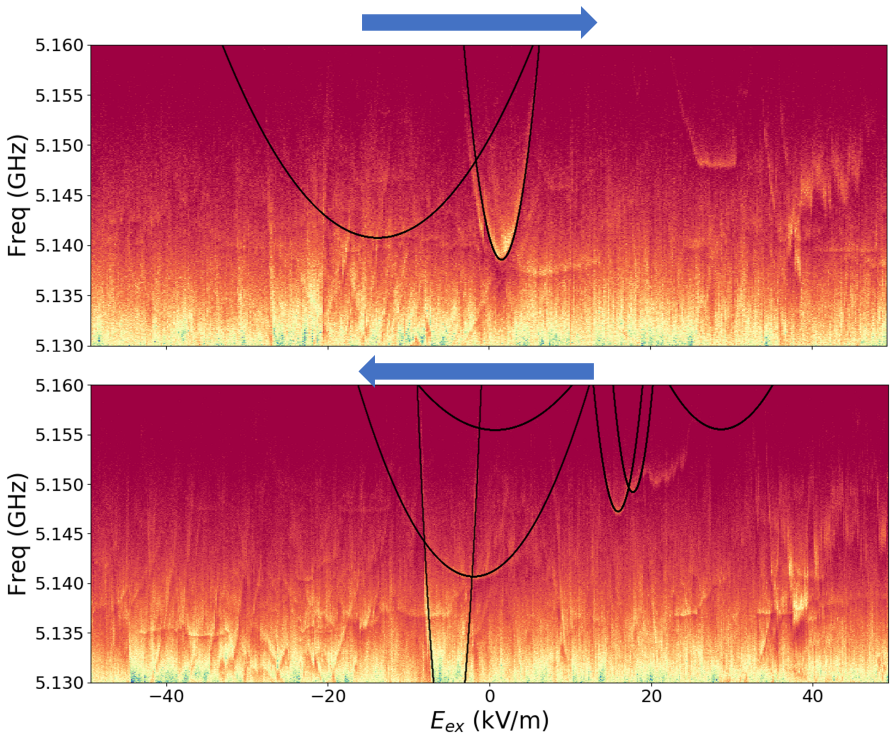


Figure 5.10: TLS spectrum of $a - \mathrm{AlO_x}$ sample scanned from low-to-high in voltage (top) and high-to-low in voltage (bottom). The two scans are measured without time interval. We find TLSs are not repeatable after the voltage bias changes direction.

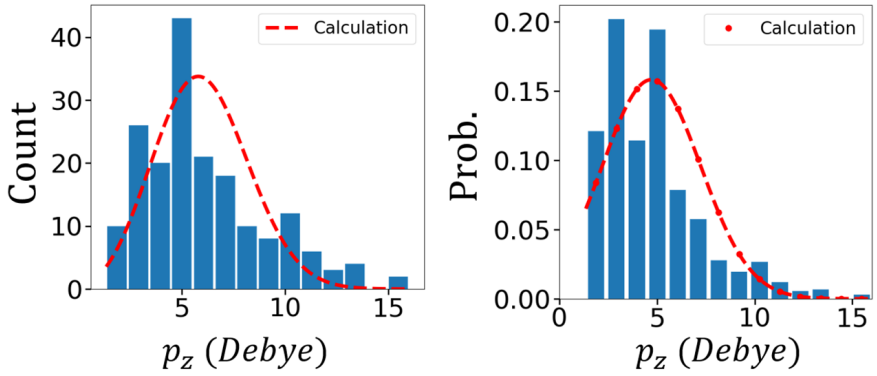


Figure 5.11: Left: The measured distribution of 189 $a - \mathrm{AlO_x}$ TLSs. Right: The probability of the material TLS dipole distribution. Dashed lines are acquired by calculation of Eq. 5.17, and we report a mean dipole = 4.6 $\pm 0.5$ D and $\sigma$ = 2.5 $\pm 0.3$ D (not from a Monte Carlo fit). Analysis of missing measured dipoles is needed, but even afterwards the mean value is larger in this material than in $\gamma - \mathrm{Al_2O_3}$ (see Chapter 5.5.6).

the same cool-down. An example in Fig. 5.10 shows two TLS spectra measured consecutively without a pause, where the first one is shown as the top panel and is scanned from low-to-high in voltage, and the second is shown on bottom and scanned from high-to-low in voltage. In a small fraction of TLS hyperbola ($< 3\%$), TLS traces appear with the same dipole and $\Delta'$ is within 1 MHz, such that they are regarded from the same TLS and counted only once in distribution. In $a - \mathrm{Al_2O_3}$, we identify and analyze a total of 189 TLSs using multiple field sweeps and cool-downs according to the above procedure. The measured distribution $H(p_z)$ with counts and the probability of material distribution $D(p_z)$ are shown in Fig. 5.11. $H(p_z)$ shows a broad range in value from 0.5 to 16 D with an average of 6.0 D and the interquartile range (range from the $25^{\mathrm{th}}$ to $75^{\mathrm{th}}$ points) of 3.8 D. Because of the large deviation, we cannot get a reasonable fitting to a Gaussian function, which yields a mean value of 1.6 D and standard deviation of 4.2 D. Instead, we calculate the material average dipole moment $\langle p_z \rangle$ of $D(p_z)$ from $H(p_z)$ by

$$\langle p_z \rangle = \frac{\int p_z D(p_z) dp_z}{\int D(p_z) dp_z} = \frac{\int H(p_z) dp_z}{\int p_z^{-1} H(p_z) dp_z} \tag{5.17}$$

The standard deviation $\sigma$ is done in a similar way. From this we find $\langle p_z \rangle = 4.6 \pm 0.5$ (= 0.96$\pm$0.1 e$\mathring{A}$) and $\sigma$ = 2.5$\pm$0.3 D (= 0.52$\pm$0.05 e$\mathring{A}$). A guiding Gaussian curve with these two parameters are plotted in red.

### 5.5.3 Loss tangent from dipole moment histograms

From $D(p_z)$, we are able to derive the statistical loss tangent $\tan\delta_s^0$. The comparison of $\tan\delta_s^0$ to the loss tangent $\tan\delta_f^0$ obtained from $S_{21,avg}$ is an important completeness check of the histogram. Following Ref. [86], Chapter 5.4 and Eq. 2.44, loss due to TLSs can be described as

$$\tan\delta = \int \frac{p_z^2}{\varepsilon} \frac{-\frac{1}{T_2}\tanh(\frac{E_{tls}}{2k_BT})}{(T_2^{-2} + \Omega^2\frac{T_1}{T_2}) + (\frac{E_{tls}}{\hbar} - 2\pi f_0)^2} d^3n$$

$$= \int_0^{E_{max}} dE_{tls} \int_{u_{min}}^1 \frac{u}{\sqrt{1-u^2}} du \int D(p_z)\frac{p_z^2}{\varepsilon} \frac{-\frac{1}{T_2}\tanh(\frac{E_{tls}}{2k_BT})}{(T_2^{-2} + \Omega^2\frac{T_1}{T_2}) + (\frac{E_{tls}}{\hbar} - 2\pi f_0)^2} dp_z, \quad (5.18)$$

where $\varepsilon$ is the permittivity constant, $\Omega$ is the Rabi frequency, $u = \Delta_0/E_{tls}$ and $T_1$ ($T_2$) is TLS relaxation (decoherence) time. The integral of $u$ can be separated and

$$\int_{u_{min}}^1 \frac{u}{\sqrt{1-u^2}} du = \sqrt{1-u_{min}^2} \approx 1, \quad (5.19)$$

where $u_{min}$ is close to 0. In the case when $\Omega^2 T_1 T_2$ is much smaller than 1 and low temperature, the equation is in the single-photon regime, and the fraction part besides $p_z$ is a Lorentzian function,

whose integral is $\pi$. Therefore, we obtain

$$\tan\delta_s^0 = \frac{\pi}{\varepsilon}\int D(p_z)p_z^2 dp_z. \tag{5.20}$$

Through the substitution of Eq. 5.13, we can estimate the loss tangent from $H(p_z)$:

$$\tan\delta_s^0 = \frac{\pi}{\varepsilon}\frac{1}{V}\int \frac{H(p_z)}{2\,p_z}\frac{l_0}{\Delta V_{bias}}\frac{f_0}{\Delta f_0}\,p_z^2\,dp_z$$

$$= \frac{\pi}{2\,\varepsilon}\frac{l_0}{V\,\Delta V_{bias}}\frac{f_0}{\Delta f_0}\int H(p_z)\,p_z\,dp_z$$

$$\approx \frac{\pi}{2\,\varepsilon}\frac{l_0}{V\,\Delta V_{bias}}\frac{f_0}{\Delta f_0}\sum H(p_z)p_z\Delta p_z$$

Finally, we have loss tangent from discrete $p_z$ as

$$\tan\delta_s^0 \approx \frac{\pi}{2\,\varepsilon}\frac{l_0}{V\,\Delta V_{bias}}\frac{f_0}{\Delta f_0}\sum_i p_{zi}. \tag{5.21}$$

Note that the function is $\pi$ times larger than the equation (S6) in Ref. [9]. A comparison of $\tan\delta_s^0 = 1.41\times10^{-3}$ from the TLS histogram to $\tan\delta_f^0 = 1.47\times10^{-3}$ from the transmission fits in polycrystalline film shows a difference less than 2% indicating we capture most of the TLSs.

Unlike in $\gamma - Al_2O_3$, in the amorphous sample, $\tan\delta_s^0$ = 3.2(3) $\times10^{-4}$ does not match $\tan\delta_f^0 = 1/\overline{Q_i} = 1\times10^{-3}$ and $\tan\delta_f^0$ is distinct with every cooldown, where the mean $\overline{Q_i}$ = 1020. We anticipate that $\tan\delta_s^0$ is smaller than $\tan\delta_f^0$, since there are unfittable TLSs due to TLS

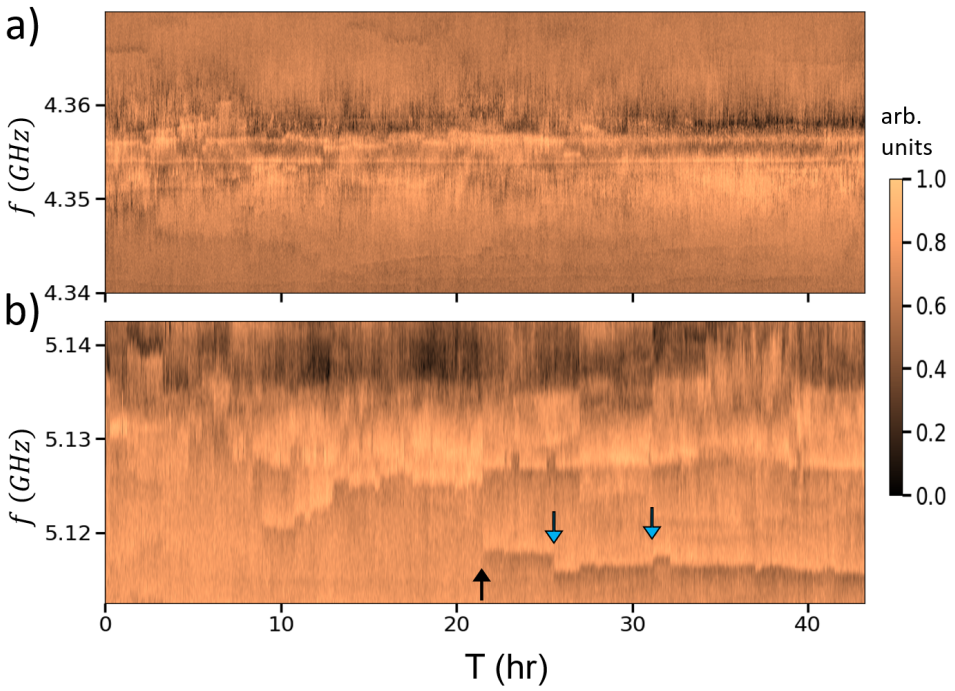


Figure 5.12: Time dependence of processed $|S_{21}|$ with a frequency range $\geq$ 30 MHz. (a) $\gamma - Al_2O_3$ spectroscopy versus time shows the TLSs are relatively stable in frequency near the transmission minimum for 10s of hours. (b) $a - AlO_x$ spectroscopy versus time shows relatively large TLS energy switching and drift.

noise.

### 5.5.4 TLS spectrum in the time domain

To decipher the role of TLS-TLS interaction, we conduct temporal spectroscopy for the two different film types. Fig. 5.12 shows the processed $S_{21}$ traces (the same process mentioned in Chapter 5.5.2) observed over many hours. This resonant TLS noise is believed to be caused by interactions with thermally excited low-frequency TLSs [85]. As shown in Fig. 5.12 (a), TLSs in the $\gamma - Al_2O_3$ film near the resonance frequency are relatively stable: their energies drift by less than 2 MHz over tens of hours. On the contrary, TLSs in $a - AlO_x$ behave similarly to Ref. [133]. TLSs show irregular drifts of more than 5 MHz, including multiple telegraphic switching events

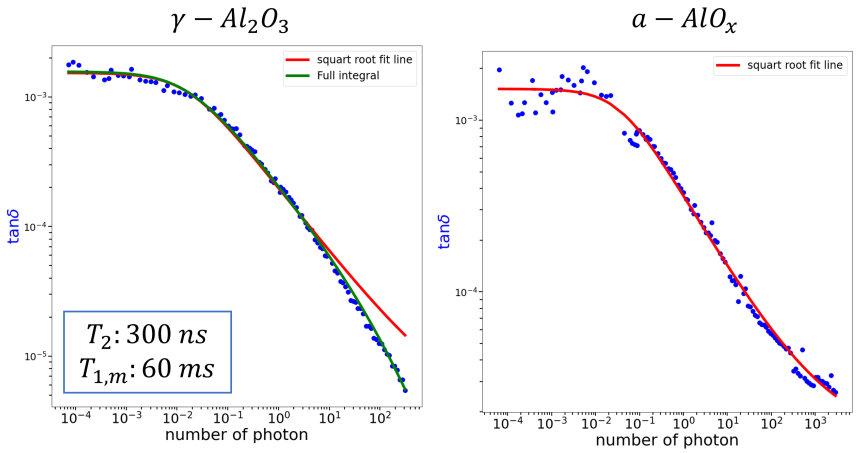


Figure 5.13: Loss tangent vs number of photon. Square root power law fits (Eq. 2.47) are shown in red. Left: polycrystalline film. At high photon numbers, the data is deviated from Eq. 2.47 in red. On contrary, the fit of Eq. 2.44 (green) yields $p_z$ = 2.6 D, $T_{1,min}$ = 60 ms and $T_2$ = 300 ns. Right: amorphous film. Eq. 2.47 can explain the loss tangent implying $T_1 \approx T_2$, even through spectral diffusion is observed.

(blue arrows) and ergodic abrupt TLS shifts (black arrow). Due to the larger dipole moments observed in $\mathrm{a-AlO_x}$, we expect a larger mutual TLS interaction than that in $\gamma - \mathrm{Al_2O_3}$ (if the low-frequency thermally activated $\mathrm{a-AlO_x}$ TLSs have also larger dipole moment).

### 5.5.5 Power dependent loss tangent

The measurement of $\tan\delta$ at various power is a common way to understand the interaction of ensemble of TLSs and microwaves. As discussed in Chapter. 2, we are generally using a square-root power law (Eq. 2.47) to fit the $\tan\delta$. However, in a rare case of $T_1 \gg T_2$, we require to use Eq. 2.44. We plot $\tan\delta$ vs photon number $n$ from $\gamma - \mathrm{Al_2O_3}$ (left) and $a - \mathrm{AlO_x}$ (right) sample in Fig. 5.13. On the left panel, we observe the fit of approximated equation 2.47 in red cannot explain $\tan\delta$ at a high $n$ instead Eq. 2.44 is needed. The fit in green yields the extracted fitting parameters $T_{1,min}$ = 60ms and $T_2$ = 300 ns by using $\hbar\Omega_0 = 2p_z E_{zpf}\sqrt{n}$, where $p_z$ = 2.6 D.

On the other hand, since spectral diffusions and telegraphic noises are observed in $a-\mathrm{AlO_x}$

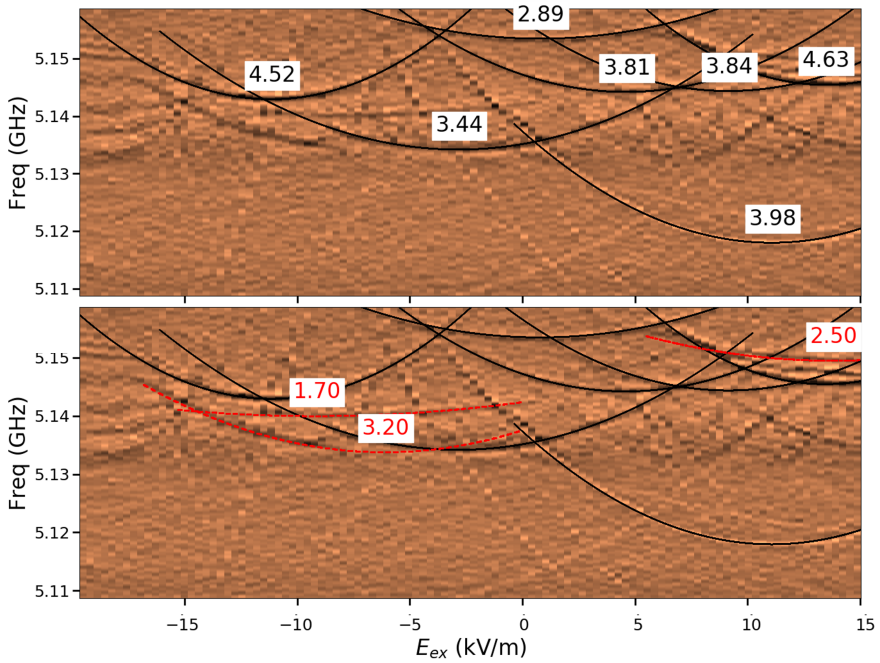


Figure 5.14: One TLS spectroscopy of $a - \mathrm{AlO_x}$ TLS. Top: TLS fitting results and their dipole $p_z$ (D). Bottom: TLSs with incomplete hyperbolas in red and their potential $p_z$ (D)

sample, it is possible that the traditional steady state STM model is not valid and the logarithmic function matches [85]. Surprisingly, $a - \mathrm{AlO_x}$ result is consistent with Eq. 2.47 in contrast to the results of 2D planar resonators [92,93] and our vacuum gap resonators. We will discuss a possible explanation later in Chapter 6. Moreover, since Eq. 2.47 agrees with the data, we suggest that $T_1$ in $a - \mathrm{AlO_x}$ is much lower than that in $\gamma - \mathrm{Al_2O_3}$ if $T_2$ is similar in both films.

### 5.5.6 Missing TLSs and overestimating mean dipole moment

From Chapter 5.5.3, we realized $\tan\delta_s^0$ is far smaller than $\tan\delta_f^0$ in the amorphous sample. There are many unfitted TLSs in the spectra and we should be careful in concluding the analysis of the histogram.

Due to the larger average dipole moments observed in $a - \mathrm{AlO_x}$, we expect a larger interaction from thermal TLSs (illustrated in Fig. 2.14) than that in $\gamma - \mathrm{Al_2O_3}$. The mutual interaction

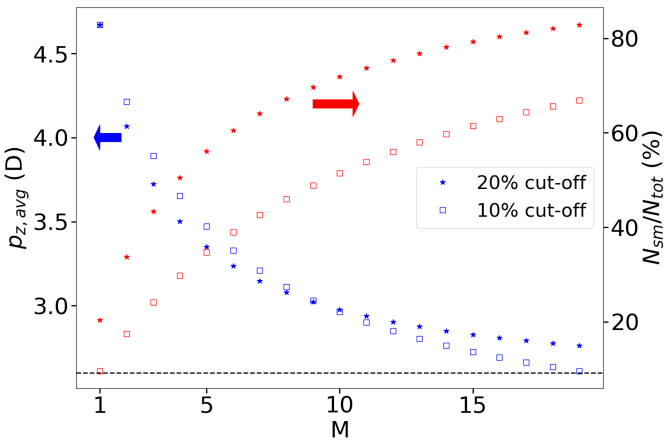


Figure 5.15: Computed average dipole for different conditions of plausible missing TLSs in the amorphous film. We assume 10th (2.8 Debye) or 20th (3.5 Debye) percentile in original data as small $p_z$ TLS in square or in star marks respectively. Small $p_z$ TLSs in the distribution are multiplied by the multiplication factor M to simulate possible missing TLSs. The original data is when M = 1. The black dashed line represents the average dipole in $\gamma - Al_2O_3$. We take M=5 as the most possible case for our data, implying $p_{z,avg} > 3.3$ D in amorphous alumina film.

is observed in Fig. 5.12, where the $a - \mathrm{AlO_x}$ TLS spectrum in the time domain is indeed more unstable. TLSs are switched in energy randomly during voltage biasing, and thus it is difficult to extract their $p_z$. For example, a 2 Debye hyperbola track in $a - \mathrm{AlO_x}$ data took about 10 hours to obtain and might experience one to three frequency jumps. Moreover, a small dipole moment TLS has a small coupling ($g \propto p$) to the resonator which has a small dip in $S_{21}$. It is more likely that the dip is covered by microwave noise when we are probing at low power. Because of the unstable TLSs due to mutual TLS interaction, and resonator signal-to-noise ratio, we are prone to measure the larger dipole moments than the smaller ones, especially in the amorphous sample. Those TLSs without crossing their minimum are not counted in statistics due to the high uncertainty. We show a few examples in Fig. 5.14, where preliminary manual fits are shown in red dashed lines, which are generally small in $p_z$. With a closer look, one can see some other potential small dipole moment TLSs at the edges of the figure.

Here we estimate a case when we miss M-1 out of M small dipole moment by multiplying

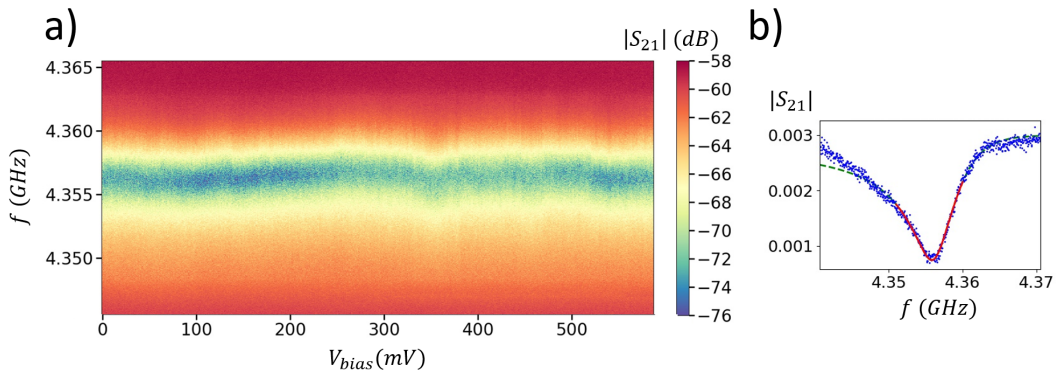


Figure 5.16: (a) Spectroscopy of DC bias sweep on $\gamma - Al_2O_3$ with voltage noise. (b) One example of $|S_{21}|$ from (a) without proper filtering. Voltage noise obscures TLSs within the spectrum and $Q_i = 1600$.

the small $p_z$ TLS distribution. First, we define the small $p_z$ TLSs as the $10^{\text{th}}$ or $20^{\text{th}}$ percentile, which equals 2.8 and 3.5 Debye respectively. The dipole smaller than the above value is multiplied M times in counts for a new distribution. The resulting new average dipole $p_z$ and ratio of small $p_z$ TLS number to the total number are plotted in Fig. 5.15. In an extreme case with 8 missing TLS and 2 fitted TLS with $p_z < 3.5$ D, 4 out of 5 are not analyzed. This also implies multiple factor M = 5 and the new average is at least 3.3 Debye. This is still larger than $\bar{p_z}$ = 2.6 Debye in $\gamma - Al_2O_3$. Now, we turn to the isotropy of dipole orientation. There are missing TLS extractions, especially of those small $p_z$ TLS. The portion of small $p_z$ TLS could be underestimated. As a result, if we add those small $p_z$ back, the material distribution $D(p_z)$ could be monotonic decreasing as expected in the standard model. More studies are needed to understand the small dipole TLSs in the amorphous phase.

### 5.5.7 Effect of less proper filtered bias line

Here, we discuss the effect of bias line filtering and TLS noise on resonator data fittings. Filtering noise in the bias line is essential to study the individual TLSs in both film types. We

performed a control experiment with additional bias-line noise. We start from a setup where the bias line has only a low-pass copper powder filter (CPF) and a 12GHz K&L filter as opposed to the usual situation in which a CPF, a K&L filter, and a RC filter are present (see Chap. 3.1.3 for the bias line setup). Fig. 5.16 (a) shows measurements of $\gamma - Al_2O_3$ TLS spectroscopy with low frequency noise and Fig. 5.16 (b) shows a trace of $|S_{21}|$ at fixed bias. There is no observation of any individual TLS. Surprisingly, the fit gives an internal quality factor, $Q_{i,noise}$ = 1600, which is higher than $Q_i$ = 680 reported before. It is believed that without proper noise filtering, the bias voltage noise strongly affects the visibility of the TLSs.

### 5.5.8 Theoretical models comparison

Ref. [34] suggests that OH bonds are the origin of TLS in AlOx films observed with qubits. Several theoretical simulations point out the possible origins of TLSs in alumina including the calculations based on density-functional theory (DFT) [119–122] and molecular dynamics [123] simulations. Holder *et al.* find that hydrogen aluminum-vacancy TLSs $V_{Al} - H$ in $\alpha - Al_2O_3$ have $p$ = 3.0 D [119]. Separately, Gordon *et al.* simulated the interstitial hydrogen in $\alpha - Al_2O_3$ at various two oxygen(O) atoms distances where $p$ = 2.2 – 2.7 D but a minimum frequency = 16 GHz [120]. Two models related to hydrogen(H) suggest total dipole moment $p < 3.0$ D [119,120].

Besides H-based simulations, two models of O-based TLSs suggest $p > 4.2$ D. DuBois *et al.* studied models of delocalized oxygen atoms with six neighboring aluminum atoms [121,122]. They found oxygen deficient $AlO_x$ for x = 1.25 by varying distances between O and Al atoms, with $p$ = 4.2 - 6.5 D for TLSs with tunneling energy $\Delta_0/h$ = 4 GHz [121]. Additionally, Paz *et al.*find natural bi-stable structures in amorphous alumina including only Al and O atoms and

calculate an average $p$ = 4.2 D from 7 TLSs [123]. Although there are differences between theoretical models, they are consistent in that H-TLSs have smaller $p$ than O-TLSs.

The $\gamma - \mathrm{Al_2O_3}$ $D(p_z)$ has a single peak at approximately $p_z$ = 2.6 D, which can be sourced from H-TLS or two unresolved peaks of both H- and O-TLSs. Although small in statistics, $\mathrm{a - AlO_x}$ has a wider spread in $D(p_z)$ and two separate peaks. Furthermore, $\mathrm{a - AlO_x}$ TLSs have 10 % population with $p_z > 8.6$ D, where $p_z$ = 8.6 D is the maximum in $\gamma - \mathrm{Al_2O_3}$. Using a comparison between two alumina datasets and the fact that O-based TLS is the larger dipole in DFT structures, we find a higher ratio of O-TLSs to H-TLSs in a-AlOx than $\gamma - \mathrm{Al_2O_3}$.

## 5.6 Conclusion

In summary, we have extracted the dipole moment $p_z$ of hundreds of individual TLSs in nanoscale-thick films of (polycrystalline) $\gamma - \mathrm{Al_2O_3}$ and (amorphous) $\mathrm{a - AlO_x}$ alumina. We have used an Electrical-Bridge Quantum Defect Sensor (EBQuDS) and show it is suitable to characterize a number of TLSs as quantum defects. Analysis of the measured histogram of $p_z$ reveals that polycrystalline alumina fits well to a single Gaussian peak. From the material distribution (algebraically related to the measured one), we obtain that the mean TLS moment of the polycrystalline film is $p_z$ =2.6$\pm$0.3 D (= 0.54$\pm$0.05 e$\mathring{A}$) and $\sigma$ = 1.6$\pm$0.2 D (= 0.33$\pm$0.03 e$\mathring{A}$). Furthermore, the material distribution disagrees with the isotropic model commonly used in amorphous materials, indicative of a preferred texture (orientation) of the polycrystalline grains that host TLSs or a modified model. On the other hand, we cannot conclude if amorphous alumina dipoles are isotropic or not because of missing TLS extraction.

The ability to extract an accurate mean $p_z$ puts constraints on its defect type and allows us

to make first comparisons to new microscopic structures used in DFT calculations. The polycrystalline data show one dominant peak and could be showing the dominance of H-TLSs, or unresolved peaks of both H- and O-TLSs in the distribution. We find that $\mathrm{a}-\mathrm{AlO_x}$ has a larger mean $p_z$ = 4.6$\pm$0.5 D, which is consistent with previous amorphous alumina results. In contrast to $\gamma-\mathrm{Al_2O_3}$, the TLSs switch more rapidly, and our $p_z$ distribution in amorphous alumina yields a larger standard deviation (= 2.5$\pm$0.3 D) and two peaks in contrast to one. The moments above 8.6 D (10% of the distribution) are larger than any TLS in polycrystalline alumina and agree only with calculations of delocalized O atoms. Due to this and other amorphous distribution features, we find that the ratio of O- to H-TLSs is higher in amorphous samples than in the polycrystalline ones. Because of its relative simplicity in distribution, alumina seems to be an important material for further JJ-barrier studies.

# Chapter 6: Surface TLSs Investigation by Vacuum-Gap Resonators

## 6.1 Motivation

To begin with, I would like to recall Chap. 2.3, where the standard tunneling model and the puzzle of saturation slope correction $\phi$ are introduced. However, I will replace Rabi frequency $\Omega$ by photon number $n_{ph}$ since $n_{ph}$ is a direct measuring parameter. Also, the direction of the ac zero-point electric field $\boldsymbol{E}_{\mathrm{zp}}$ depends on the position and is typically unknown in planar resonators (so as $\Omega$). It is useful to have $\boldsymbol{p}$ as a vector of dipole moment and $p = |\boldsymbol{p}|$.

Measuring the loss (inverse quality factor $1/Q_i$) of a resonator as a function of photon number $n_{ph}$ provides information on TLSs. According to the STM with steady TLS frequencies [76, 77], the loss from TLSs gives

$$\frac{1}{Q_i} = \frac{1}{Q_i^0} \frac{\tanh(\frac{\hbar\omega}{2k_BT})}{\sqrt{1 + n_{ph}/n_c}}. \tag{6.1}$$

This is written in terms of the intrinsic loss $1/Q_i^0$, the resonator frequency $\omega$, temperature $T$, and TLS coherent time $\tau = 1/\Gamma_2$. Note that $n_c^{-1} \propto (\boldsymbol{p} \cdot \boldsymbol{E}_{\mathrm{zp}})^2 \tau$ depends not on $\Gamma_1$, since $\Gamma_1$ is only related to the phonon coupling [76]. Recent measurements of resonators with deposited films support the saturation power law with an exponent of 0.5, $Q_i \propto n_{ph}^{0.5}$, above $n_c$ [34, 134–136]. However, planar resonators with only oxide interfaces and processing residues have a

small saturation exponent $\ll 0.5$. A phenomenological approach uses a free fitting parameter $\phi \ll 0.5$ with the denominator part in Eq. 6.1 set as $(1 + n_{ph}/n_c)^{\phi}$ for matching the experimental data [38, 90–93].

A physical mechanism for small $\phi$ may come from the non-negligible interactions between TLSs. The concept is that frequencies of coherent TLS (cTLS) defined by $\hbar\omega \gg k_B T$ would depend on the states of neighboring low-frequency (LF) TLSs with $\hbar\omega \leq k_B T$. Thus, stronger fields are required to saturate TLSs than if their frequencies were fixed as suggested by STM. The stochastic fluctuations yield a logarithmic equation 2.85 which is used for the fits in the results from planar resonators [92, 93]. However, planar resonators have position-dependent field distribution of $E_{zp}$ [94], and dielectric films may exhibit a wide spread of $p$ [95, 103, 131], resulting in a distribution of $n_c$. In consequence, Eq. 6.1 which has a single value $n_c$ is forced to be rectified to Eqs. 2.88 or 2.87.

Vacuum-gap capacitors (VGCs) or 3D cavities are two types of resonators to study TLS loss solely from metal surface. VGCs can provide a small on-chip footprint of capacitance and still maintain high quality for both micro- and mechanical wave resonators [137–139]. 3D cavities show extremely high quality factor and are used widely to couple to transmon qubits [70]. However, 3D cavities still have a distribution of $\boldsymbol{E}_{\mathrm{zp}}$. Here we choose VGC in resonators, where the metal-air (MA) interface (i.e., $\mathrm{AlO_x}$) is the dominant TLS host material. A quasi-uniform gap distance yields $\boldsymbol{E}_{\mathrm{zp}} \approx \sqrt{\hbar\omega_c/2Cd^2}\hat{z}$, where $\hat{z}$ is the direction of two plates separated by $d$ and $C$ is the total capacitance of the resonator. As a result, we are enabled to investigate MA TLSs and verify the correct explanation.

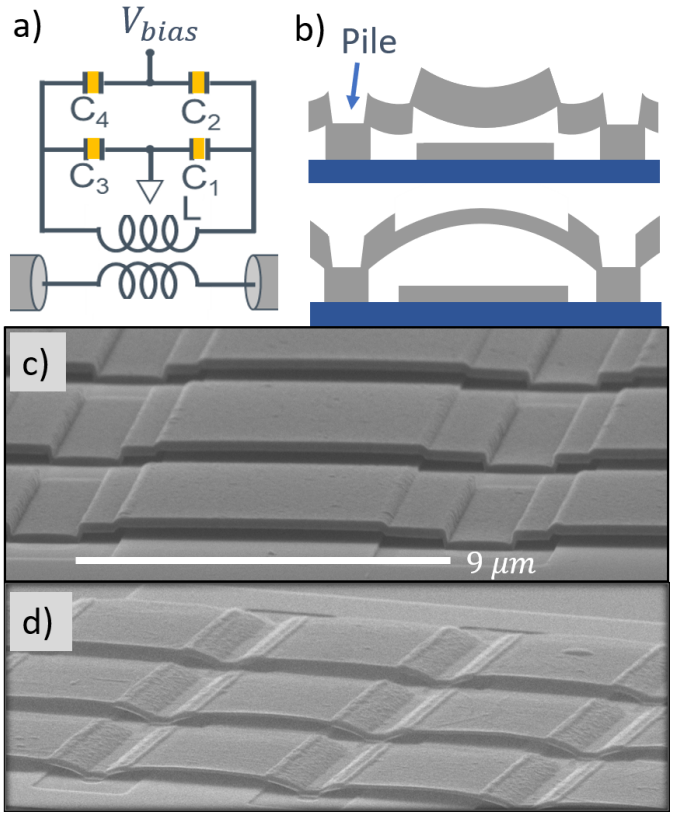


Figure 6.1: Schematic, side-views and scanning electron micrographs of vacuum gap capacitors (VGCs). Vacuum-gap resonators are primarily sensitive to metal-air (MA) interface TLSs. (a) Schematic of the resonators. (b) Side-view illustrations of the VGCs using SiNx (top) and photoresist (bottom) as sacrificial layers. The shape of top electrode depends on the sacrificial layers (see main text). (c) VGCs with SiNx as the sacrificial layer, which yields a terraced bridge shape with an average gap distance $\bar{d} \approx 125$ nm. (d) VGCs with photoresist as the sacrificial layer, which yields an arch shape and $\bar{d} \approx 250$ nm. The process uses a 200 nm metal-thinning step before removal of the sacrificial layer .

## 6.2 Fabrication Method

The schematic of the resonators follows the Ref. [95, 131] and is shown in Fig. 6.1 (a). VGCs are achieved with a standard optical lithography process; two kinds of sacrificial layers (SLs) are used, which are low stress SiNx and photoresist (PR). The capacitors are comprised of perpendicular strips with widths of 6 and 13 $\mu$m. After releasing the SL, the top electrode strip shape ensures a quasi-uniform gap distance. At the start of the fabrication, the bottom

electrode and the ground plane are made from 120 nm-thick aluminum film deposited by e-beam evaporation to ensure a small stress film. Next, we deposit the SL and name the resonators SiNx VGC and PR VGC depending on the use of the SL. For SiNx VGCs, we grow 200 nm-thick SiNx in an Oxford PECVD system at 300°C and spin PR to pattern the structures of the connection via-holes and bridge supports. Later, we etch the patterns by $SF_6$ reactive-ion etching (RIE) plasma. For PR VGCs, we spin S1805 positive PR at 500 nm thickness. The wafer is exposed to the pattern of via and bridges and then developed by Microposit MF-CD-26. We reduce the PR thickness from 500 to 200 nm by a timed RIE oxygen plasma descum and then bake it at 170°C to strengthen the PR. A top Al layer of 300 nm is deposited by e-beam evaporation and patterned to form the top electrode plate. We choose 300 nm-thick Al in order to fill vias and strengthen the base piles for the top electrodes. Side-view illustrations of two VGCs are shown in Fig. 6.1 (b). The illustration of the fabrication can be found in Appendix A.

An additional thinning process is made by etching 100 $\sim$ 200 nm of the top electrode to prevent the bridge from collapsing. The thinning process reduces the beam mass/thickness which changes the strain from compressive to tensile. We show a SiNx VGC without thinning process in Fig. 6.1 (c) and PR VGC with 200 nm thinning in Fig. 6.1 (d). This step is essential for PR VGCs or both types of VGC with support base piles having large separations. The separation of piles is chosen as 9 $\mu$m in the final devices, and a separation $>$ 15 $\mu$m always collapsed after releasing.

Next, the wafers are diced into 6.5 X 6.5 $mm^2$ chips and the SL is ready to be released. For PR VGC, the chips are immersed in 80 °C NMP for 3 hours, rinsed with IPA, and blown dry by nitrogen. For SiNx VGC, the chips are placed under a high power inductively coupled $SF_6$ plasma without forward voltage, which has a lateral etch rate around 4 $\mu$m per hour. Finally, we measure

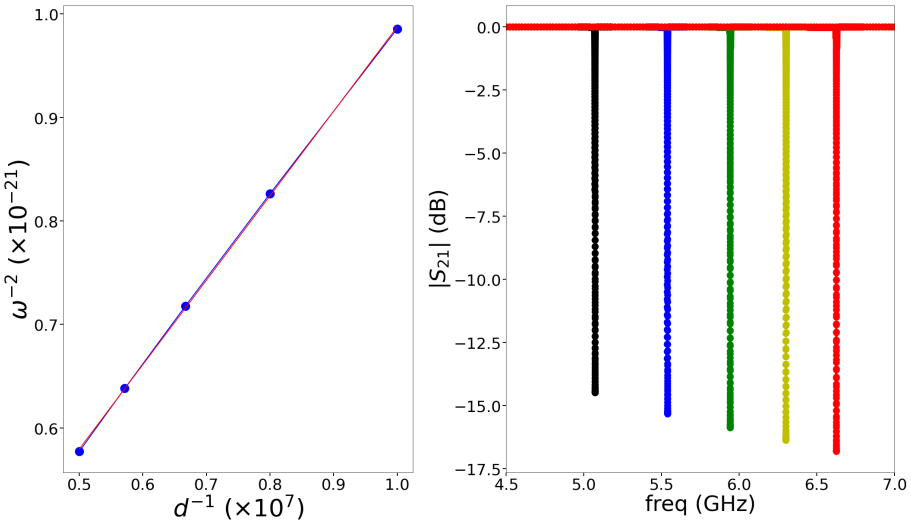


Figure 6.2: Left: Simulated resonant frequency $\omega$ vs vacuum-gap distance $d$. From the intersection, we can estimate the stray capacitor. Right: Simulated $|S_{21}|$ vs $d$.

the resistivity from the bias port of the resonators and the ground to confirm a non-collapse VGC, where the yield is more than 95%.

The gap distance $d$ depends on the choice of the SL and the thinning process. We expect the curvature or $d$ would change during cooling from room temperature to mK. However, this affect would be small and in fact all non-collapsed VGCs did survive cooling to cryogenic temperatures. The gap $d$ is estimated by comparing the measured resonant frequency to that of the finite-element microwave simulation in Sonnet at different $d$ (see Fig. 6.2). From resonance frequency and distance plotted as $\omega^{-2}$ versus $1/d$, we estimate the stray capacitor $C_{stray} \approx 25$ fF, which is primarily coming from the self-capacitance of meander inductance and is expected to have a high quality factor. Since the VGC ($d$ = 125 nm) has capacitance $\approx$ 150 fF, we expect the dominating TLS effect is from the MA interface of the VGC.

We find that $d$ of all four resonators on the same chip have the same value. However, because of the strain, the top electrode-bridges are never precisely parallel to the bottom electrodes (see Fig. 6.1 (b)) but also has $d$ of the coefficient of variation $< 15\%$. From the simulation,

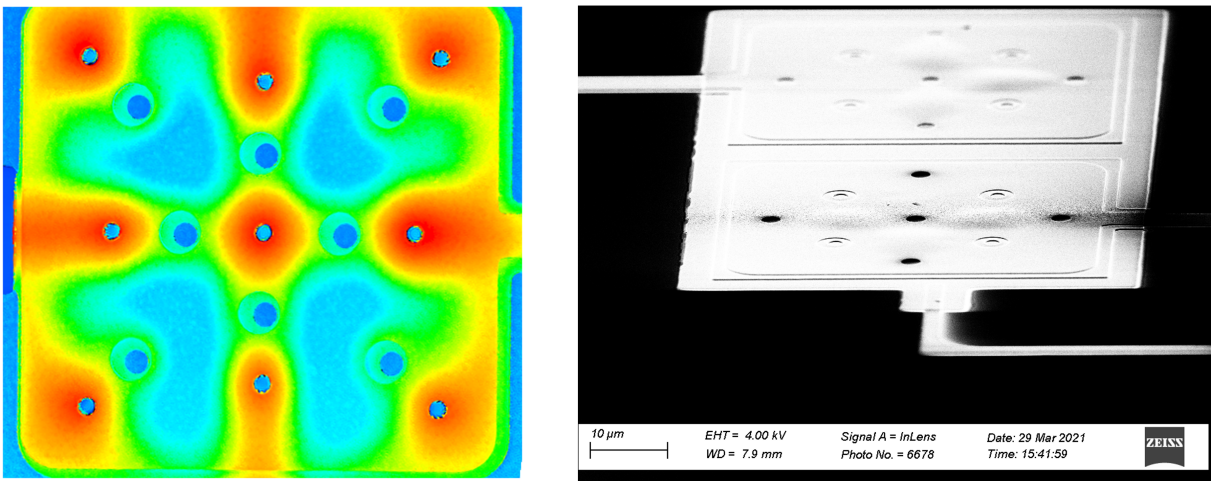


Figure 6.3: Left: Height measurement done by a laser confocal microscope. The red means a higher position. Right: SEM image. A clear non-uniform top plates are seen.

we found that the average gap distance $\bar{d}$ from SiNx VGCs is 125 nm for no-thinning process (Fig. 6.1 (c)), 135 nm for a 100 nm thinning process, and 150 nm for a 200 nm thinning process. The filling factor of MA interface $F_{r,MA}$ are 0.9%, 0.8%, and 0.7% ,respectively. Moreover, $F_r$ of other interfaces are at least a factor of 10 smaller than than a comparable coplanar resonator which could have been used in a surface TLS study [87]. While PR VGCs in Fig. 6.1 (d) have $\bar{d}$ = 225 nm and $F_{r,MA} < 0.45\%$, which is smaller than our other resonators, it should have more contributions to interfaces other than MA relative to SiNx VGCs. Since the MA surface loss dominates, the surface loss tangent is $\tan\delta_{MA} = (Q_i\, F_{r,MA})^{-1}$.

### 6.2.1 Unoptimized fabrication process

The original design version is shown in Fig. 6.3 which is followed Ref. [137, 138]. The top electrode plate is chosen to be a continuous piece which needs several supporting poles to hold the plate not collapsing and releasing holes to speed up the lateral etching of the SL. This kind of design offers a small footprint. However, the top plates are never flat due to local strain. The left

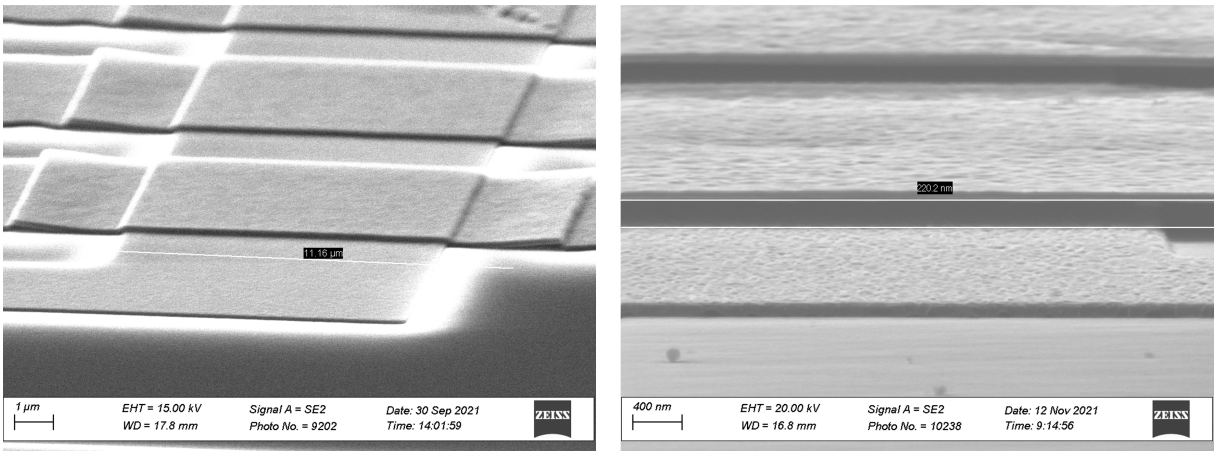


Figure 6.4: Unoptimized SiNx VGC. Left: 100-nm top Al layer resulting in collapsed bridge. Right: Over-etched top Al resulting in non-uniform gap distance.

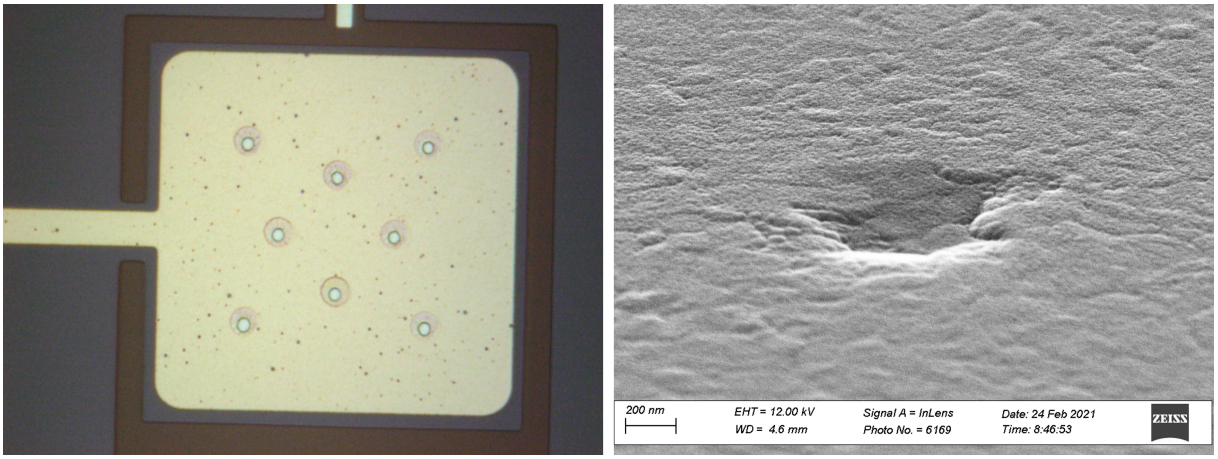


Figure 6.5: Sputtered Al as the bottom layer. Dents are generated after post-annealing to 300 °C during SiNx deposition. Left: microscopy image. Right: SEM image

of Fig. 6.3 is the height measurement done by a laser confocal microscope, where one can see that the plate near releasing holes (smaller circles) is bowing up ($d > \bar{d}$) and the plate between supporting poles (larger circles) is bending down. I show a SEM image on the right.

Fig. 6.4 shows the unoptimized fabrication of SiNx VGC. On the left, collapsed bridges are observed due to the 100-nm top Al deposition. It indicates a thicker top layer is necessary. On the right, the top layer is over-etched from the original thickness of 300 nm to the final thickness of $\sim$ 60 nm. The local strain pulls the bridge non-uniformly resulting a non-uniform $d$.

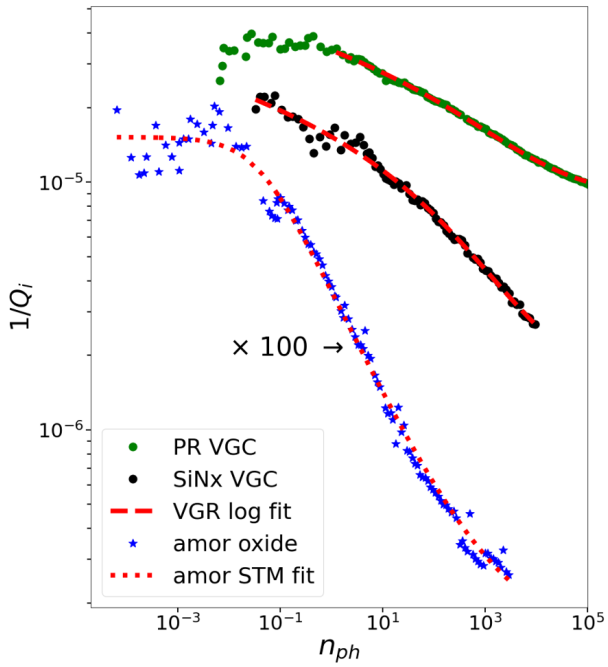


Figure 6.6: Intrinsic loss $Q_i^{-1}$ vs. average photon number $n_{ph}$. The resonator results of a photoresist (PR) VGC, a SiNx VGC, and a bulk amorphous $AlO_x$ sample are displayed from top to bottom, where the $AlO_x$ loss is shown after dividing by 100. For the amorphous sample (blue), the saturation slope follows the standard tunneling model (STM) and the fit to Eq. 2.84, with the expected exponent of $\phi = 0.50$. However, the VGC results are consistent with the fast switching (FS) model which yields a logarithmic Eq. 2.85.

We choose e-beam evaporated Al as the bottom layer due to the dents observed after we anneal sputtered Al at 300 °C. Dents have dimensions about 200 nm which prevents us to have a uniform gap distance (see Fig. 6.5). This phenomenon is only seen in sputtered Al which we suspect the reason is because of less dense Al deposited by Ar ion than by e-beam.

## 6.3 Verification of the correct model

### 6.3.1 Power dependent loss tangent

The microwave setup is given in Ref. [95], and has a strongly attenuated input line and a low-pass filtered bias line. Each chip contains four resonators and six chips are measured (4 for

SiNx VGC and 2 for PR VGC). All resonators except one that may have a collapsed capacitor, worked with repeatable resonant frequency between cooldowns. A high internal quality factor in single photon regime $Q_i^0 \geq$ 60k is found in SiNx VGC regardless of the thinning process. $Q_i^0 \geq$ 20k in PR VGC is generally lower possibly due to the ICP dry-etching thinning process causing extra residues. A control group of coplanar waveguide resonators fabricated in parallel with the VGC fabrication process shows $Q_i^0 >$ 0.5M, independent of the choice of SLs. We would, therefore, expect the loss from $C_{stray}$ is $\frac{1}{Q_{i,stray}} \sim 2 \times 10^{-7}$ which is much smaller than $F_{r,MA} \tan\delta_{MA} \sim 10^{-5}$. Another reference sample is the bulk amorphous $\mathrm{AlO_x}$ films studied in Ref. [95] for comparing TLSs in surface and in bulk. Since SiNx VGCs have a better $Q_i^0$, we focus on them below.

Due to the unstable TLS frequencies, $Q_i$ fluctuates over time. Therefore, each $Q_i(n_{ph})$ in Fig. 6.6 is an average value from 10 acquisitions of transmission $S_{21}$ and the separation time of two acquisition approximates to 1.5 hours. Weak $n_{ph}$ dependent losses of a SiNx VGC (black) and a PR VGC (green) are found in all VGCs. Their traces fit well to the logarithmic Eq. 2.85 derived from the FS model as shown in red dashed line. From the fit, we obtain $\gamma_{max}$ = $2\pi \cdot 5.7$ MHz and $\gamma_{min}$ = $2\pi \cdot 20$ kHz using $p$ = 1.5 (Debye) which is extracted later in Fig. 6.8 (c). We obtain $F_{r,MA} P_r \tan\delta^0 \ln(C_1) < 4 \times 10^{-7}$ indicating the $n_{ph}$-independent loss is trivial and not affecting the accuracy of the fitting. In contrast, for the bulk $\mathrm{AlO_x}$, we find a good fit to Eq. 6.1 shown in Fig. 6.6 (a) in blue dots. Despite the fact that we observe spectral diffusion and jitters in individual TLS frequencies, the mutual TLS interaction in bulk $\mathrm{AlO_x}$ is still insignificant, which is consistent with STM. The larger $\gamma$ in MA TLSs is possibly due to a larger LF TLS density than that in $\mathrm{AlO_x}$.

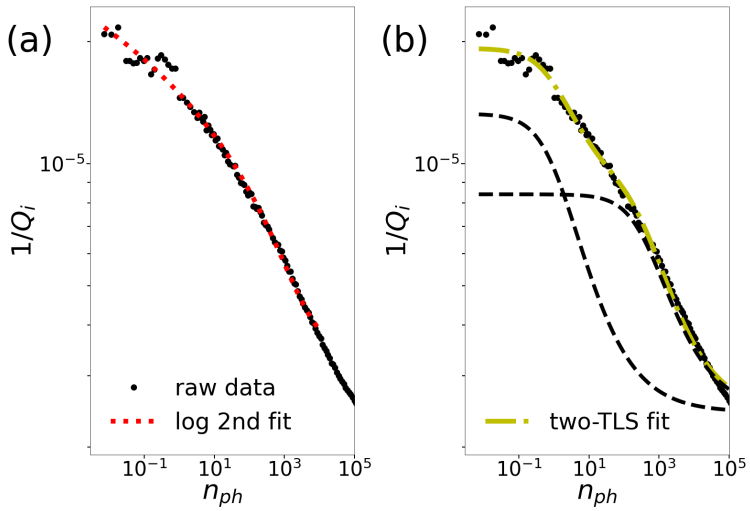


Figure 6.7: $1/Q_i$ vs. $n_{ph}$ for two different fitting equations. (a) Fit to Eq. 2.86 using $p = 1.5$ Debye as given in Fig. 6.8 (c). The fit yields the geometric average $\sqrt{\gamma_{max}\Gamma_2} = 2\pi\cdot$ 14MHz. (b) Fit to Eq. 6.2. We obtain the fitting parameters of $F_{r,1}\tan\delta_1^0 = 1.1\times10^{-5}$, $F_{r,2}\tan\delta_2^0 = 6.0\times10^{-6}$, $n_{c,1}$ = 0.9, and $n_{c,2}$ = 320. The two dashed guidelines represent the contributions from each TLS contribution. However, from Fig. 6.6 (d), we exclude the possibility that Eq. 6.2 is the correct equation (see the main text).

### 6.3.2 Alternative models for $Q_i(n_{ph})$ fit

Here, I will show the fits to the MC model and the second logarithmic equation from Ref. [85]. The fit to Eq. 2.86, which satisfies the different condition than Eq. 2.85, is shown in Fig. 6.7 (a). We extract the geometric average $\sqrt{\gamma_{max}\Gamma_2} = 2\pi\cdot14$ MHz, which is much larger than $\Omega$ of the fitting range. Since we do not know the exact value of $\Gamma_2$, we prefer Eq. 2.85 in this chapter.

On the other hand, the MC model is given by Eq. 2.87 with $i$ = 1 to N, while an more accurate integral form is Eq. 2.88 and can be also found in Ref. [136, 140]. Here, we consider the case of two contributions ($i$ = 1, 2), giving

$$\tan\delta(n_{ph}) = \frac{F_{r,1}\,\tan\delta_1^0}{\sqrt{1+\frac{n_{ph}}{n_{c,1}}}} + \frac{F_{r,2}\,\tan\delta_2^0}{\sqrt{1+\frac{n_{ph}}{n_{c,2}}}} + C_0. \tag{6.2}$$

From the fit in Fig. 6.7 (b), we obtain $F_{r1}\tan\delta_1^0 = 1.1\times10^{-5}$, $F_{r2}\tan\delta_2^0 = 6.0\times10^{-6}$, $n_{c,1}$ = 0.9, and $n_{c,2}$ = 320. Two guidelines showed two separate square root dependent $Q_i$. $n_{c,i}^{-1} \propto (p_i E_{\mathrm{zp}})^2\tau$, where $p_i$ is dipole moment of i-th group. The fit yield $\frac{n_{c,2}}{n_{c,1}} \approx 320$, which is valid only if there are two types of TLSs. However, the validity is negated by the results of two-tone spectroscopy, where we observe weak power dependent TLS Rabi frequency.

### 6.3.3 Experimental two-tone spectroscopy

To further understand these MA TLSs, we perform a two-tone technique where the second tone saturates TLSs at frequency $\omega_p$ [88, 89]. From our results of the two-tone spectroscopy, we find that a similar phenomenological exponent $\phi$ is needed to fit the data ($n_{pu}^{0.5} \rightarrow n_{pu}^{\phi}$) and

$$\hbar\Omega_0 = 2\langle|\boldsymbol{p}\cdot\hat{z}|\rangle|\boldsymbol{E}_{\mathrm{zp}}|\, n_{pu}^{\phi}. \tag{6.3}$$

See Chapt. 2.2.5 for the theoretical derivation of frequency and quality factor shifts.

First, we show $\Delta\omega$ vs. $\Delta\omega_p$ (Fig. 6.8a) and $1/Q_i'$ vs. $\Delta\omega_p$ (Fig. 6.8b) at a fixed $P_{in} \approx$ -105.5 dBm. The red curves are the simultaneous least-squares fit of both $\Delta\omega$ and $Q_i'$ to Eq. 2.81 and Eq. 2.82. For the fit, we obtain $\phi$ = 0.3 and $\Omega_{max} = \Omega_0(\Delta\omega_p = 0) = 2\pi\cdot$1.7MHz, which is also the maximum of Rabi frequency at $\Delta\omega_p = 0$ and at a fixed $P_{in}$. We plot $\Omega_{max}$ vs. $P_{in}$ in Fig. 6.8 (c), which leads to $\phi$ = 0.27, which is consistent the fact that $\phi < 0.5$. Similarly, we measure the $1/Q_i'$ and $\Delta\omega$ vs $n_{pu}$ at a fixed $\Delta\omega_p = 2\pi\cdot$1.5 MHz, and the fit yields $\phi = 0.3$ in Fig. 6.8 (d). In the fitting process, $\kappa_{tot}$ is chosen as a constant = $2\pi\cdot 280$ kHz, although $\kappa_{tot}$ is dependent on $Q_i'$, which in-turn depends on $\Delta\omega_p$. We find only a slight sensitivity of the extracted $\Omega_{max}$ depending on if $\kappa_{tot}$ is a constant or varying value in the next Chapter 6.3.4. Lastly, from

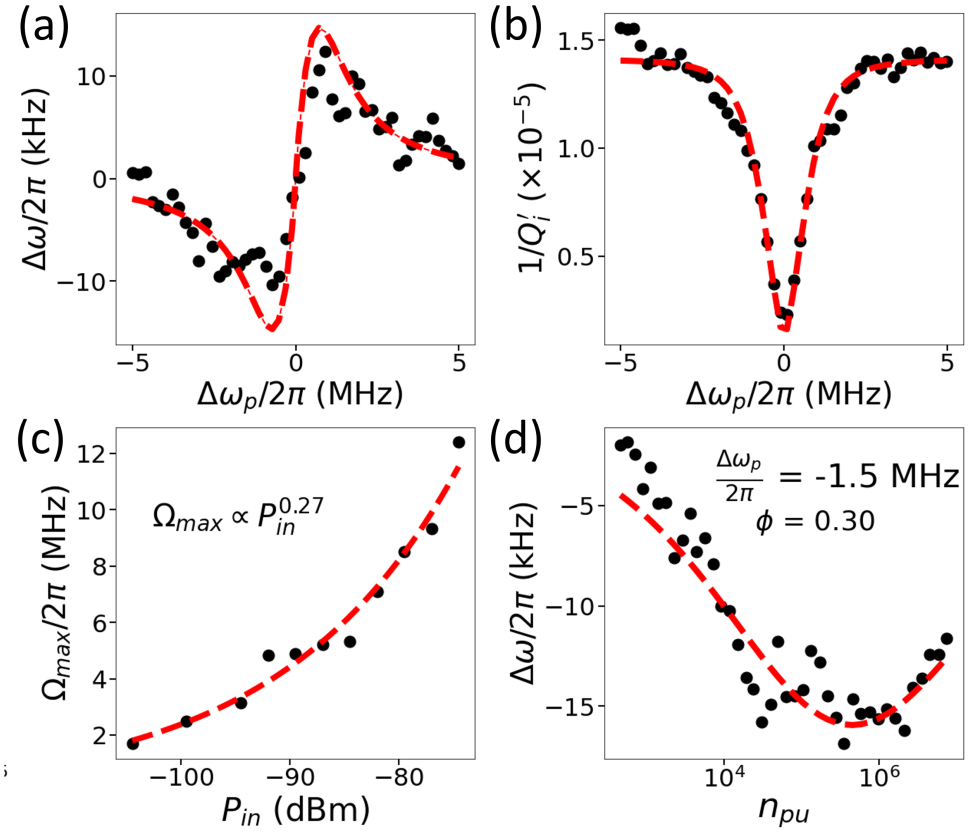


Figure 6.8: (a-d) Two-tone spectroscopy with a pumping tone frequency $\omega_p$, and a probing tone around the original resonant frequency $\omega_c$. (a) Resonant frequency shift $\Delta\omega = \omega' - \omega_c$ vs. pumping tone detuning $\Delta\omega_p = \omega_p - \omega_c$. (b) $Q_i^{-1}$ vs. $\Delta\omega_p$. Panel (a) and (b) show the two-tone data from the SiNx VGC at a fixed input power $P_{in} \approx$ -105.5 dBm. The red curves are the simultaneous least-squares fit of both $\Delta\omega$ and $Q_i$ to Eq. 2.81 and Eq. 2.82 except for a replacement of $n_{pu}^{0.5} \rightarrow n_{pu}^{\phi}$, where $\phi$ allows a deviation from the STM. For the fit, we obtain the maximum Rabi frequency of TLSs $\Omega_{max} = 2\pi\cdot$1.7MHz. (c) $\Omega_{max}$ vs. $P_{in}$. We find $\Omega_{max} \propto P_{in}^{0.27}$, where the exponent is $< 0.5$ against the multi-contribution STM model which takes diverse $p$ and $E_{\mathrm{ZPF}}$ distributions into account. (d) $\Delta\omega$ vs. $n_{pu}$ for a fixed $\Delta\omega_p = -2\pi\cdot$1.5 MHz. The fit resolves $\phi = 0.30$ consistently.

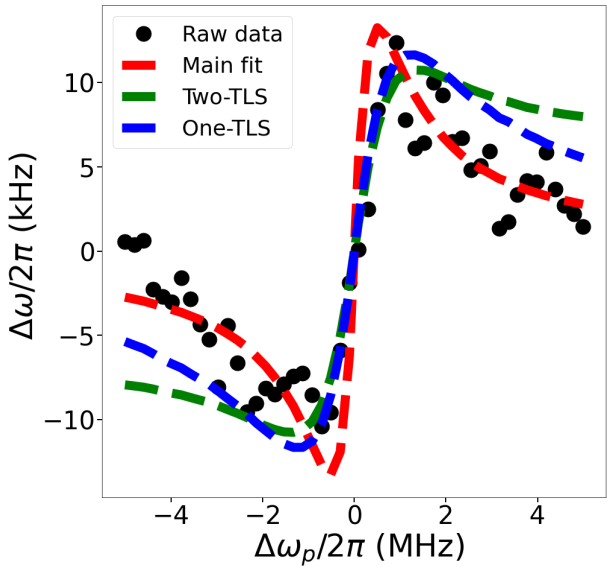


Figure 6.9: Two tone spectroscopy, $\Delta\omega$ vs. $\Delta\omega_p$, using different models to fit. The black dots as raw data and the red curve are the same as in Fig. 6.8 (a). The blue and green curves are based on $\Omega_0 \propto \sqrt{n_{pu}}$ with one and two groups of TLSs, respectively. We find that only a weak power dependence $\Omega_0$ can explain the behavior of $\Delta\omega$ while increasing $\Delta\omega_p$.

Eq. 2.83 and 6.3, we extract $p$ = 1.5 $\pm$ 0.2 Debye = 0.3 $\pm$ 0.02 e$\mathring{A}$ by considering isotropic $\boldsymbol{p}$, $\langle|\boldsymbol{p}\cdot\hat{z}|\rangle = p/\sqrt{3}$ [86].

In Fig. 6.8, we substitute $n_{ph}^{0.5} \rightarrow n_{ph}^{\phi}$ with $\phi < 0.5$ for all equations derived from the STM including Eqs. 2.84, 2.81, 2.82, and 6.3. A comparison using the MC model is shown in Fig. 6.9, where we observe that the fit of Eq. 6.3 with $\phi$ = 0.3 (red) is the better fitting function than Eq. 6.3 with $\phi$ = 0.5 (blue). Even assuming two TLS groups with $p_1 = \sqrt{320}p_2$ (and $\phi$ = 0.5) as shown in green, the fit of $\Delta\omega$ is not matching the raw data in black when $\Delta\omega_p$ increases. Therefore, it is more likely that only one group of $p$ exists. Additionally, TLS density distributing as $1/\tau$ [125] but not as $p$ still gives $\phi = 0.5$, we rule out MC model and find the FS model qualitatively consistent. For comparison, our two-tone spectroscopy is consistent with Ref. [141], where they resolved $\phi$ = 0.28 $\sim$ 0.3 in a surface acoustic wave resonator with the same method of Fig. 6.8 (c).

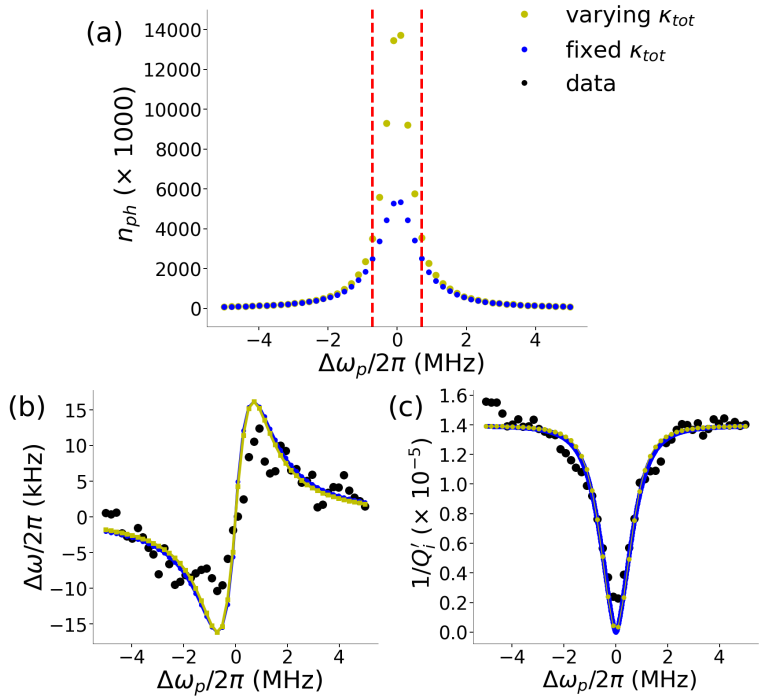


Figure 6.10: The minor effect of $\Delta\omega_p$-dependent $n_{pu}$ at a fixed input power ≈ -105.5 dBm. The data set is from Fig. 6.8 (a) and (b). Panel (a): $n_{pu}$ vs. the pump tone detuning $\Delta\omega_p$. Varying TLS saturation tone $\Delta\omega_p$, $\kappa_{tot}$ is not a fixed value due to the change of $Q_i$. It is expected that when $\Delta\omega_p$ is close to 0, there is a decrease of $\kappa_{tot}$ since $Q_i$ increases. We plot $n_{pu}$ with a fixed $\kappa_{tot}$ by $Q_i(n_{pu}) \rightarrow Q_i^0$ in blue comparing to $n_{pu}$ with a varying $\kappa_{tot}$ in yellow as a function of $\Delta\omega_p$. The two red dashed lines represent $\Delta\omega_p$ which has the maximum $|\Delta\omega|$. Panel (b) and (c): The effect of a fixed or varying $\kappa_{tot}$ in $\Delta\omega$ vs. $\Delta\omega_p$ and $1/Q_i'$ vs. $\Delta\omega_p$. The raw data is in black. We observe little influence using a fixed or varying $\kappa_{tot}$ for extracting $\Omega_{max}$.

### 6.3.4 Nonlinearity of $n_{pu}$ and $\Omega_{max}$ in two-tone spectroscopy

This resonator has external quality factor $Q_e \approx$ 25k and $Q_i^0 \approx$ 60k. When we measure the two-tone spectroscopy, the nonlinear $n_{ph}$ as a function of $\Delta\omega_p$ would affect the accuracy of extracting $\Omega_{max}$. While using the equation Eq. 2.81 and Eq. 2.82 to fit the data of Fig. 6.8 (a) and (b), we automatically assume $\kappa_{tot}$ is a constant and independent of $\Delta\omega_p$ by $Q_i(n_{pu}) \rightarrow Q_i^0$. However, in Fig. 6.10 (a), we also show how $n_{ph}$ would have changed in analysis if we had allow $k_{tot}$ to be a fit parameter. Two vertical lines represent the maximum shift $|\Delta\omega_p|_{max}$ in Fig. 6.8 (a). In Fig. 6.10 (b) and (c), we recalculated $\Delta\omega$ and $1/Q_i'$ considering the difference of $n_{ph}$ using a

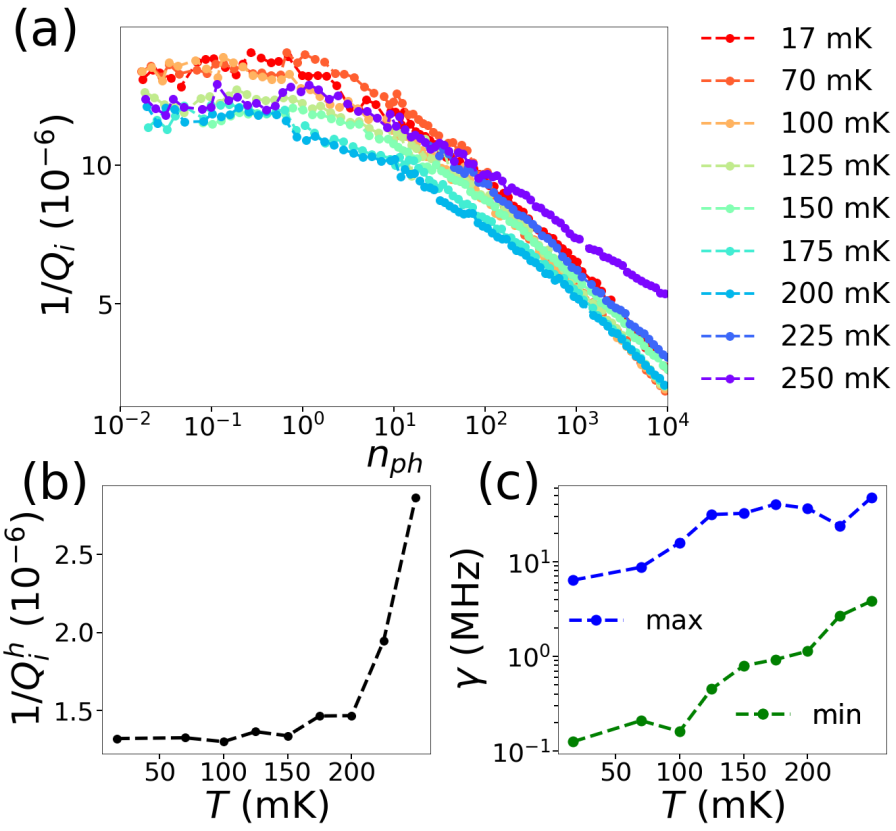


Figure 6.11: (a) $1/Q_i$ vs. $n_{ph}$ from a SiNx VGC at different temperatures. The exponent of $Q_i^{-1}(n_{ph})$ or $\phi$ is slightly decreasing while temperature increase. (b) The loss at high power $1/Q_i^h = 1/Q_i(n_{ph} = 10^5)$ is relatively constant for low temperature $< 200$ mK and it increases due to thermally generated quasiparticles at high temperatures. (c) Fitted maximum and minimum jitter rate $\gamma_{max,min}$ increase with temperature. This is expected since $\gamma$ is affected by the the number of low-frequency (LF) TLSs.

fixed $\kappa_{tot}$ or a varying $\kappa_{tot}(\Delta\omega_p)$. The difference is small and the inaccuracy of $\Omega_{max}$ is limited by the accuracy of $n_{ph}$ and $\Delta\omega$, which depend on the input-line calibration and the extraction of $\omega_c'$, respectively.

### 6.3.5 TLS properties with temperature effect

We next probe the temperature effect on dependence of MA TLSs. In Fig. 6.11 (a), we show the $1/Q_i$ vs. $n_{ph}$ for different temperatures $T$ from 17 to 250 mK. From the fits of Eq. 2.85, we obtain the loss tangent background $C_0 < 2\times10^{-7}$ and $\tan\delta^0$ is roughly the same for $T \leq 200$

mK. In Fig. 6.11 (b), we plot high power loss $1/Q_i^h$ vs. $T$ at a large $n_{ph}$ = $10^5$ and observe a rising $1/Q_i^h$ from quasiparticles only when $T > 200$ mK. We also observe that both extracted $\gamma_{max}$ and $\gamma_{min}$ increased with $T$, as shown in Fig. 6.11 (c). This qualitatively agrees with expectations of the increasing LF TLSs density.

According to Ref. [142], cTLSs' decoherence rate $\Gamma_2 \propto T^{1+\mu}$ depends on the number of coupled LF TLSs. Here, $\mu$ describes a non-uniform TLS asymmetry energy $\Delta$ density: $P(\Delta) \propto \Delta^{\mu}$. This density of states dependence is introduced phenomenologically, and is stronger than the expected dipolar gap from TLS-TLS dipolar interactions [97]. Additionally, previous measurements [93] of 1/f resonant frequency noise induced by cTLSs show that the noise $\propto \Gamma_2^2/T = T^{1+2\mu}$ with $\mu$ = 0.3. To study $\Gamma_2$ of MA TLSs, we perform a transmission $S_{21}$ measurement on resonance at various temperatures and display power spectral density (PSD) of the phase $\theta$. $\theta$ is defined as the angle of the vector of the off-resonant point (1,0) to $S_{21}$ data and the x-axis (see inset of Fig. 6.12 (a)). The PSD of the fluctuations in the phase angle, $\delta\theta$, provides the information of the fluctuations in the resonator frequency [86]. One PSD of $\delta\theta$ dataset is plotted in the lower trace of panel (a). We fit the PSD to a function combining 1/f, Lorentz and white noise: $A/f^{\alpha} + B\tau/(1+(2\pi f\tau)^2) + C$. The Lorentz noise indicates single or few coupled cTLSs with $\tau \approx 3$ sec, and the 1/f noise ($\alpha \approx 1$) is from weak coupled TLSs [40, 143]. Guidelines show the Lorentz noise and 1/f noise separately in dashed lines. In Fig. 6.12 (b), we show $\delta\theta$ vs. time (blue) and a Gaussian function filtered data in time domain (red). We observe both telegraphic noise and spectral diffusion are affecting the resonance. We realize the noise spectrum is also fluctuating with time (the same phenomenon in $Q_i$). In some data, the Lorentz noise does not show up and is covered under 1/f noise. Therefore, the noise is analyzed by averaging 8 consecutive measurement, and the average PSD is shown in the upper trace in Fig. 6.12

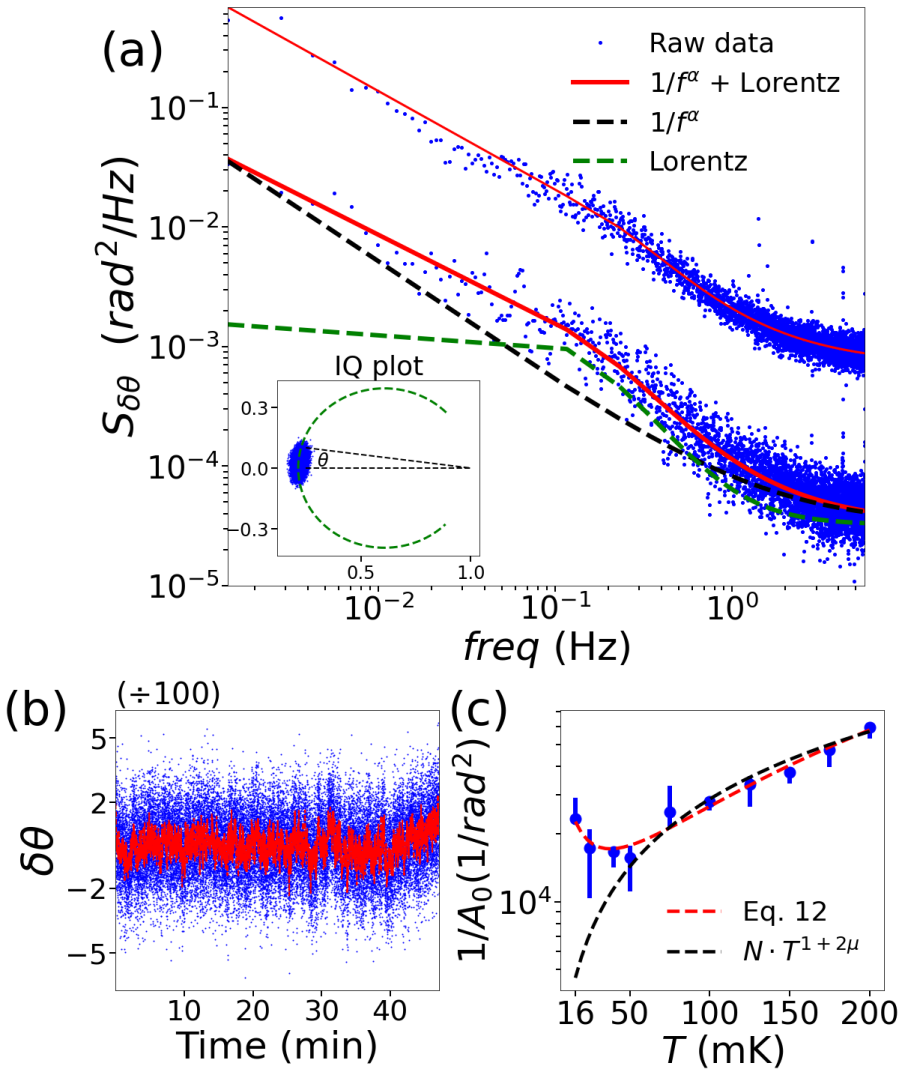


Figure 6.12: (a) Power spectral density (PSD) of phase angle $\delta\theta = \theta - \bar{\theta}$. Here, $\theta$ is the angle defined in the inset and described in the main text. $\bar{\theta}$ is the mean value of $\theta$. The bottom data is a 50 min continuous wave (CW) transmission measurement on resonance from a SiNx VGC. PSD is fitted to a 1/f spectrum with Lorentz function and white noise $(A/f^{\alpha} + B\tau/(1+(2\pi f\tau)^2)+C)$ in the red curves. An example trace and an average of 8 separate measurements (shifted by 50 times) are shown on the bottom and top, respectively. (b) An example of $\delta\theta$ vs time. The blue dots are the raw data, and we applied a Gaussian filter in time to obtain the set of smoothed red dots. (c) Inverse of $A_0$ vs. temperature $T$. $A_0$ is the amplitude of 1/f fit of the average PSD. The error bar represents the max and min of $A$ in 8 separate measurements at each $T$. We assume the TLS decoherence rate is temperature dependent: $\Gamma_2(T) = \Gamma_{2,0} + \Gamma_{2,LF}(T)$, where the LF TLS induced dephasing rate $\Gamma_{2,LF}(T) \propto T^{1+\mu}$. From the red fit to Eq. 6.4, we obtain $\mu = 0.32$.

(a) with a shift ($\times 50$). The max and min extracted 1/f noise amplitude ($A$) from the eight scans at each temperature are shown as bars in Fig. 6.12 (c).

The amplitude of 1/f type noise extracted from the averaged PSD is denoted as $A_0$. In the derivation of Ref. [93], we see the noise is given by $1/A_0 \propto \Gamma_2^2/T$ and plot $1/A_0$ vs. $T$ (mK) in Fig. 6.12 (c). In contrast to $\Gamma_2 \propto T^{1+\mu}$, we phenomenologically assume $\Gamma_2(T) = \Gamma_{2,0} + \Gamma_{2,LF}(T)$ to explain our data, where a TLS-induced dephasing $\Gamma_{2,LF}(T) \propto T^{1+\mu}$ and a constant intrinsic dephasing is $\Gamma_{2,0}$. We plot the fit (red) to the equation

$$\frac{1}{A_0} = \frac{(M + N \cdot T^{1+\mu})^2}{T}, \tag{6.4}$$

where $M$ and $N$ are constant, and yield $\mu$ = 0.32. We also plot $\frac{1}{A_0} \propto T^{1+2\mu}$ used in Ref. [93] which has $\Gamma_{2,0}$ = 0 (or M = 0) in black. However, M = 0 is not consistent with our data. The constant $\Gamma_{2,0}$ may originate from other effects, e.g., TLS phonon decay. It also set a bound for the problem of infinite noise ($A \to \infty$) when $T \to 0$ and $\Gamma_{2,0}$ = 0 [38, 93].

### 6.3.6 Annealing effect

In the past, an annealing process is found to lead to a reduction of resonant frequency noise [93]. In four measured SiNx VGCs, the post-annealing at ultrahigh vacuum and 300°C for 1 hour changes the resonant frequency and causes one resonator disappear. The gap distance is modified from a persistent $d \approx$ 125 nm to $d' \approx$ 125, 100, 135 nm labeled as anneal 1 to 3 in Fig. 6.13. There are differences in microwave properties as well. We show the results of three annealed SiNx VGCs, a comparison of one unannealed SiNx VGC (the same VGC in Fig. 6.6), and their fits to the FS model in Fig. 6.13. We find that the $Q_i^0$ is not improved but the

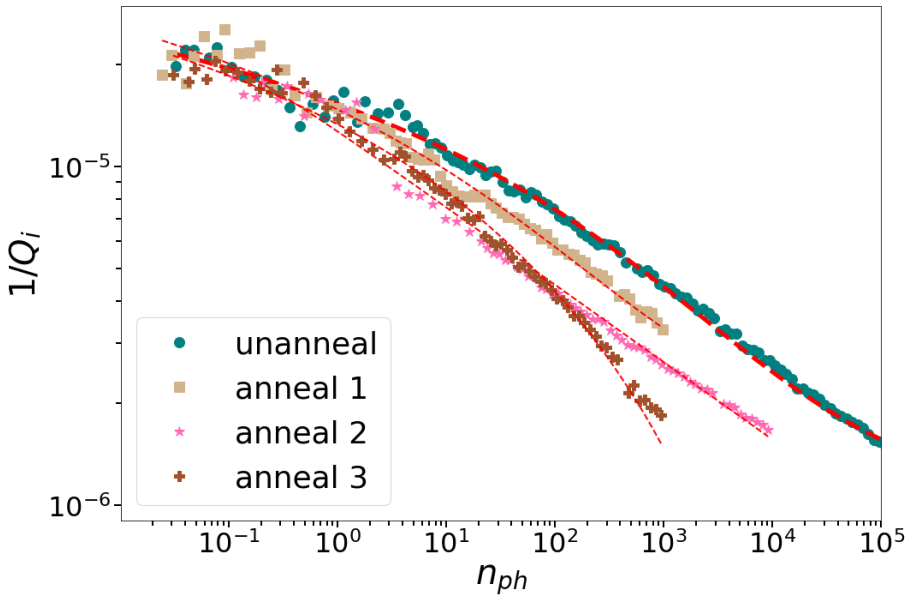


Figure 6.13: $1/Q_i$ vs. $n_{ph}$ of an unannealed and three annealed SiNx VGCs. Label "unanneal" is the same data set from Fig. 6.6 which has the smallest $\gamma_{max}$ among all unannealed VGCs. The red dashed lines are the fits to FS model (Eq. 2.85). We observe that $\gamma_{max}$ of three annealed VGCs is smaller than all unannealed VGCs. There is no improvement in single photon $Q_i^0$. The probable cause to the decrease in $\gamma_{max}$ and unchanged $Q_i^0$ is that the desorption of surface spins constitute LF TLSs, but not coherent TLSs.

maximum jitter rate is reduced by roughly a factor of two to $\gamma_{max} = 2\pi\times$(2.9,1.9,0.9) MHz for anneal 1 to 3, respectively. The reduced value of $\gamma_{max}$ indicates a decrease in LF TLSs number. The improvement is possible from the desorption of surface spins as reported in Ref. [93]. That study finds a slight improvement in $Q_i^0$ and an almost tenfold reduction in the resonant noise. Our results imply that the desorbed surface spins do not contribute to $Q_i^0$ and are LF TLSs instead of cTLSs since only $\gamma_{max}$ decreases.

### 6.3.7 Voltage tunable resonance and nonlinear oscillator

We are able to apply a voltage bias $V_b$ on the capacitors in our design. The accumulated charges on the electrodes would attract and bring two electrodes closer resulting in decrease of the resonance frequency. In Fig. 6.14 (a) and (b), we show the magnitude of transmission $S_{21}$ and the

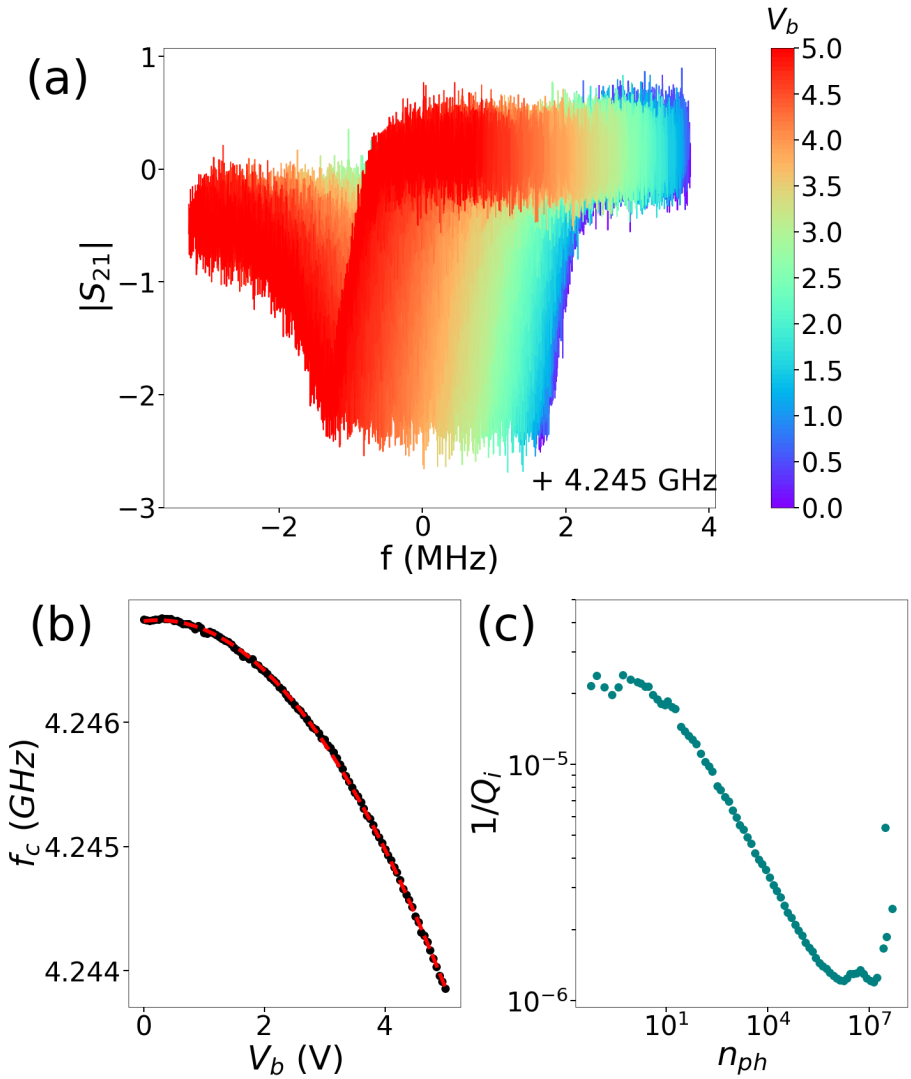


Figure 6.14: Resonance shift due to voltage biasing. (a) $|S_{21}|$ at different voltage bias $V_b$. The rainbow color show the increasing $V_b$ from purple for $V_b$ = 0 to red for $V_b$ = 5V. (b) resonance $f_c$ vs. $V_b$. We found a quadratic decrease in $f_c$ and the fit to $m_2V_b^2+m_1V_b+m_0$, shown in the red line, where $m_2$ = -0.13($\frac{MHz}{V^2}$), $m_1$ = 0.06($\frac{MHz}{V}$) and $m_0$= 4.2468(GHz). (c) $1/Q_i$ vs. $n_{ph}$ from a SiNx VGC. When $n_{ph} > 5 \times 10^6$, $\tan\delta(n_{ph})$ increases due to the high-power-induced quasiparticles. The maximum ac voltage amplitude across the capacitor is $\sqrt{\frac{2hf_c}{C}n_{ph}} = 12$ mV, which does not cause an obvious frequency shift or extra complexity, corresponding to $n_{ph} = 5 \times 10^6$.

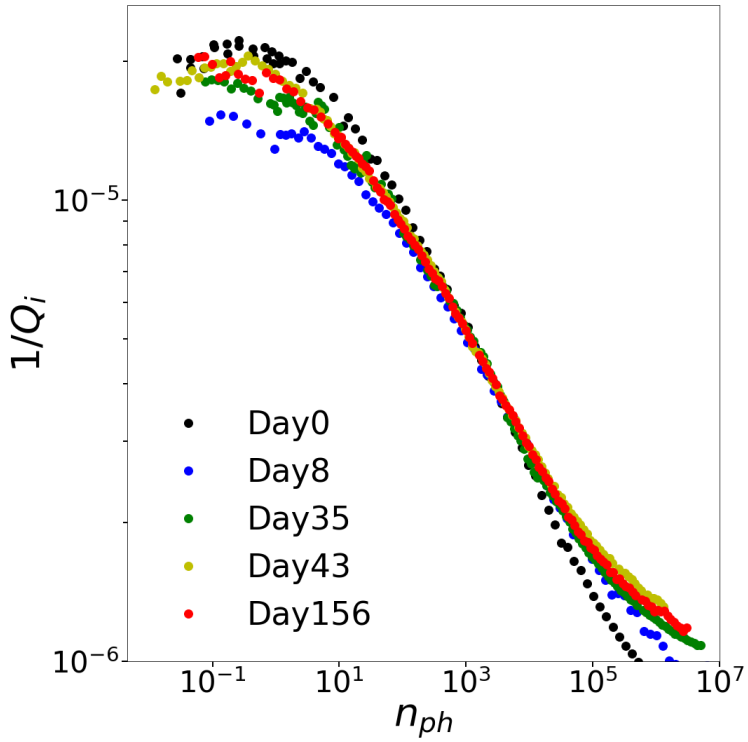


Figure 6.15: The aging effect on a SiNx VGC. The "Day0" indicates the resonator is in the vacuum right after the releasing process. We find the jitter rate $\gamma_{max}$ is slightly increased with time but the changes are small.

resonance $f_c$ at various $V_b$. The $f_c(V_b)$ shows a quadratic dependence: $m_2V_b^2+m_1V_b+m_0$, where $m_2$ = -0.13 ($\frac{MHz}{V^2}$), $m_1$ = 0.06 ($\frac{MHz}{V}$) and $m_0$= 4.2468 (GHz). The red fit line is shown in Fig. 6.14 (b). In Fig. 6.14 (c), we display the resonator has nonlinearity when stored photon number $n_{ph} > 5 \times 10^6$. The amplitude of the voltage $\delta V = \sqrt{\frac{2hf_c}{C}n_{ph}}$ = 12 mV when $n_{ph} = 5 \times 10^6$. Since 12 mV is too small to have a significant effect on resonance, we conclude that the extra loss is due to the quasiparticles induced by broken Cooper pairs.

### 6.3.8 VGC aging effect

We found little effect of aging in our SiNx VGC. In Fig. 6.15, we showed $1/Q_i$ of one SiNx VGC from right after the VGC was released as Day0 (about 2 hours to be pumped into

vacuum) to Day N, where N is the number of days after releasing and the MA interface exposing to the atmosphere. A slightly increased $\gamma_{max}$ change over time implies some accumulation of LF TLSs.

### 6.3.9 Discussion

The dimensionless parameter describing collective mutual TLS-TLS interaction $\chi = P_{0,LF}U_0 \approx 10^{-2} \sim 10^{-3}$ is generally small in bulk films which is critical for the steady-frequency approximation in the STM [97]. Here, $P_{0,LF}$ is the LF TLS density and $U_0$ is the interaction strength of a TLS pair. $Q_i$ in our resonator containing bulk amorphous $\mathrm{AlO_x}$ film is proportional to $\sqrt{n_{ph}}$ so that we expect $\chi$ is ignorable even though TLS spectral diffusion is observed. However MA TLSs agree with the FS model. Thus, we expect that $\chi$ is larger at the Al surface than in the bulk $\mathrm{AlO_x}$ film. The extracted $p$ from Al surface is 1.5 D, which is the same order magnitude of $p$ in bulk amorphous film. Therefore, $U_0$ is expected to be similar in both samples if $U_0$ depends only on electric dipole moment. Furthermore, from the post-annealing experiment, we learn that $P_{0,LF}$ is not necessarily equal to the density of cTLSs $P_{0,c}$, since $\tan\delta^0 \propto P_{0,c}$ is unchanged and $\gamma_{max}$ is reduced by a factor of 3 via the annealing. Thus, one possible explanation for a larger $\chi$ of surface TLSs is that there is a much larger $P_{0,LF}$ at the Al surface than in the bulk $\mathrm{AlO_x}$ film.

Ref. [3] overviews interface losses from a wide variety of materials, substrates and processes through measurements of either lumped or coplanar waveguide resonators. The collective effect from different interfaces brings complexity and it is hard to distinguish the intrinsic loss from a specific interface, though a good attempt has been made in Refs. [87, 144]. Similar problems are in the experiments of planar resonator frequency noise made from various super-

conductors [145]. On the other hand, vacuum-gap resonators and 3D cavities provide the opportunities to study the effect only from a MA interface. For example, Gorgichuk *et al.* study post-treated TESLA Nb cavities at 1.3 GHz and show the importance of accounting the variation of $E_{\mathrm{ZPF}}$. [140]. They claim that $Q_i$ can fit to the STM which is an integral over the surface of the cavity indicating that no extra free parameter $\phi$ is involved. It is likely that the electro-polished cavities with $Q_i^0 = 3 \times 10^{10}$ have extremely low surface TLS density such that $\chi$ is ignorable and $\gamma$ is small. For comparison, the lower $Q_i$ of anodized cavities with a thick surface oxide layer ($\sim$100 nm) shows a low saturation slope of $\phi = 0.25$. This may indicate there are two TLS contributions or interacting TLSs, which can be verified by a two-tone technique in the future.

$Q_i(n_{ph})$ of VGCs follows Eq. 2.85 up to a certain $n_{ph}$ but starts to increases afterward probably due to quasiparticles. In general we only analyze data that is an order of magnitude smaller in photon number than where the loss reverses. The fits of Eq. 2.84 yield $\phi = 0.18 \pm 0.2$ and $n_c \approx 0.1$ and 1 for the SiNx VGC and PR VGC in Fig. 6.6, respectively. Single-photon ${Q_i}^0$ of VGCs also vary with cooldowns up to about 20 percent probably due to a surface oxide aging effect or a new set of TLS after a cooldown-and-warmup.

## 6.4 Conclusion

In the last decade, planar or 2D resonators have been popular in quantum information science. They have a weak photon number ($n_{ph}$) dependence to the loss $1/Q_i \propto n_{ph}^{-\phi}$ at high power, where $\phi$ is a phenomenological fitting parameter. $\phi$ is smaller than 0.5 derived from the standard tunneling model (STM) which is based on the assumption of steady TLS frequency. These resonators have multiple imperfect interfaces, which can host quantum defects. The STM can

possibly explain this phenomenon if multi-interfaces have different TLS types (dipole moment, relaxation rate) or possibly if a broad distribution of electric fields is included from the resonator geometry. In contrast, a fast-switching (FS) TLS model, considering mutual interacting TLSs, would yield a logarithmic power dependence (Eq. 2.85). Typical resonators cannot distinguish which model is correct.

To understand the loss without multiple interface types or distributed fields, we construct resonators with VGCs (Vacuum gap capacitors). These allow us to primarily probe metal-air interface TLSs using this approximation to a parallel plate capacitor. We fabricate these VGCs using two kinds of sacrificial layers, that are SiNx and photoresist, and obtain good internal quality factors of $Q_i > 20$k. The weak $n_{ph}$ dependent loss is best fit to FS model if there is only one TLS type. This contrasts the loss properties of a reference device of amorphous $\mathrm{AlO_x}$, which follows the derivation of STM. Using this VGC structure, we find that surface-based TLSs are distinguishable from bulk TLSs.

Next, we apply a two-tone spectroscopy and find the maximum TLS Rabi frequency $\Omega_{max}$ is weakly dependent to the input power $P_{in}$. All of the equations derived from STM need adjustment of $n_{pu}^{0.5} \rightarrow n_{pu}^{\phi}$, including Eq. 2.84, 2.81, 2.82, and 6.3 in order to fit the experimental data. Therefore, we exclude the MC model which predicts $\phi$ = 0.5, no matter if TLSs have different dipole sizes, coherent times, or different fields. Based on our data from a quasi-parallel plate VGC which gives a weak $n_{ph}$ dependence to $Q_i$ and $\Omega_{max}$, we conclude the TLSs are switching frequencies at a high rate and have a reasonably narrow distribution of TLS parameters.

We observe that the jitter rate of TLSs increases with temperature $T$ from the measurement of loss tangent. Additionally, we observe an increase of TLS dephasing rate on rising $T$ from the resonance phase noise. These effects are believed to arise from the noise of low-frequency

TLSs on high-frequency (near resonant) TLSs [142]. Furthermore, we reduce the density of low-frequency TLSs by post-annealing in vacuum at 300°C for 15 min. This does not change the internal quality factor, which implies the source of low- and high-frequency TLSs are different.

Our study finds substantial difference between the thin-film (bulk) and surface (metal-air interface) TLSs. The MA TLSs are understood using various measurements: power dependent loss, two-tone saturation, and noise spectrum. This work could motivate further studies of TLSs at material interfaces. In the future, a study could be conducted to study surface TLSs at other material interfaces or individual TLSs to confirm the extracted dipole moment (1.5 D).

# Chapter 7: Conclusions

## 7.1 Summary of key results

Quantum computers offer the promise of efficiently solving certain problems that are computational complex for classical computers [12, 14, 16]. In the development of quantum computers, many candidates are proposed such as trapped ions, photons, defect spins, and superconducting qubits. In particular, superconducting qubits are one of the leading candidate for scalable quantum processor architecture. Superconducting qubits are highly flexible to design. Different types of high-coherent qubits, such as transmon, fluxonium, zero−pi qubit, etc, have the capacitance, inductance, and Josephson energy in different regimes. With the demonstrations of multiple high-fidelity, two-qubit gates as well as quantum error correction producing logical qubits (in extensible superconducting qubit systems), Google has shown a clear quantum advantage over a classical computer [146].

However, the local environment surrounding qubits are sources of noise that lead to decoherence and reduce the operational fidelity of the qubits. Two-level-systems (TLSs) retain substantial amounts of attentions because they are seen as a major source of decoherence in superconducting qubits. TLSs also affect other quantum devices including semiconducting qubits, kinetic-inductance photon detectors, quantum-limited microwave amplifiers, and quantum transducers. Superconducting qubits typically contain aluminium oxide because it enables high-

quality Josephson junctions using the well-developed techniques, i.e., double angle shadow evaporation. Aluminium oxide, an amorphous material, will grow once Al exposes to oxygen, which is characterized by a large dielectric loss and a high TLS density. Moreover, TLSs in the insulating tunnel barrier of JJs usually strongly couple to qubitsand cause qubits to exhibit splittings or dips in $T_1$. Studying TLSs of aluminum oxide is extremely important to enhance the coherent time of qubits.

A good qubit frequency targeting, the process of reducing mismatch between the designed and the measured qubit frequency during fabrication, is important in designs with multiple qubits. To avoid unintentional crosstalk, qubits should not have coincident frequencies: $\omega_{10}^{A} = \omega_{10}^{B}$ or $\omega_{10}^{A} = \omega_{21}^{B}$. The crosstalks depend on the detuning between two qubits and are identified as a dominant source for gate error. However, the intended qubit frequency is usually unmatched with the measured frequency due to the uncertainty of $\mathrm{AlO_x}$ thickness. Moreover, despite the well-developed fabrication process, using e-beam lithography has a huge drawback that it cannot have a massive and fast production compared to CMOS fabrication using optical lithography. There are questions if optical-lithography-made qubits can perform as good as the e-beam method in coherent properties and in frequency targeting. In Chapter 4, we show data from transmon qubits fabricated on 300 mm Si wafers with a resistivity of 10 kΩ-cm by only optical lithography processes. We measure $\mathrm{T_1}$ = 26 and 23 $\mu$s in two transmons and the standard deviation in resistance is 2.8 to 3.6%, which is comparable to e-beam method.

In Chapter 5, we utilize Electrical-Bridge Quantum-Defect Sensor to extract the dipole moment $p_z$ of hundreds of individual TLSs in polycrystalline $\gamma - \mathrm{Al_2O_3}$ and amorphous $\mathrm{a - AlO_x}$. The sensor contains a film that is 20 nm thick that hosts TLSs. TLSs in $\gamma - \mathrm{Al_2O_3}$ films are relatively stable. The material histogram of $p_z$ reveals that $\gamma - \mathrm{Al_2O_3}$ fits well to a single Gaussian

peak. We obtain that the mean TLS moment of $\gamma - Al_2O_3$ is $p_z$ =2.6±0.3 D and $\sigma$ = 1.6±0.2 D. Furthermore, the material distribution disagrees with the isotropic model derived from STM commonly used in amorphous materials.

The ability to extract an accurate mean $p_z$ puts constraints on its defect type, and we find a clear difference in the dipole moment distribution from the film types, indicating a difference in TLS structures. We make first comparisons to new microscopic structures used in DFT calculations (delocalized O and hydrogen-based TLSs). The $\gamma - Al_2O_3$ data show one dominant peak with a mean $p_z$ = 2.6 Debye. This indicates the dominance of one TLS origin (likely to be H-TLS). On the other hand, $a - AlO_x$ has a larger mean $p_z$ = 4.6±0.5 D, which is consistent with previous amorphous alumina results. The moments above 8.6 D (10% of the distribution) are larger than any TLS in polycrystalline alumina and agree only with calculations of delocalized O atoms. Based on data and the candidate models, we find that polycrystalline alumina has smaller ratio of O-based to H-based TLS than that of amorphous alumina.

In Chapter 6, we construct resonators with VGCs (Vacuum gap capacitors). These allow us to primarily study metal-air interface TLSs without contributions from other interfaces and keep the distribution of $E_{zpf}$ simple. We fabricate these VGCs using two kinds of sacrificial layers, that are SiNx and S1805 photoresist, and obtain good internal quality factors of $Q_i^0 >$ 20k. The weak $n_{ph}$ dependent loss is best fit to the model, which assumes TLS frequencies are unstable. This contrasts the loss properties of a reference device of amorphous $AlO_x$, which follows the derivation of STM. Using this VGC structure, we find that surface-based TLSs are distinguishable from bulk TLSs. We apply a two-tone spectroscopy, which extracts the maximum TLS Rabi frequency $\Omega_{max}$ as a fit parameter at a particular input power $P_{in}$. All of the equations derived from STM need adjustment of $n_{pu}^{0.5} \rightarrow n_{pu}^{\phi}$, including Eq. 2.84, 2.81, 2.82, and 6.3 in

order to fit the experimental data. With $n_{ph}$ dependent loss data, we exclude the MC model which predicts $\phi$ = 0.5, no matter if TLSs have different dipole size or are under different fields. We also extract the dipole moment $p$ = 1.5 $\pm$ 0.3 D from our quasi-uniform zero-point electric field fluctuation. Based on the weak $n_{ph}$ dependence to $Q_i$ and $\Omega_{max}$, we conclude there is only one type of TLS and TLSs are switching their frequencies at a high rate. The power spectral density of resonator transmission rate $S_{21}$ at various temperatures indicates that TLS dephasing rate is a function of temperature. The jitter rate $\gamma$ decreases after annealing the devices in vacuum at 300°C but $\tan\delta^0$ is unchanged. Those indirect evidences also show that TLSs are influenced by the far-detuned TLSs which can have a different density.

This thesis presents our studies of aluminum oxide in different structural phases. TLSs in different structural phases behave differently such that the conventional STM is not adequate to describe the phenomena. The EBQuDS is a powerful tool to extract the information of the dipole moment, which allows comparison to theoretical models, and can help pin down the origins of TLSs.

# Appendix A: Fabrication recipes

## A.1 Recipes of device fabrication

### A.1.1 Optical lithography fabrication: photoresist and patterning

All the lithography processes are using the positive photoresist (OiR 906-10) expect for the sacrificial layer of vacuum-gap capacitors.

1. Dehydrate the wafer at 90°C for 5 min
2. Spin HMDS at 3000 rpm for 60 sec, spin OiR 906 at 3000 rpm for 60 sec
3. Pre-bake at 90°C for 60 sec, expose at a dose of 180 mJ/m$^2$, and post-bake at 120°C for 60 sec
4. Develop in OPD-4262 for 45 sec, rinse in DI water, and blow dry by nitrogen gun
5. Etching process (wet etch, ICP etch, etc)
6. Rinse and sonicate in acetone and IPA separately

### A.1.2 Deposition

1. Sputtering Aluminum by AXXIS

(a) Load wafer into loadlock chamber and pump down for 30 min (pressure is around $3 \times 10^{-6}$ Torr).

(b) Transfer to processing chamber (PC) and pump down $< 10^{-7}$ Torr.

(c) Inject 10 mTorr Ar and turn on DC voltage (100V) to ionize Ar.

(d) Pre-sputtering Al target for 5 min to reduce the Al oxide on the target surface.

(e) Reduce Ar pressure to 1 mTorr and open shutter for deposition.

(f) Turn off shutter, DC voltage and Ar gas gate.

(g) Wait for 10 min before exposing to atmosphere due to the sputtering-induced heat on the substrate.

2. E-beam evaporate Al by AXXIS

(a) Load wafer into loadlock chamber and pump down for 30 min (pressure is around $3 \times 10^{-6}$ Torr).

(b) Transfer to processing chamber (PC) and pump down $< 10^{-7}$ Torr.

(c) Open filament and increase the current to heat up the crucible.

(d) PID control the deposition rate as 0.2 nm/sec and open shuttle.

(e) Turn off shutter and cooldown for 10 minutes.

(f) Transfer back to loadlock chamber.

### A.1.3 Etching

1. Ion-milling for via connection

(a) Turn on Ar gas and the filament at 300 V

(b) Open shutter for 20 sec and close shutter for 1 min and wait the heat diffuses from the substrate.

(c) Repeat (b) two times. The total etching time is 1 min

(d) Turn off Ar gas and filament

2. RIE O2 descum: 150W RF power resulting in etch rate = 3 nm/sec for S1805

3. ICP SiNx releasing: 2000 W ICP power and 0 W forward power at 20 mT SF6 gas resulting in a lateral etch rate = 6 $\mu$m/hr

4. ICP Al etching: 500W ICP power and 50W forward power at 0.5 mT BCl3/Cl2 (3:2) gas resulting in etch rate = 10 nm/sec

### A.1.4 Vacuum-gap capacitor fabrication recipe

The fabrication process of vacuum-gap capacitors is the following. See the illustration of each step in Fig. A.1and the corresponding design pattern in Fig. A.2.

i) SiNx VGC

(a) E-beam evaporate 100 nm Al on sapphire, spin photoresist and pattern the ground/bottom electrode layers by wet etching.

(b) Deposit low loss and low strain 200-nm SiNx

(c) Spin photoresist and pattern the via holes and supporting poles.

(d) Ion-milling surface by 3 iterations of Recipe Etching 1, deposit 300 nm Al by e-beam evaporation, spin photoresist and pattern the top electrode layer by wet etching.

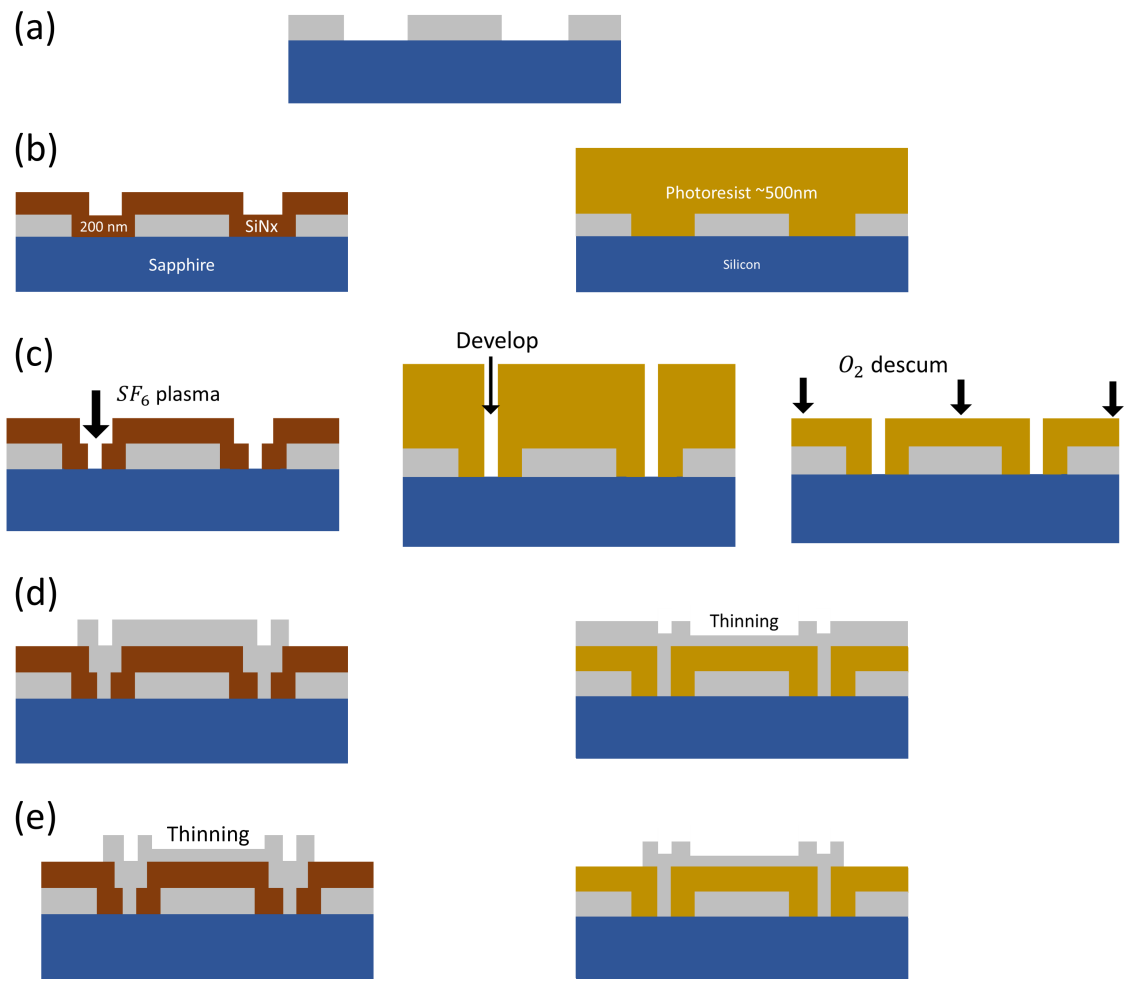


Figure A.1: Illustrations of the fabrication of vacuum-gap resonators with SiNx (left) and photoresist (right) as sacrificial layers (SLs). (a) Bottom e-beam evaporated Al layer is deposited and patterned. (b) SiNx SLs are deposited at 300°C or PR SLs are spun. (c) On top of SiNx SL, the PR layer is spun and exposed. For PR SL, the SL is exposed and developed. An additional step of $O_2$ descum reduces the thickness from 500 to 200 nm. (d) Before top Al layers are deposited, SLs are cleaned by ion-milling. The recipe for ion-milling is provided in this appendix. (e) Top Al layers are patterned and etched by wet chemicals for SiNx or dry-etching for PR. (e) Top electrodes are partially etched to reduce the mass if needed. After this step, SLs are ready to be released.

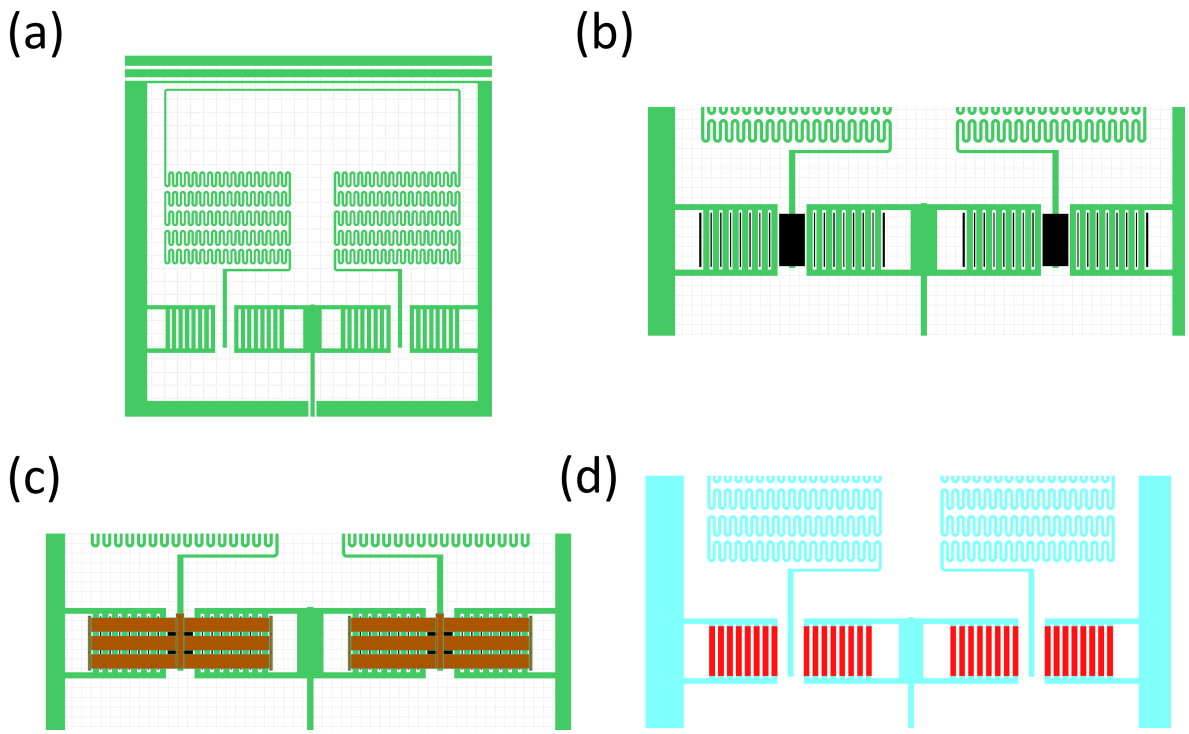


Figure A.2: (a) Ground and bottom layer (b) Via and supporting pole layer (c) Top electrode layer (d) Thinning layer

(e) [Optional] Spin photoresist and pattern the thinning area by wet etching. This step can be done after dicing as well.

(f) Spin thick photoresist, dice into a chip size and release SiNx by Recipe Etching 3.

ii) Photoresist S1805 VGC

(a) E-beam evaporate 100 nm Al on a silicon wafer, spin photoresist and pattern the ground/bottom electrode layers by wet etching.

(b) Spin S1805 at 4000 rpm for 60 sec, pre-bake under 120 °C for 60 sec.

(c) Expose S1805 with the pattern, develop by Microposit MF-CD-26 for 10 sec, check the thickness is about 500 nm, timed-etch the photoresist by O2 plasma (Recipe Etching 2), and post-bake under 120 °C for 4 min.

(d) Ion-milling surface by 3 iterations of Recipe Etching 1, deposit 300 nm Al by e-beam evaporation, spin photoresist, pattern the thinning area by ICP dry etching (Recipe Etching 4), and blow acetone and IPA by spray gun to remove photoresist. Note that do not rinse in acetone which will remove S1805 as well.

(e) Blow dry, spin photoresist and pattern the top electrode.

(f) Spin thick photoresist, dice into chip size and release S1805 by NMP for 3 hours.

# Appendix B: Fitting procedures for Chapter 5

## B.1 Fitting of hyperbolas in DC sweep plot

This section is describing the procedure of fitting the TLS dipole in Chapter 5. Take Fig. 5.6 as an example, We search the local minimum (hybridized state) of each $|S_{21}|$ and apply a Gaussian filter on the 2D plot of the local minimum. The result is shown in Fig. B.1 (a). We obtain the initial guess values of $\Delta_0$, $V_{bias}$, and $p_z$ for all possible TLS candidates. Due to the complexity of the TLS spectrum, TLSs are fitted separately in the order of their $\Delta_0$ from the largest to the smallest. The first candidate TLS with the largest $\Delta_0$ is fitted by the Monte Carlo method and the result is shown in Fig B.1 (b). We assign those local minimum to first TLS and subtract them from Fig. B.1 (a) to get Fig. B.1 (c). For the next TLS, we use the local minimum plot from Fig. B.1 (c) and the next fitting will not be affected by the previous TLS result. We repeat the process until all TLSs are fit and discard those TLSs not crossing their minimum energies.

## B.2 Fitting of TLS density by maximum likelihood estimation

Here, we show the procedure of applying Fisher's maximum likelihood estimation (MLE) on our dipole moment statistics. For simplicity, we choose truncated normal distribution as our

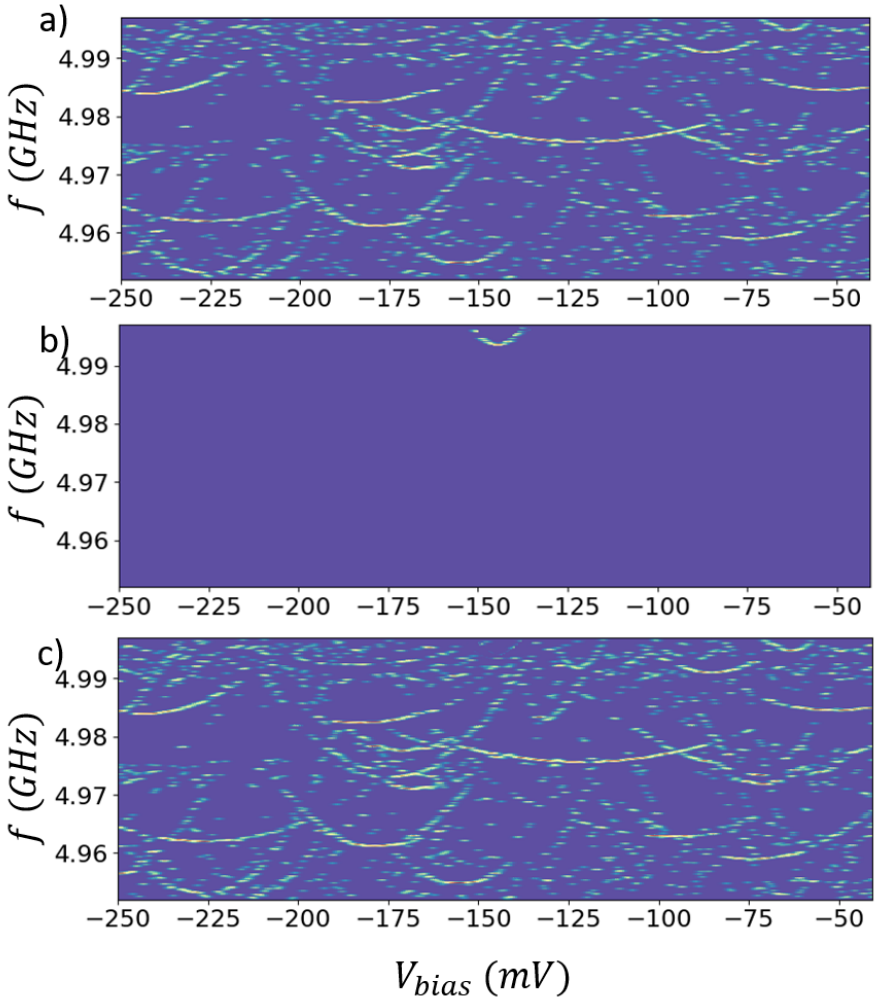


Figure B.1: (a) Plot of extracted minimum energies in Fig 2 of main text. (b) The final result of first dipole fit. (c) Subtract the first dipole fitting result from (a).

target function $f(p_z;\ \mu,\ \sigma)$ to fit our material density $D(p_z)$, and

$$f(p_z;\ \mu,\ \sigma)\ =\ C(\mu,\sigma)\,\frac{1}{\sigma\sqrt{2\pi}}\exp\left(-\frac{(p_z\ -\ \mu)^2}{2\sigma^2}\right) \tag{B.1}$$

for $p_z \in [0,\infty)$, where $\mu$ is the mean value, $\sigma$ is the standard deviation. The normalized constant

$$C(\mu,\sigma)\ =\ \frac{2}{1-\mathrm{erf}(-\mu/\sigma\sqrt{2})} \tag{B.2}$$

depends only on $\mu$ and $\sigma$, where erf(x) is error function defined as

$$\mathrm{erf}(x)\ =\ \frac{2}{\sqrt{\pi}}\int_0^x \exp(-t^2)dt. \tag{B.3}$$

The likelihood function

$$L\ =\ \prod_i f(p_{zi};\ \mu,\ \sigma). \tag{B.4}$$

The necessary conditions for the occurrence of a maximum (or a minimum) are

$$\frac{\partial ln(L)}{\partial\mu}\ =\ 0,\ \frac{\partial ln(L)}{\partial\sigma}\ =\ 0. \tag{B.5}$$

Since $D(p_z)$ is not a directly measurement result and $H(p_z)is$, there is a weighing factor $p_z$ transferring $D(p_z)$ to $H(p_z)$. This leads to

$$H(p_z;\ \mu,\ \sigma)\ =\ N_{tot}\,C_1(\mu,\sigma)p_z\exp\left(-\frac{(p_z\ -\ \mu)^2}{2\sigma^2}\right). \tag{B.6}$$

A new normalization constant is

$$C_1(\mu,\sigma) \;=\; \sigma^2 \exp\left(-\frac{\mu^2}{2\sigma^2}\right) + \mu\,\sigma\,\sqrt{\frac{\pi}{2}}\left(1-\operatorname{erf}\left(-\frac{\mu}{\sigma\sqrt{2}}\right)\right), \tag{B.7}$$

and $N_{tot}$ is the total observed TLS.

We also apply a gamma distribution function $f_1$ and a mirrored Gaussian distribution function $f_2$ to fit the data.

$$f_1(x,\alpha,\beta) \;=\; \frac{x^{\alpha}\,e^{-\beta\,x}}{\Gamma(\alpha)\beta^{\alpha}}, \tag{B.8}$$

and $\Gamma(\alpha)$ is a gamma function. The fitting result gives $\alpha$ = 5.15 and $\beta$ = 1.72 and mean = 2.99 D. However, we expect there is a distribution $> 0$ when dipole equals 0 so that gamma distribution is not suitable. $f_2$ contains two Gaussian distributions with opposite sign of mean value $\pm\mu$ and

$$f_2(x,\mu,\sigma) \;=\; \frac{1}{2\sigma\sqrt{2\pi}}\left[\exp\left(-\frac{(p_z\,-\,\mu)^2}{2\sigma^2}\right)+\exp\left(-\frac{(p_z\,+\,\mu)^2}{2\sigma^2}\right)\right]. \tag{B.9}$$

We obtain $\mu$ = 2.73 and $\sigma$ = 1.63, which are slightly different than the mean value obtained from the truncated Gaussian function.

MLE method applied to the amorphous alumina measured histogram does not adequately give the main peak feature in the material distribution $D(p_z)$. Thus, we do not use MLE to report averaged dipole in the amorphous data, but rather a calculated mean and standard deviation. See

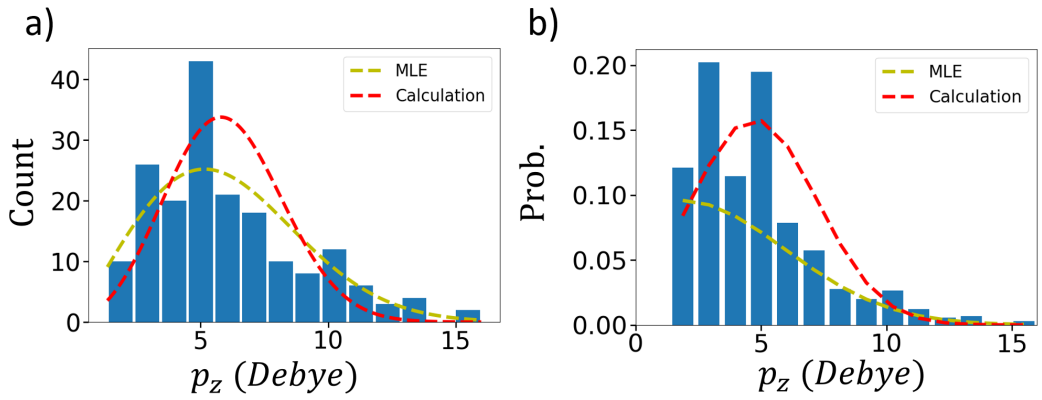


Figure B.2: (a) Histogram of amorphous alumina dipole moment $H(p_z)$. (b) TLS density $D(p_z)$. The red lines are Gaussian function with a calculated mean and standard deviation mention in Chapter 5. The yellow lines are the fit to Eq. B.6.

Fig. B.2.

# Appendix C: Extra alumina TLS spectrum

This section shows additional spectroscopy data sets from different cooldowns on the two alumina types. Fig. C.1 shows $\gamma - Al_2O_3$ TLS spectra during voltage biasing and Fig. C.2 shows TLS spectra in the time domain. Fig. C.3 shows an unsuccessful spectrum of a-$AlO_x$ deposited in 70°C.

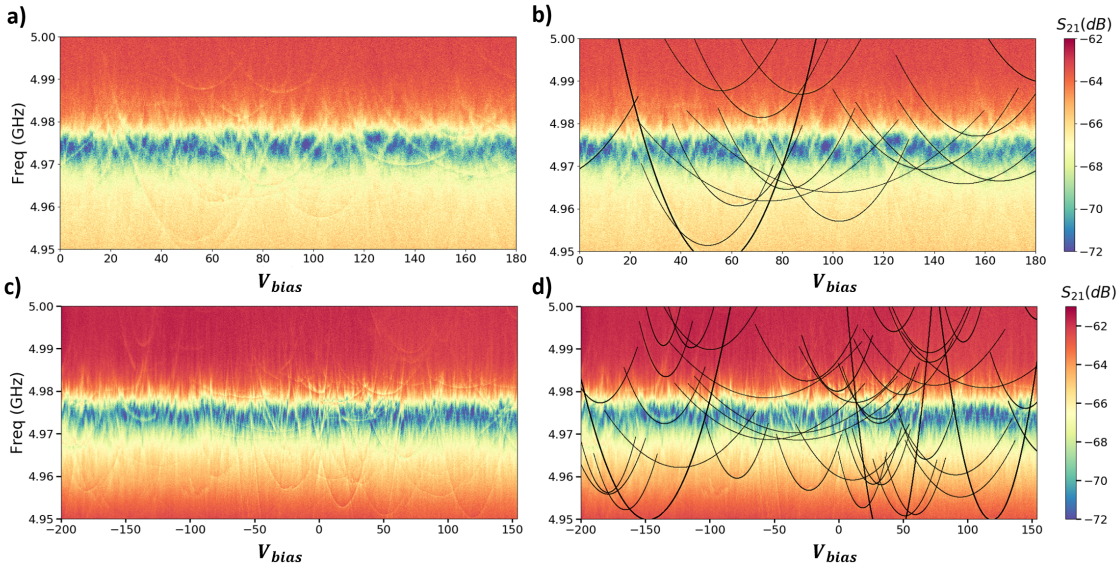


Figure C.1: TLS spectroscopy of $\gamma - Al_2O_3$ TLS. Fig. (a) and (c) show two raw data sets, while Fig. (b) and (d) show TLS spectra with TLS fittings, respectively. The data sets are measured in different cooldowns.

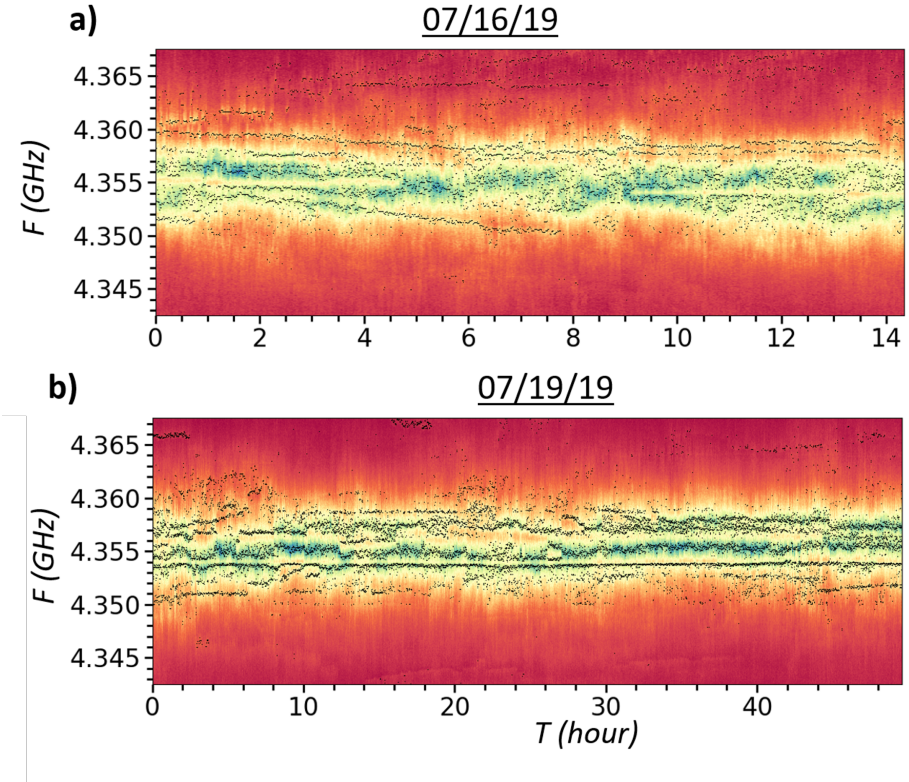


Figure C.2: TLS dynamic in the time domain in two different dates.

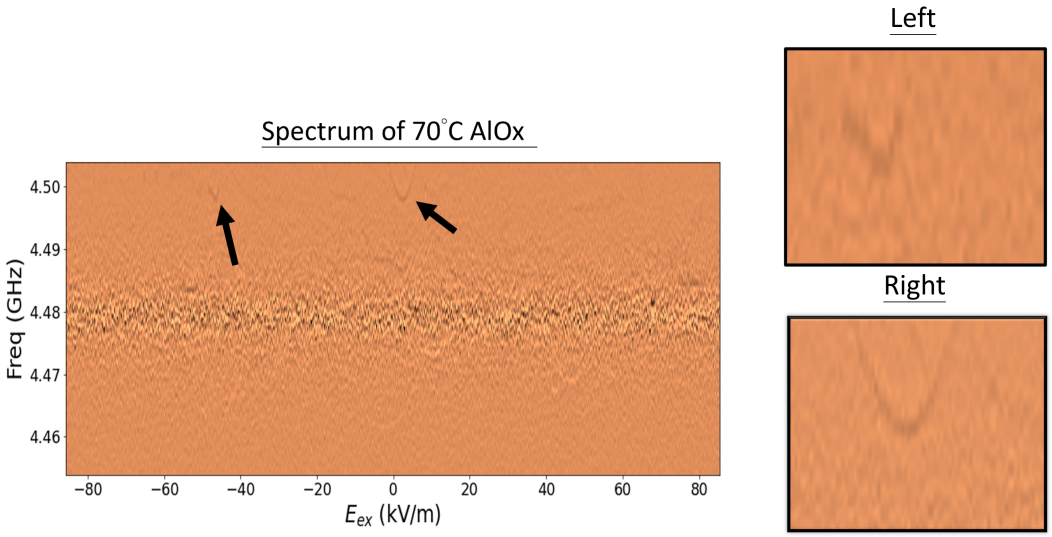


Figure C.3: Left: TLS spectrum of a-$AlO_x$ deposited in 70°C. Only two TLSs are observed. Right: Zoom-in of the left and right TLS.

# Bibliography


[1] Farzan Jazaeri, Arnout Beckers, Armin Tajalli, and Jean-Michel Sallese. A review on quantum computing: From qubits to front-end electronics and cryogenic mosfet physics. In *2019 MIXDES-26th International Conference" Mixed Design of Integrated Circuits and Systems"*, pages 15–25. IEEE, 2019.

[2] Mostafa Khezri. Dispersive measurement of superconducting qubits. 2018.

[3] Corey Rae Harrington McRae, Haozhi Wang, Jiansong Gao, Michael R Vissers, Teresa Brecht, Andrew Dunsworth, David P Pappas, and Josh Mutus. Materials loss measurements using superconducting microwave resonators. *Review of Scientific Instruments*, 91(9):091101, 2020.

[4] RC Zeller and RO Pohl. Thermal conductivity and specific heat of noncrystalline solids. *Physical Review B*, 4(6):2029, 1971.

[5] JC Lasjaunias, A Ravex, M Vandorpe, and S Hunklinger. The density of low energy states in vitreous silica: specific heat and thermal conductivity down to 25 mk. *Solid State Communications*, 17(9):1045–1049, 1975.

[6] Philip Krantz, Morten Kjaergaard, Fei Yan, Terry P Orlando, Simon Gustavsson, and William D Oliver. A quantum engineer's guide to superconducting qubits. *Applied Physics Reviews*, 6(2):021318, 2019.

[7] Jian-Qiang You and Franco Nori. Atomic physics and quantum optics using superconducting circuits. *Nature*, 474(7353):589–597, 2011.

[8] N Foroozani, C Hobbs, CC Hung, S Olson, D Ashworth, E Holland, M Malloy, P Kearney, B O'Brien, B Bunday, et al. Development of transmon qubits solely from optical lithography on 300 mm wafers. *Quantum Science and Technology*, 4(2):025012, 2019.

[9] B. Sarabi, A. N. Ramanayaka, A. L. Burin, F. C. Wellstood, and K. D. Osborn. Projected dipole moments of individual two-level defects extracted using circuit quantum electrodynamics. *Phys. Rev. Lett.*, 116:167002, Apr 2016.

[10] S Fritz, L Radtke, R Schneider, M Luysberg, M Weides, and D Gerthsen. Structural and nanochemical properties of alox layers in al/alox/al-layer systems for josephson junctions. *Physical Review Materials*, 3(11):114805, 2019.

[11] Richard P Feynman. Simulating physics with computers. In *Feynman and computation*, pages 133–153. CRC Press, 2018.

[12] Peter W Shor. Polynomial-time algorithms for prime factorization and discrete logarithms on a quantum computer. *SIAM review*, 41(2):303–332, 1999.

[13] Daniel S Abrams and Seth Lloyd. Simulation of many-body fermi systems on a universal quantum computer. *Physical Review Letters*, 79(13):2586, 1997.

[14] Dan Boneh and Richard J Lipton. Quantum cryptanalysis of hidden linear functions. In *Annual International Cryptology Conference*, pages 424–437. Springer, 1995.

[15] David Deutsch and Richard Jozsa. Rapid solution of problems by quantum computation. *Proceedings of the Royal Society of London. Series A: Mathematical and Physical Sciences*, 439(1907):553–558, 1992.

[16] Lov K Grover. A fast quantum mechanical algorithm for database search. In *Proceedings of the twenty-eighth annual ACM symposium on Theory of computing*, pages 212–219, 1996.

[17] John Preskill. Quantum computing 40 years later. *arXiv preprint arXiv:2106.10522*, 2021.

[18] Nikolaj Moll, Panagiotis Barkoutsos, Lev S Bishop, Jerry M Chow, Andrew Cross, Daniel J Egger, Stefan Filipp, Andreas Fuhrer, Jay M Gambetta, Marc Ganzhorn, et al. Quantum optimization using variational algorithms on near-term quantum devices. *Quantum Science and Technology*, 3(3):030503, 2018.

[19] Pulak Ray, Bikas K Chakrabarti, and Arunava Chakrabarti. Sherrington-kirkpatrick model in a transverse field: Absence of replica symmetry breaking due to quantum fluctuations. *Physical Review B*, 39(16):11828, 1989.

[20] Andrew A Houck, Hakan E Türeci, and Jens Koch. On-chip quantum simulation with superconducting circuits. *Nature Physics*, 8(4):292–299, 2012.

[21] Alberto Galindo and Miguel Angelo Martin-Delgado. Information and computation: Classical and quantum aspects. *Reviews of Modern Physics*, 74(2):347, 2002.

[22] Göran Wendin. Quantum information processing with superconducting circuits: a review. *Reports on Progress in Physics*, 80(10):106001, 2017.

[23] Morten Kjaergaard, Mollie E Schwartz, Jochen Braumüller, Philip Krantz, Joel I-J Wang, Simon Gustavsson, and William D Oliver. Superconducting qubits: Current state of play. *Annual Review of Condensed Matter Physics*, 11:369–395, 2020.

[24] Peter W Shor. Scheme for reducing decoherence in quantum computer memory. *Physical review A*, 52(4):R2493, 1995.

[25] Paul T Cochrane, Gerard J Milburn, and William J Munro. Macroscopically distinct quantum-superposition states as a bosonic code for amplitude damping. *Physical Review A*, 59(4):2631, 1999.

[26] A Robert Calderbank, Eric M Rains, PM Shor, and Neil JA Sloane. Quantum error correction via codes over gf (4). *IEEE Transactions on Information Theory*, 44(4):1369–1387, 1998.

[27] Austin G Fowler, Matteo Mariantoni, John M Martinis, and Andrew N Cleland. Surface codes: Towards practical large-scale quantum computation. *Physical Review A*, 86(3):032324, 2012.

[28] Thaddeus D Ladd, JR Goldman, F Yamaguchi, Y Yamamoto, E Abe, and Kohei M Itoh. All-silicon quantum computer. *Physical Review Letters*, 89(1):017901, 2002.

[29] Pieter Kok, William J Munro, Kae Nemoto, Timothy C Ralph, Jonathan P Dowling, and Gerard J Milburn. Linear optical quantum computing with photonic qubits. *Reviews of modern physics*, 79(1):135, 2007.

[30] Jonathan A Jones and Michele Mosca. Implementation of a quantum algorithm on a nuclear magnetic resonance quantum computer. *The Journal of chemical physics*, 109(5):1648–1653, 1998.

[31] Lilian Childress and Ronald Hanson. Diamond nv centers for quantum computing and quantum networks. *MRS bulletin*, 38(2):134–138, 2013.

[32] Xuedong Hu and S Das Sarma. Hilbert-space structure of a solid-state quantum computer: Two-electron states of a double-quantum-dot artificial molecule. *Physical Review A*, 61(6):062301, 2000.

[33] Hartmut Häffner, Christian F Roos, and Rainer Blatt. Quantum computing with trapped ions. *Physics reports*, 469(4):155–203, 2008.

[34] John M Martinis, Ken B Cooper, Robert McDermott, Matthias Steffen, Markus Ansmann, KD Osborn, Katarina Cicak, Seongshik Oh, David P Pappas, Raymond W Simmonds, et al. Decoherence in josephson qubits from dielectric loss. *Physical review letters*, 95(21):210503, 2005.

[35] Jens Koch, M Yu Terri, Jay Gambetta, Andrew A Houck, David Isaac Schuster, Johannes Majer, Alexandre Blais, Michel H Devoret, Steven M Girvin, and Robert J Schoelkopf. Charge-insensitive qubit design derived from the cooper pair box. *Physical Review A*, 76(4):042319, 2007.

[36] Michel H Devoret and Robert J Schoelkopf. Superconducting circuits for quantum information: an outlook. *Science*, 339(6124):1169–1174, 2013.

[37] LJ Zeng, S Nik, Tine Greibe, Philip Krantz, CM Wilson, Per Delsing, and Eva Olsson. Direct observation of the thickness distribution of ultra thin alox barriers in al/alox/al josephson junctions. *Journal of Physics D: Applied Physics*, 48(39):395308, 2015.

[38] Clemens Müller, Jared H Cole, and Jürgen Lisenfeld. Towards understanding two-level-systems in amorphous solids: insights from quantum circuits. *Reports on Progress in Physics*, 82(12):124501, 2019.

[39] Steffen Schlör, Jürgen Lisenfeld, Clemens Müller, Alexander Bilmes, Andre Schneider, David P Pappas, Alexey V Ustinov, and Martin Weides. Correlating decoherence in transmon qubits: Low frequency noise by single fluctuators. *Physical review letters*, 123(19):190502, 2019.

[40] Jonathan J Burnett, Andreas Bengtsson, Marco Scigliuzzo, David Niepce, Marina Kudra, Per Delsing, and Jonas Bylander. Decoherence benchmarking of superconducting qubits. *npj Quantum Information*, 5(1):1–8, 2019.

[41] Chen Wang, Yvonne Y Gao, Ioan M Pop, Uri Vool, Chris Axline, Teresa Brecht, Reinier W Heeres, Luigi Frunzio, Michel H Devoret, Gianluigi Catelani, et al. Measurement and control of quasiparticle dynamics in a superconducting qubit. *Nature communications*, 5(1):1–7, 2014.

[42] Gianluigi Catelani, Simon E Nigg, Steven M Girvin, Robert J Schoelkopf, and Leonid I Glazman. Decoherence of superconducting qubits caused by quasiparticle tunneling. *Physical Review B*, 86(18):184514, 2012.

[43] Alexander PM Place, Lila VH Rodgers, Pranav Mundada, Basil M Smitham, Mattias Fitzpatrick, Zhaoqi Leng, Anjali Premkumar, Jacob Bryon, Andrei Vrajitoarea, Sara Sussman, et al. New material platform for superconducting transmon qubits with coherence times exceeding 0.3 milliseconds. *Nature communications*, 12(1):1–6, 2021.

[44] J Verjauw, A Potočnik, M Mongillo, R Acharya, F Mohiyaddin, G Simion, A Pacco, Ts Ivanov, D Wan, A Vanleenhove, et al. Investigation of microwave loss induced by oxide regrowth in high-q niobium resonators. *Physical Review Applied*, 16(1):014018, 2021.

[45] Michael R Vissers, Jiansong Gao, David S Wisbey, Dustin A Hite, Chang C Tsuei, Antonio D Corcoles, Matthias Steffen, and David P Pappas. Low loss superconducting titanium nitride coplanar waveguide resonators. *Applied Physics Letters*, 97(23):232509, 2010.

[46] CJK Richardson, A Alexander, CG Weddle, B Arey, and M Olszta. Low-loss superconducting titanium nitride grown using plasma-assisted molecular beam epitaxy. *Journal of Applied Physics*, 127(23):235302, 2020.

[47] Chris Macklin, K O'brien, D Hover, ME Schwartz, V Bolkhovsky, X Zhang, WD Oliver, and I Siddiqi. A near–quantum-limited josephson traveling-wave parametric amplifier. *Science*, 350(6258):307–310, 2015.

[48] M Hatridge, R Vijay, DH Slichter, John Clarke, and I Siddiqi. Dispersive magnetometry with a quantum limited squid parametric amplifier. *Physical Review B*, 83(13):134501, 2011.

[49] Michael R Vissers, Robert P Erickson, H-S Ku, Leila Vale, Xian Wu, GC Hilton, and David P Pappas. Low-noise kinetic inductance traveling-wave amplifier using three-wave mixing. *Applied physics letters*, 108(1):012601, 2016.

[50] Vladimir E Manucharyan, Jens Koch, Leonid I Glazman, and Michel H Devoret. Fluxonium: Single cooper-pair circuit free of charge offsets. *Science*, 326(5949):113–116, 2009.

[51] András Gyenis, Pranav S Mundada, Agustin Di Paolo, Thomas M Hazard, Xinyuan You, David I Schuster, Jens Koch, Alexandre Blais, and Andrew A Houck. Experimental realization of a protected superconducting circuit derived from the 0–$\pi$ qubit. *PRX Quantum*, 2(1):010339, 2021.

[52] B Foxen, JY Mutus, E Lucero, R Graff, A Megrant, Yu Chen, C Quintana, B Burkett, J Kelly, E Jeffrey, et al. Qubit compatible superconducting interconnects. *Quantum Science and Technology*, 3(1):014005, 2017.

[53] D Rosenberg, D Kim, R Das, D Yost, S Gustavsson, D Hover, P Krantz, A Melville, L Racz, GO Samach, et al. 3d integrated superconducting qubits. *npj quantum information*, 3(1):1–5, 2017.

[54] Goran Lindblad. On the generators of quantum dynamical semigroups. *Communications in Mathematical Physics*, 48(2):119–130, 1976.

[55] MD Reed, L DiCarlo, BR Johnson, L Sun, DI Schuster, L Frunzio, and RJ Schoelkopf. High-fidelity readout in circuit quantum electrodynamics using the jaynes-cummings nonlinearity. *Physical review letters*, 105(17):173601, 2010.

[56] Theodore Walter, Philipp Kurpiers, Simone Gasparinetti, Paul Magnard, Anton Potočnik, Yves Salathé, Marek Pechal, Mintu Mondal, Markus Oppliger, Christopher Eichler, et al. Rapid high-fidelity single-shot dispersive readout of superconducting qubits. *Physical Review Applied*, 7(5):054020, 2017.

[57] Alicia J Kollár, Mattias Fitzpatrick, and Andrew A Houck. Hyperbolic lattices in circuit quantum electrodynamics. *Nature*, 571(7763):45–50, 2019.

[58] Paul Adrien Maurice Dirac. The quantum theory of the electron. *Proceedings of the Royal Society of London. Series A, Containing Papers of a Mathematical and Physical Character*, 117(778):610–624, 1928.

[59] Uri Vool and Michel Devoret. Introduction to quantum electromagnetic circuits. *International Journal of Circuit Theory and Applications*, 45(7):897–934, 2017.

[60] Steven M Girvin. Circuit qed: superconducting qubits coupled to microwave photons. *Quantum machines: measurement and control of engineered quantum systems*, pages 113–256, 2014.

[61] John Bardeen, Leon N Cooper, and John Robert Schrieffer. Theory of superconductivity. *Physical review*, 108(5):1175, 1957.

[62] Sam Posen and Matthias Liepe. Advances in development of nb 3 sn superconducting radio-frequency cavities. *Physical Review Special Topics-Accelerators and Beams*, 17(11):112001, 2014.

[63] B.D. Josephson. Possible new effects in superconductive tunnelling. *Physics Letters*, 1(7):251–253, 1962.

[64] David M Pozar. *Microwave engineering*. John wiley & sons, 2011.

[65] Martin Göppl, A Fragner, M Baur, R Bianchetti, Stefan Filipp, Johannes M Fink, Peter J Leek, G Puebla, L Steffen, and Andreas Wallraff. Coplanar waveguide resonators for circuit quantum electrodynamics. *Journal of Applied Physics*, 104(11):113904, 2008.

[66] Morten Kjaergaard, Mollie E Schwartz, Jochen Braumüller, Philip Krantz, Joel I-J Wang, Simon Gustavsson, and William D Oliver. Superconducting qubits: Current state of play. *Annual Review of Condensed Matter Physics*, 11:369–395, 2020.

[67] Jay M Gambetta, Conal E Murray, Y-K-K Fung, Douglas T McClure, Oliver Dial, William Shanks, Jeffrey W Sleight, and Matthias Steffen. Investigating surface loss effects in superconducting transmon qubits. *IEEE Transactions on Applied Superconductivity*, 27(1):1–5, 2016.

[68] Z Wang, S Shankar, ZK Minev, P Campagne-Ibarcq, A Narla, and Michel H Devoret. Cavity attenuators for superconducting qubits. *Physical Review Applied*, 11(1):014031, 2019.

[69] Matthew Reagor, Hanhee Paik, Gianluigi Catelani, Luyan Sun, Christopher Axline, Eric Holland, Ioan M Pop, Nicholas A Masluk, Teresa Brecht, Luigi Frunzio, et al. Reaching 10 ms single photon lifetimes for superconducting aluminum cavities. *Applied Physics Letters*, 102(19):192604, 2013.

[70] Hanhee Paik, David I Schuster, Lev S Bishop, Gerhard Kirchmair, Gianluigi Catelani, Adam P Sears, BR Johnson, MJ Reagor, Luigi Frunzio, Leonid I Glazman, et al. Observation of high coherence in josephson junction qubits measured in a three-dimensional circuit qed architecture. *Physical Review Letters*, 107(24):240501, 2011.

[71] Mazyar Mirrahimi, Zaki Leghtas, Victor V Albert, Steven Touzard, Robert J Schoelkopf, Liang Jiang, and Michel H Devoret. Dynamically protected cat-qubits: a new paradigm for universal quantum computation. *New Journal of Physics*, 16(4):045014, 2014.

[72] Alexander Grimm, Nicholas E Frattini, Shruti Puri, Shantanu O Mundhada, Steven Touzard, Mazyar Mirrahimi, Steven M Girvin, Shyam Shankar, and Michel H Devoret. Stabilization and operation of a kerr-cat qubit. *Nature*, 584(7820):205–209, 2020.

[73] MJ Collett and CW Gardiner. Squeezing of intracavity and traveling-wave light fields produced in parametric amplification. *Physical Review A*, 30(3):1386, 1984.

[74] MS Khalil, MJA Stoutimore, FC Wellstood, and KD Osborn. An analysis method for asymmetric resonator transmission applied to superconducting devices. *Journal of Applied Physics*, 111(5):054510, 2012.

[75] Moe Shwan Khalil. *A study of two-level system defects in dielectric films using superconducting resonators*. PhD thesis, University of Maryland, College Park, 2013.

[76] P W Anderson, Bertrand I Halperin, and C M Varma. Anomalous low-temperature thermal properties of glasses and spin glasses. *Philosophical Magazine*, 25(1):1–9, 1972.

[77] William A Phillips. Tunneling states in amorphous solids. *Journal of Low Temperature Physics*, 7(3):351–360, 1972.

[78] S. Hunklinger and A.K. Raychaudhuri. Chapter 3: Thermal and elastic anomalies in glasses at low temperatures. volume 9 of *Progress in Low Temperature Physics*, pages 265–344. Elsevier, 1986.

[79] JJ Freeman and AC Anderson. Thermal conductivity of amorphous solids. *Physical Review B*, 34(8):5684, 1986.

[80] JF Berret and M Meissner. How universal are the low temperature acoustic properties of glasses? *Zeitschrift für Physik B Condensed Matter*, 70(1):65–72, 1988.

[81] Grigorij J Grabovskij, Torben Peichl, Jürgen Lisenfeld, Georg Weiss, and Alexey V Ustinov. Strain tuning of individual atomic tunneling systems detected by a superconducting qubit. *Science*, 338(6104):232–234, 2012.

[82] Stefan Kettemann, Peter Fulde, and Peter Strehlow. Correlated persistent tunneling currents in glasses. *Physical review letters*, 83(21):4325, 1999.

[83] I Ya Polishchuk, P Fulde, AL Burin, Yu Sereda, and D Balamurugan. Effect of nuclear quadrupole interaction on the relaxation in amorphous solids. *Journal of low temperature physics*, 140(5):355–376, 2005.

[84] F. Bloch. Nuclear induction. *Phys. Rev.*, 70:460–474, Oct 1946.

[85] Lara Faoro and Lev B Ioffe. Internal loss of superconducting resonators induced by interacting two-level systems. *Physical review letters*, 109(15):157005, 2012.

[86] Jiansong Gao. *The physics of superconducting microwave resonators*. PhD thesis, California Institute of Technology, 2008.

[87] Wayne Woods, Greg Calusine, Alexander Melville, Arjan Sevi, Evan Golden, David K Kim, Danna Rosenberg, Jonilyn L Yoder, and William D Oliver. Determining interface dielectric losses in superconducting coplanar-waveguide resonators. *Physical Review Applied*, 12(1):014012, 2019.

[88] Naftali Kirsh, Elisha Svetitsky, Alexander L Burin, Moshe Schechter, and Nadav Katz. Revealing the nonlinear response of a tunneling two-level system ensemble using coupled modes. *Physical Review Materials*, 1(1):012601, 2017.

[89] Thibault Capelle, Emmanuel Flurin, Edouard Ivanov, Jose Palomo, Michael Rosticher, Sheon Chua, Tristan Briant, Pierre-François Cohadon, Antoine Heidmann, Thibaut Jacqmin, et al. Probing a two-level system bath via the frequency shift of an off-resonantly driven cavity. *Physical Review Applied*, 13(3):034022, 2020.

[90] Moe S Khalil, FC Wellstood, and Kevin D Osborn. Loss dependence on geometry and applied power in superconducting coplanar resonators. *IEEE Transactions on Applied Superconductivity*, 21(3):879–882, 2010.

[91] Pascal Macha, SHW van Der Ploeg, G Oelsner, E Il'ichev, H-G Meyer, S Wünsch, and M Siegel. Losses in coplanar waveguide resonators at millikelvin temperatures. *Applied Physics Letters*, 96(6):062503, 2010.

[92] Jonathan Burnett, Lara Faoro, I Wisby, VL Gurtovoi, AV Chernykh, GM Mikhailov, VA Tulin, R Shaikhaidarov, V Antonov, PJ Meeson, et al. Evidence for interacting two-level systems from the 1/f noise of a superconducting resonator. *Nature communications*, 5(1):1–6, 2014.

[93] SE De Graaf, L Faoro, J Burnett, AA Adamyan, A Ya Tzalenchuk, SE Kubatkin, T Lindström, and AV Danilov. Suppression of low-frequency charge noise in superconducting resonators by surface spin desorption. *Nature communications*, 9(1):1–6, 2018.

[94] Chen Wang, Christopher Axline, Yvonne Y Gao, Teresa Brecht, Yiwen Chu, Luigi Frunzio, MH Devoret, and Robert J Schoelkopf. Surface participation and dielectric loss in superconducting qubits. *Applied Physics Letters*, 107(16):162601, 2015.

[95] Chih-Chiao Hung, Liuqi Yu, Neda Foroozani, Stefan Fritz, Dagmar Gerthsen, and Kevin D Osborn. Probing hundreds of individual quantum defects in polycrystalline and amorphous alumina. *Physical Review Applied*, 17(3):034025, 2022.

[96] CC Yu and AJ Leggett. Low temperature properties of amorphous materials: Through a glass darkly. *Comments Cond. Mat. Phys*, 14(4):231, 1988.

[97] Alexander L Burin, Douglas Natelson, Douglas D Osheroff, and Yuri Kagan. Interactions between tunneling defects in amorphous solids. *Tunneling systems in amorphous and crystalline solids*, pages 223–315, 1998.

[98] PV Klimov, Julian Kelly, Z Chen, Matthew Neeley, Anthony Megrant, Brian Burkett, Rami Barends, Kunal Arya, Ben Chiaro, Yu Chen, et al. Fluctuations of energy-relaxation times in superconducting qubits. *Physical review letters*, 121(9):090502, 2018.

[99] Jürgen Lisenfeld, Grigorij J Grabovskij, Clemens Müller, Jared H Cole, Georg Weiss, and Alexey V Ustinov. Observation of directly interacting coherent two-level systems in an amorphous material. *Nature communications*, 6(1):1–6, 2015.

[100] Jen-Hao Yeh, Jay LeFebvre, Shavindra Premaratne, FC Wellstood, and BS Palmer. Microwave attenuators for use with quantum devices below 100 mk. *Journal of Applied Physics*, 121(22):224501, 2017.

[101] John C Wheatley, OE Vilches, and WR Abel. Principles and methods of dilution refrigeration. *Physics Physique Fizika*, 4(1):1, 1968.

[102] Jen-Hao Yeh and Steven M Anlage. In situ broadband cryogenic calibration for two-port superconducting microwave resonators. *Review of Scientific Instruments*, 84(3):034706, 2013.

[103] Liuqi Yu, Shlomi Matityahu, Yaniv J Rosen, Chih-Chiao Hung, Andrii Maksymov, Alexander L Burin, Moshe Schechter, and Kevin D Osborn. Evidence for weakly and strongly interacting two-level systems in amorphous silicon. *arXiv preprint arXiv:2110.10747*, 2021.

[104] MS Khalil, S Gladchenko, MJA Stoutimore, FC Wellstood, AL Burin, and KD Osborn. Landau-zener population control and dipole measurement of a two-level-system bath. *Physical Review B*, 90(10):100201, 2014.

[105] Bahman Sarabi. *Cavity quantum electrodynamics of nanoscale two-level systems*. PhD thesis, University of Maryland, College park, 2014.

[106] BL Brock, MP Blencowe, and AJ Rimberg. Frequency fluctuations in tunable and nonlinear microwave cavities. *Physical Review Applied*, 14(5):054026, 2020.

[107] Hanhee Paik and Kevin D Osborn. Reducing quantum-regime dielectric loss of silicon nitride for superconducting quantum circuits. *Applied Physics Letters*, 96(7):072505, 2010.

[108] GJ Dolan. Offset masks for lift-off photoprocessing. *Applied Physics Letters*, 31(5):337–339, 1977.

[109] Marius V Costache, German Bridoux, Ingmar Neumann, and Sergio O Valenzuela. Lateral metallic devices made by a multiangle shadow evaporation technique. *Journal of Vacuum Science Technology B, Nanotechnology and Microelectronics: Materials, Processing, Measurement, and Phenomena*, 30(4):04E105, 2012.

[110] Yasunobu Nakamura, Yu A Pashkin, and JS Tsai. Coherent control of macroscopic quantum states in a single-cooper-pair box. *nature*, 398(6730):786–788, 1999.

[111] Vinay Ambegaokar and Alexis Baratoff. Tunneling between superconductors. *Physical Review Letters*, 10(11):486, 1963.

[112] David C McKay, Sarah Sheldon, John A Smolin, Jerry M Chow, and Jay M Gambetta. Three-qubit randomized benchmarking. *Physical review letters*, 122(20):200502, 2019.

[113] Pranav Mundada, Gengyan Zhang, Thomas Hazard, and Andrew Houck. Suppression of qubit crosstalk in a tunable coupling superconducting circuit. *Physical Review Applied*, 12(5):054023, 2019.

[114] Yu Chen, C Neill, Pedram Roushan, Nelson Leung, Michael Fang, Rami Barends, Julian Kelly, Brooks Campbell, Z Chen, Benjamin Chiaro, et al. Qubit architecture with high coherence and fast tunable coupling. *Physical review letters*, 113(22):220502, 2014.

[115] Jared B Hertzberg, Eric J Zhang, Sami Rosenblatt, Easwar Magesan, John A Smolin, Jeng-Bang Yau, Vivekananda P Adiga, Martin Sandberg, Markus Brink, Jerry M Chow, et al. Laser-annealing josephson junctions for yielding scaled-up superconducting quantum processors. *npj Quantum Information*, 7(1):1–8, 2021.

[116] JM Kreikebaum, KP O'Brien, A Morvan, and I Siddiqi. Improving wafer-scale josephson junction resistance variation in superconducting quantum coherent circuits. *Superconductor Science and Technology*, 33(6):06LT02, 2020.

[117] Josephine B Chang, Michael R Vissers, Antonio D Córcoles, Martin Sandberg, Jiansong Gao, David W Abraham, Jerry M Chow, Jay M Gambetta, Mary Beth Rothwell, George A Keefe, et al. Improved superconducting qubit coherence using titanium nitride. *Applied Physics Letters*, 103(1):012602, 2013.

[118] Felix Motzoi, Jay M Gambetta, Patrick Rebentrost, and Frank K Wilhelm. Simple pulses for elimination of leakage in weakly nonlinear qubits. *Physical review letters*, 103(11):110501, 2009.

[119] Aaron M Holder, Kevin D Osborn, CJ Lobb, and Charles B Musgrave. Bulk and surface tunneling hydrogen defects in alumina. *Physical review letters*, 111(6):065901, 2013.

[120] Luke Gordon, Hazem Abu-Farsakh, Anderson Janotti, and Chris G Van de Walle. Hydrogen bonds in al2o3 as dissipative two-level systems in superconducting qubits. *Scientific reports*, 4(1):1–5, 2014.

[121] Timothy C DuBois, Manolo C Per, Salvy P Russo, and Jared H Cole. Delocalized oxygen as the origin of two-level defects in josephson junctions. *Physical review letters*, 110(7):077002, 2013.

[122] Timothy C DuBois, Salvy P Russo, and Jared H Cole. Atomic delocalization as a microscopic origin of two-level defects in josephson junctions. *New Journal of Physics*, 17(2):023017, 2015.

[123] Alejandro Pérez Paz, Irina V Lebedeva, Ilya V Tokatly, and Angel Rubio. Identification of structural motifs as tunneling two-level systems in amorphous alumina at low temperatures. *Physical Review B*, 90(22):224202, 2014.

[124] Yoni Shalibo, Ya'ara Rofe, David Shwa, Felix Zeides, Matthew Neeley, John M Martinis, and Nadav Katz. Lifetime and coherence of two-level defects in a josephson junction. *Physical review letters*, 105(17):177001, 2010.

[125] TA Palomaki, SK Dutta, RM Lewis, AJ Przybysz, Hanhee Paik, BK Cooper, H Kwon, JR Anderson, CJ Lobb, FC Wellstood, et al. Multilevel spectroscopy of two-level systems coupled to a dc squid phase qubit. *Physical Review B*, 81(14):144503, 2010.

[126] Timothy Kohler. *Spectroscopy of Two Level Defects and Quasiparticles in Superconducting Resonators*. PhD thesis, University of Maryland, College park, 2021.

[127] Alexander L. Burin, Moe S. Khalil, and Kevin D. Osborn. Universal dielectric loss in glass from simultaneous bias and microwave fields. *Phys. Rev. Lett.*, 110:157002, Apr 2013.

[128] Shlomi Matityahu, Hartmut Schmidt, Alexander Bilmes, Alexander Shnirman, Georg Weiss, Alexey V Ustinov, Moshe Schechter, and Jürgen Lisenfeld. Dynamical decoupling of quantum two-level systems by coherent multiple landau–zener transitions. *npj Quantum Information*, 5(1):1–7, 2019.

[129] Jan David Brehm, Alexander Bilmes, Georg Weiss, Alexey V Ustinov, and Jürgen Lisenfeld. Transmission-line resonators for the study of individual two-level tunneling systems. *Applied Physics Letters*, 111(11):112601, 2017.

[130] Alexander Bilmes, Serhii Volosheniuk, Jan David Brehm, Alexey V Ustinov, and Jürgen Lisenfeld. Quantum sensors for microscopic tunneling systems. *npj Quantum Information*, 7(1):1–6, 2021.

[131] Bahman Sarabi, Aruna N Ramanayaka, Alexander L Burin, Frederick C Wellstood, and Kevin D Osborn. Projected dipole moments of individual two-level defects extracted using circuit quantum electrodynamics. *Physical Review Letters*, 116(16):167002, 2016.

[132] Herve M Carruzzo and C Yu Clare. Why phonon scattering in glasses is universally small at low temperatures. *Physical review letters*, 124(7):075902, 2020.

[133] PV Klimov, Julian Kelly, Z Chen, Matthew Neeley, Anthony Megrant, Brian Burkett, Rami Barends, Kunal Arya, Ben Chiaro, Yu Chen, et al. Fluctuations of energy-relaxation times in superconducting qubits. *Physical review letters*, 121(9):090502, 2018.

[134] T Lindström, JE Healey, MS Colclough, CM Muirhead, and A Ya Tzalenchuk. Properties of superconducting planar resonators at millikelvin temperatures. *Physical Review B*, 80(13):132501, 2009.

[135] David P Pappas, Michael R Vissers, David S Wisbey, Jeffrey S Kline, and Jiansong Gao. Two level system loss in superconducting microwave resonators. *IEEE Transactions on Applied Superconductivity*, 21(3):871–874, 2011.

[136] MS Khalil, MJA Stoutimore, S Gladchenko, AM Holder, CB Musgrave, AC Kozen, G Rubloff, YQ Liu, RG Gordon, JH Yum, et al. Evidence for hydrogen two-level systems in atomic layer deposition oxides. *Applied Physics Letters*, 103(16):162601, 2013.

[137] Katarina Cicak, Dale Li, Joshua A Strong, Michael S Allman, Fabio Altomare, Adam J Sirois, Jed D Whittaker, John D Teufel, and Raymond W Simmonds. Low-loss superconducting resonant circuits using vacuum-gap-based microwave components. *Applied Physics Letters*, 96(9):093502, 2010.

[138] John D Teufel, Dale Li, MS Allman, K Cicak, AJ Sirois, JD Whittaker, and RW Simmonds. Circuit cavity electromechanics in the strong-coupling regime. *Nature*, 471(7337):204–208, 2011.

[139] TA Palomaki, JD Teufel, RW Simmonds, and Konrad W Lehnert. Entangling mechanical motion with microwave fields. *Science*, 342(6159):710–713, 2013.

[140] Noah Gorgichuk, Tobias Junginger, and Rogério de Sousa. Origin of dielectric loss at the nb/oxide interface: Evidence for atomic two-level systems. *arXiv preprint arXiv:2203.05054*, 2022.

[141] Gustav Andersson, André Luiz Oliveira Bilobran, Marco Scigliuzzo, Mauricio M de Lima, Jared H Cole, and Per Delsing. Acoustic spectral hole-burning in a two-level system ensemble. *npj Quantum Information*, 7(1):1–5, 2021.

[142] Lara Faoro and Lev B. Ioffe. Interacting tunneling model for two-level systems in amorphous materials and its predictions for their dephasing and noise in superconducting microresonators. *Phys. Rev. B*, 91:014201, Jan 2015.

[143] David Niepce, Jonathan J Burnett, Marina Kudra, Jared H Cole, and Jonas Bylander. Stability of superconducting resonators: Motional narrowing and the role of landau-zener driving of two-level defects. *Science advances*, 7(39):eabh0462, 2021.

[144] Alexander Melville, Greg Calusine, Wayne Woods, Kyle Serniak, Evan Golden, Bethany M Niedzielski, David K Kim, Arjan Sevi, Jonilyn L Yoder, Eric A Dauler, et al. Comparison of dielectric loss in titanium nitride and aluminum superconducting resonators. *Applied Physics Letters*, 117(12):124004, 2020.

[145] R Barends, HL Hortensius, Tony Zijlstra, Jochem JA Baselmans, SJC Yates, JR Gao, and Teun M Klapwijk. Noise in nbtin, al, and ta superconducting resonators on silicon and sapphire substrates. *IEEE transactions on applied superconductivity*, 19(3):936–939, 2009.

[146] Frank Arute, Kunal Arya, Ryan Babbush, Dave Bacon, Joseph C Bardin, Rami Barends, Rupak Biswas, Sergio Boixo, Fernando GSL Brandao, David A Buell, et al. Quantum supremacy using a programmable superconducting processor. *Nature*, 574(7779):505–510, 2019.